Single Ion Detection Using FET Based Nano-Sensors:

A Combined Drift Diffusion and Brownian Dynamics 3D Simulation Study

Iain Moore

Submitted to the University of Glasgow

School of Engineering

in fulfilment of the requirements for the degree of Doctor of Philosophy

April 2014

ABSTRACT

There is an ever increasing requirement for rapid sensing mechanisms for a variety of purposes – from blood analysis to gas detection. In order to allow large throughput, these devices must also be available at low cost per unit. One method which meets these criteria is the interfacing of biological and nano-scale semiconductor elements. Using modern CMOS processing, alongside further post processing, such devices can be created for a variety of purposes. However, development of these devices is expensive and in order to investigate possible structures, a simulation system is ideal.

This work details the development, testing and utilisation of such a system. By combining two widely understood simulation methods – Brownian dynamics and drift diffusion – a mix of efficiency and accuracy is achieved. The introduction begins with a section detailing background to the field in order to set the work in context. The development and strict testing regime employed is then described. Initial simulations of a bio-nano interface are then presented with detection of ions though alterations in the drain current of a nominal 35 nm FET. This shows that there is a 5 nA/μm increase in drain current when an ion is moved through a 3 nm lipid layer which is suspended 15 nm above the oxide allowing identification of the period of traversal of the lipid layer. The final chapter indicates the successful detection of individual ions traversing a nano-pore in the presence of biologically significant ionic concentrations. The rate of change of drain current in the FET indicates a 4 σ signal during traversal with a background concentration of ions of 1 mM which allows clear identification of this individual event.

Acknowledgements

The list of people who have helped me through this research could be longer than the thesis, so I will name only a handful of those to whom I am greatly indebted. First, I would like to thank my supervisors, Asen Asenov and Campbell Millar without whom this research would not have started. Thanks must also go to my additional supervisor, Scott Roy, who is famous amongst students for being the man who will always help. He stepped in when he had many more important things to do.

I must also thank all of the members of the Device Modelling group which has seen many changes during my tenure. I would like to thank Gareth and Craig, who led me to join the group, and more importantly without whom I would have not seen the process through. Gordon, Craig, Dave, Elisa, Doug and Daniel for support, computer help and setting the world to rights. Thanks to Jon and Billy for solving so many mini problems.

Finally, I must thank my family for their endless support throughout the many extending years of my research. This would simply never have seen the light of day without them.

List of Publications

1. Moore, I.; Millar, C.; Roy, S.; Asenov, A., "Integrating drift-diffusion and Brownian simulations for sensory applications," *Proceedings of the 11th International Conference on Ultimate Integration on Silicon*, pp.85-88, 2010.

2. Moore, I.; Millar, C.; Roy, S.; Asenov, A., "Brownian noise in FET based nano-pore sensing: A 3D simulation study," *Proceedings of the 14th International Workshop on Computational Electronics (IWCE)*, pp.1-4, 2010.

3. Moore, I.; Millar, C.; Roy, S.; Asenov, A., "FET based nano-pore sensing: a 3D simulation study," (Invited) *Journal of Computational Electronics*, vol. 11, no. 3, pp.266-271, 2012.

Contents

List of Figures

Chapter 1

Introduction

Sensors are used for many purposes. Among the applications is drug research, as it becomes more sophisticated, and as bioterrorism becomes a serious threat, reliable and accurate biosensors become more and more important. There is also a desire for selective, rapid and transportable sensors to allow use in clinical situations, with the ability to complete tests at the bedside [1].

Simulation of devices offers a relatively inexpensive and risk free alternative to experimentation to improve sensor design before the prototyping stage. For this reason efficient simulators which allow thorough investigation of potential advances are essential tools in modern sensor design. Previous simulation tools have used a single simulation technique; Simulations based on Brownian dynamics allow particle detail, but are computationally slow [2]. Simulations based on drift diffusion lose the detail of individual particle movement. Simulations based on molecular dynamics, due to its incredible detail, are

unworkable over the timescales required. Instead, this work proposes a simulation approach that combines the efficiency of drift diffusion with the particle detail provided by Brownian dynamics simulations in the analysis of field effect based ion channel sensors.

1.1 Aims and Objectives

The aim of this PhD was to develop a new, efficient nano-bio-CMOS device simulator combining Brownian dynamics and drift-diffusion simulation techniques in a single simulator domain. This built upon the self-consistent Brownian dynamics simulation techniques developed by C. Miller in his PhD thesis [3]. By integrating this with the Glasgow University Device Modelling Group's drift diffusion simulator, the intent was to provide a tool with two main advantages over those using previous simulation techniques – efficiency and atomic scale resolution. The efficiency of drift diffusion, to reduce computational overhead is combined with the single particle motion details resolved by Brownian dynamics where required. Creation of such a combined simulator would provide an ideal tool for the design of novel devices as it allows the investigation of a variety of structures without the expense of manufacturing individual prototypes.

The first step was to create a simulation harness which combines drift diffusion and Brownian dynamics domains. The time taken to perform a single simulation was greatly reduced over that of a traditional Brownian simulator, since the frequently repeated solution of the electrostatic potential required by particle simulations imposed a greater computational burden compared to the drift diffusion techniques [4]. This advantage was provided with a minimal reduction

in the accuracy of the simulated current-voltage characteristics extracted as the device areas where single ion flux is important were modelled with Brownian dynamics, while the continuum method was used in the sensing transistor area [2].

Previous work has clearly demonstrated the benefits of using Brownian dynamics to model ion conduction through biological pores [5] and the advantages of using drift diffusion for MOSFET simulations of semiconductor devices have been apparent for many years [6]. By combining both simulation techniques, each can be best utilised to exploit their strengths while maximising the computational efficiency of the simulation as a whole. This combined harness was then applied using the appropriate technique in each section of an ion channel sensor. Additionally the two domains could be integrated into a single ion channel simulation which allows larger, or more detailed, simulations than those currently computationally feasible, over the microsecond time scales, which are relevant for comparison of simulation and experimental data.

In order to achieve coupled simulations in a single domain, charge and potential interactions from a Brownian simulation were accurately and efficiently coupled into a drift diffusion simulation domain. This allowed charges in each domain to interact via the electric field in such a way as to allow the effect of ion position on the current-voltage and characteristics of MOSFETs to be assessed.

The combined simulator was rigorously tested with progressively more complex devices in order to ensure the correct operation of all elements. This involved moving from a basic resistor model through diodes and capacitors to an analytical field effect transistor (FET) with known characteristics. This complex, but well understood, structure allowed full testing and evaluation of the simulation harness before its application in combined bio-semiconductor device simulations.

Finally, the simulation harness was utilised to model FET sensors which incorporate a nano-pore. The nano-pore and surrounding electrolyte acted in place of a MOSFET gate. Chemical current sensors work in a similar way, where an organic chemical sensor acts as the gate for a MOSFET [7] and a DNA sensor based on a long channel MOSFET where the charge on a DNA molecule modulates current to flow in the channel of a MOSFET [8] has been created. Through observation of the drain current, analysis of the traversal of ions through the pore was made.

1.2 Outline of Thesis

A brief review of the literature covering some of the aspects of this project follows in chapter 2. This includes a brief introduction to ion channels and their importance, and sensors and their applications and describes important and recent developments in simulation methodology.

The two simulation methodologies used in this research are Brownian dynamics and drift-diffusion. Chapter three describes these approaches in detail It describes the implementation of the two simulation techniques used in this research. In particular, there is a focus on the Brownian and drift-diffusion approaches which are most important for this work.

Chapter four describes, in considerable detail, the development of the software. The testing of the software tools is covered in depth, as the implementation of a reliable and accurate combined simulator was one of the major objectives of this research. The in depth nature of the description of this work is an attempt to

emphasise the difficulties overcome in achieving a simulation with combined methodologies and aligning two separate codebases.

Chapters five and six discuss the results obtained using the developed software. The first of these chapters covers drift-diffusion based simulations, where the steady state effect of individual ions is investigated, without considering the Brownian motion associated with them. A lipid layer with a nano-pore is introduced at this stage, and the effect of ion position on FET drain current is described.

Chapter six focuses on the dynamic effect of ions as they move according to Brownian motion. Once the effect of the Brownian 'noise' is established, the nano-pore is introduced in the combined simulation domain to investigate the sensing possibilities of the FET. Two sets of results are presented. The first set of investigations use artificial movement of a pore, while the second set of investigations shows that this sensing capability is present even when the ion which occupies the pore is experiencing Brownian motion itself.

The final chapter gives an overview of the results which were obtained, and the conclusions drawn. Additionally, this chapter details the many directions which may be followed to obtained further interesting results using the simulator as the next steps of the research into the combination of biological and electronic systems for sensing applications.

Chapter 2

Background

2.1 Ion Channels

Evolving over three billion years ago [9], ion channels are proteins made of chains of amino acids which self-assemble in such a way as to create nanopores, with a wide range of properties, in the membranes of cells. As a general class of proteins, ion channels evolved to control the flux of ions through the cell membrane. They are present in all known biological cells [10]. Ion channels are directly responsible for a wide range of biological functions such as cellular signalling mechanisms [11], including that of neurons [12], hormone secretion and muscle contraction (including in the heart) [13]. Their importance is further highlighted based on the estimate that approximately 60% of all pharmaceuticals target, either directly or

indirectly, the function of these proteins, and that this percentage is likely to increase over the coming years [14]. It has been pointed out that a greater knowledge of the mechanisms by which single channel functions will lead to the understanding of many neurological and muscular disorders, and in fact may lead to cures [15].

Ion channels display a wide range of behaviours similar to solid-state devices, such as gating, switching, and rectification, while utilising very different mechanisms [9,16]. One indicative structure of an ion channel is shown in Figure 2.1. They perform a wide range of functions in biology, analogous to those in complex electronic systems, such as communication between cells. Some ion channels exhibit gating behaviour and can therefore be viewed as biological switches, and direct comparisons to the behaviour of MOSFETs can be made, in that they have inputs, outputs, gating properties and a channel through which current flows [17]. It has been demonstrated that a biological device closely

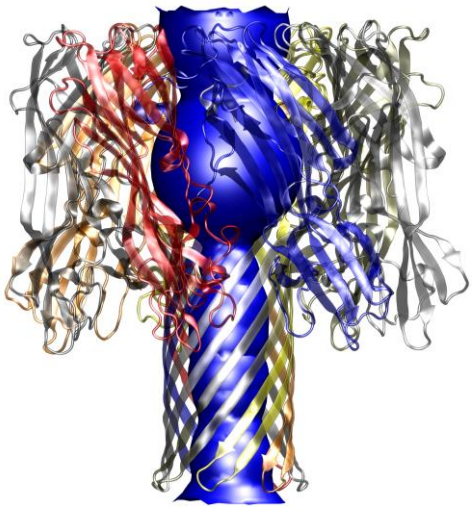

Figure 2.1 – An example structure of a large ion channel (α-Haemolysin RL2 Mutant). The blue section indicates the pore in the structure which ions flow through. After Millar [18].

emulating a diode can be created using protein engineering [16]. Some research has taken place into the use of silicon devices for nerve repair [19], and the reliable coupling of ion channels to MOSFETs would significantly enhance this research and hasten the development of a direct semiconductor neural interface.

The link between biology and MOSFETs is now considered so strong that references in the International Technology Roadmap for Semiconductors have been made regarding the relevance of ion channel research in the semiconductor area [20]. Greater understanding of the coupling of biological elements with MOSFETs will allow the design of nano-bio-electronic devices capable of forming a direct interface between electronic hardware and biology and if realised, will allow a new generation of biosensors to be created. They would also provide direct neural interfaces, and perhaps allow biological computing to exploit the massive parallelism inherent in biological systems [21,2]. Since both solid state devices and biological signalling rely on charge transport, interactions between them are possible through the electric field, and nerve cells from rat brains have already been interfaced to silicon transistors [22].

In order to predict the operation of such a new generation of biosensors, and thus facilitate their design and optimisation, simulation tools are needed. Thus far, only basic simulations of bio-nano-CMOS devices, using continuum drift-diffusion methods to model their constituent ion channels, have been published [14]. However, it is well understood that continuum models poorly model the infrequent, stochastic traversal of single ions through ion channels [2]. Therefore, new simulation methodologies are needed – including combining simulation techniques across different model domains – in order to optimise the overall speed and accuracy of simulation of such complex systems, and thus allow ‘sifting; of the design space of the vast range of possible bio-nano-CMOS devices.

The results of this research focuses on FET and ion-channel based biosensors as exemplars. But the simulation tools developed should have applicability to a wider range of biosensors. Therefore, the following sections of this background chapter (sections 2.2-2.3) will review various types of sensors, both historic and current, placing this research in the context of an expanding field. Then current trends in the simulation of these complex systems will be reviewed (section 2.4) and the relative merits of each of the most important simulation techniques used to model biosensors - molecular dynamics, Brownian dynamics, and drift-diffusion - described.

2.2 Sensors

In order to be regarded as a sensor, a device must include a transducer, some method of interpreting information, such as interface circuitry, and also the package which holds the device [23]. Metal oxide semiconductor field effect transistors (MOSFETs) are devices which use an electric field applied to the "gate" to attract mobile charges to allow current to flow between two terminals. A schematic diagram of a basic MOSFET can be seen in Figure 4.20. These devices can be 'functionalised' by the removal of the metal gate and the addition of specific biological or chemical elements, as indicated in Figure 2.2, to cause increases in the electric field as a result of analytes attaching themselves to the gate material. CMOS technology is the basis of modern computing and uses FETs as a method of interpreting data – thus allowing the interface circuitry and information interpretation to be manufactured alongside the FET based sensor on a single device. To do this, the outputs should be in the range of 0-3 V depending on the specific interfacing technology used – with more modern devices capable of operating with the lower part of this range.

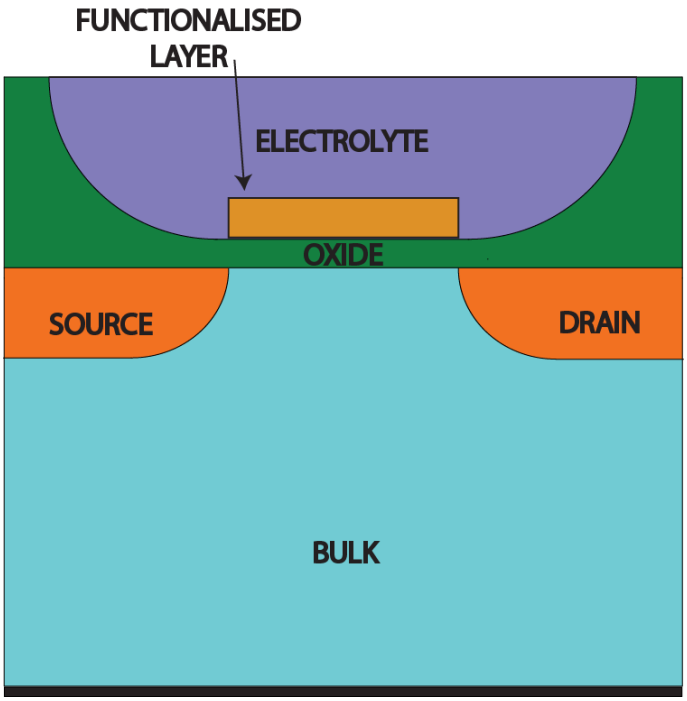

Figure 2.2 – Schematic of a FET based biosensor with a possible functionalised layer.

The devices which form the focus of this work are particularly useful in that they form the transducer element of the sensor, but due to the use of a FET, they can easily be interfaced with modern CMOS circuitry. There are multiple types of sensor, but the discussion in this chapter will be limited to two broad types – chemical and biological as indicated later in Figure 2.6.

A chemical sensor is a device which takes chemical signals and transforms them to interpretable information. A biosensor is a sub-class of chemical sensors, where a biological mechanism is the target of the sensing stage [24]. The International Union of Pure and Applied Chemistry definition of a biosensor: "an electrochemical biosensor is a self-contained integrated device which is capable of providing specific quantitative or semi quantitative analytical information using a biological recognition element (bio-chemical receptor) which is retained in direct

spatial contact with an electrochemical element [25]." This definition is sufficiently non-specific to allow for multiple types of sensor, and currently many biosensors require large, difficult to use equipment in order to function (laboratory equipment which is installed on benches). The definition does not, however, allow for biosensors which do not require an electrochemical element, and it must be noted that biosensors without the electrochemical element do exist. Further moves towards FET based sensors will allow smaller, lower power, more portable devices to be designed, with the further benefit that it is conceivable that a biosensor chip could be constructed using standard CMOS processes, with amendments to the process to include biological elements. Affinity biosensors are an example of this which use molecules in order to sense the presence of specific analytes, for example antibodies can be used to identify diseases [26]. Whole devices can be fabricated on the mm scale with the active sensing regions in the order of hundreds of µm and individual electrodes and sensing sites on the nano-scale [27] with power consumption in the mW range. These can be produced by altering a MOSFET or nano-wire FETs with post-production functionalisation techniques.

2.3 Sensor Applications

To understand the importance of biosensors, it is important to begin by describing their applications. Continuous, selective detection of biological molecules is one of the most widely stated requirements in biosensing literature [28,29], and as sensors become simpler to use, less expensive and more portable, their use is becoming more common in clinical applications [1].

The ability to detect, and identify various biomolecules is not only important in clinical diagnostics, but can be extended into various areas of scientific research [30]. Biosensors could be used to monitor the effects and amounts of pollutants in the environment, for monitoring the food industry, to aid medical research and to accelerate drug screening processes [25,31]. More specifically, they could be used for the detection of viruses, proteins, antibodies, DNA, electrolytes, drugs and pesticides [32]. Each of these individual sensors would require some form of embedded sensing mechanism, such as an enzyme or chemical receptor, and would be on the scale of tens to hundreds of nanometres [33]. These would most likely be built onto an overall platform on the millimetre scale, most likely including multiple individual sensors, such as those described in the previous section.

Silicon device based research sensors have been suggested as a method for rapid detection of various proteins and DNA in order to provide higher throughput assaying systems [34,35]. Detection and identification of specific sequences of DNA could allow the identification of various diseases and cancers, and devices which allow this are in great demand [8]. Arrays of various types of silicon technologies, including immobilisation of DNA on a gold-based gate layer [28] as shown in Figure 2.3 and nanotubes and nanowires have been suggested as potential future technologies for rapid medical screening [36].

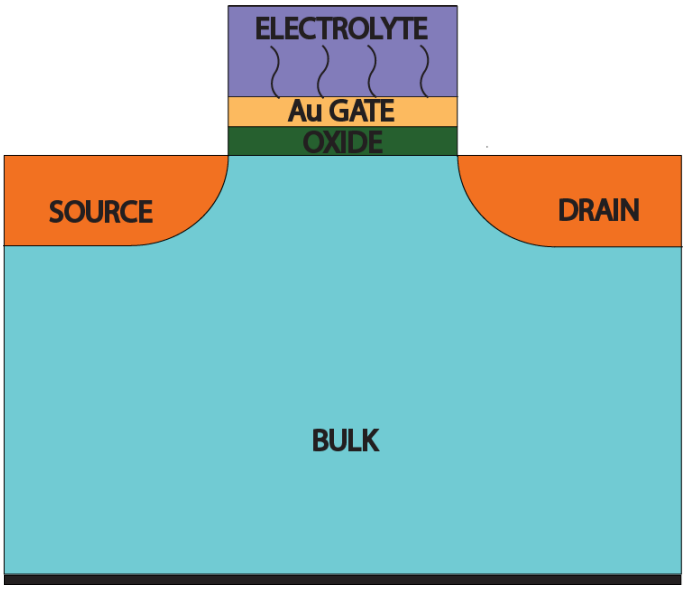

Figure 2.3 – DNA sensor with a gold gate layer which enables immobilisation of DNA.

Rapid (minutes from sampling to result), accurate, where specific analytes can be sensed at 1 nM concentrations and below, sensors are also desired by military, law enforcement and security forces [25]. Bioterrorism is now a clear threat world-wide, and it is essential that biosensors are able to detect biological and chemical threats both quickly and accurately. One of the biggest challenges is to develop sensors which are specific enough to identify threats, but with the flexibility to be able to detect mutations, altered versions of, or previously unknown chemical and biological substances [37]. The functionalization of the sensing mechanism, such as an enzyme is more difficult in these cases as they may not be ideally suited to the purpose due to the specific mutation. This is where the step of direct sensing, as opposed to functionalisation of the device may be an advantage – instead of searching for specific molecules, each molecule could be identified and analysed.

The ability to detect ions in a solution is of particular use when detecting proteins, DNA and viruses and this forms the primary focus of this work. The sensitivity of devices already demonstrated for the sensing of hydrogen ions, for example, has reached a measurable change in conductance of between 5 and 150 nS/pH in an FET based sensor with a functionalised nano-wire, depending on setup characteristics [30,38]. The use of ion channels as components has also already been demonstrated in working biosensors [39]. One example using the gramicidin-A channel protein embedded in a synthetic lipid layer, senses the movement of ions through the ~0.2 nm channel [40] by microsiemens changes in the conduction of a gold electrode approximately 4 nm away [32].

It has been stated in research that there is a need for devices with a faster response than current methods [41]. Specifically, lab-based tests currently require timescales of hours to days to complete, whereas the production of smaller portable sensors would allow tests to take place *in situ*. This would conceivably decrease the timescale to minutes to low number of hours for similar tests. It is likely that nano-scale electronic devices will provide precision with detection of biological interactions above 95% [41] and the ease of integration with digital electronic circuits will enable the fabrication of devices which could be handheld, inexpensive and highly integrated devices capable of both sensing and analysis [42,29]. It is intended that, by enabling rapid simulation of novel devices, this research will provide a platform for investigation of a wide array of combined bio-nano devices. Present and proposed simulation techniques for such devices will be discussed in section 2.4 below.

2.3.1 Present Sensing Methods

Various methods are currently employed in biological sensing, centrifugation, filtration, dielectrophoresis, immunomagnetic separation and nucleic acid extraction are all widely used, but these methods are labour intensive and often expensive [37]. Additionally, gas chromatography and mass spectrometry have been used in sensing, but these have three disadvantages; they are slow – taking tens of minutes for the test and require preparation and transportation of samples, expensive – costing thousands of pounds for the equipment, and highly non-portable [43,44].

Measuring minute (ng/ml) mass changes with a quartz crystal microbalance (QCM) is one of the most common methods of DNA analysis, but is very difficult, though not impossible, to convert the readings into a useable and analysable electrical signal [28]. The output is a change of the frequency of the crystal oscillation, at best 1.5 Hz/ppm [43], and is dependent on the exact unloaded frequency for ambient conditions. Electro chemical DNA analysis requires that an indicating label be attached to the DNA strand however this method does have the advantage that the signal can be more easily amplified since the signals from these sensors are electrical – the output is caused by a nanoamp range current induced when a reaction of the target molecule occurs on the surface of the electrodes - and can be combined with circuitry [45].

The optical analysis of DNA requires the target to be fluorescently labelled so that it reacts to a specific wavelength of light. The optical detection techniques are useful due to their high specificity and sensitivity – up to ~10^7 molecules/cm^2, but suffer from a difficulty when it comes to miniaturisation due to the cost of

individual devices and requirement for multiple stages, and thus individual laboratory elements [45]. At this stage, optical methods require permanent setup in a laboratory situation. Optical sensing is the dominant method at the moment, despite the fact that it uses costly and non-portable equipment and requires significant pre-processing of the sample, meaning multiple steps for each sample and result [8,46,47].

Modern sensing techniques often require the amplification of the sample, for example with DNA it may be necessary to increase the concentration of a sample using the polymerase chain reaction. This means that these technologies are restricted on two fronts: firstly, the time taken for a given test is increased because of the steps required to amplify the signal, often meaning that real time analysis is not possible. Secondly, these sensing methods require the use of specialist equipment which, in turn, may require trained personnel to operate them [26].

There has been some work to integrate electrochemical methods with CMOS circuitry [48]. These methods involve sensors producing ~100 nA analogue current signals which are converted using CMOS based analogue to digital converters before being analysed. Most research which uses semiconductors, however, has focussed on sensing methods based on FET devices which may in turn be integrated with CMOS analysis circuitry – this means that the intermediate step need only be an analogue to digital converter. These offer the distinct advantage that they can be produced on a single chip and altered using post processing techniques. Electronic detection techniques have not yet been fully investigated and may yield significant advances in low cost, portable sensing technology [47]. This work aims to demonstrate a tool which would allow the full investigation of these devices through simulation, allowing rapid development of advanced sensors.

2.3.2 FET Based Sensing Methods

Biochips are used in many forms as biosensors. Semiconductor based sensors have also been used in conjunction with more traditional sensing methods, for example a sample, concentrated by dielectrophoresis to enhance the target agent, has been detected by an immunoassay which is activated by an electric field in the region of 125 kV/m over tens of micrometres [37].

Semiconductor devices, at the cutting edge of technology for their time, have been being used in an attempt to make novel sensors for decades, for example in 1974 a 10µm FET was submerged in an electrolyte solution in order to analyse mV range potentials due to biological activity [49]. Hydrogen sensitive FET devices were developed as long ago as 1975 [50]. As a result of their comparative size, modern 35 nm MOSFET devices and biological molecules, which are typically tens of nanometres, with features at the sub-nano scale, are ideally suited for use in integrated sensors [51]. A mix of this type of sensor has been investigated – using biological and electronic elements in a hybrid system creating a link between the two domains [52] allowing the inherent integration of analytical circuitry. This leads to the potential for *in vivo* utilisation of nanoscale biosensors [53].

There has already been research which shows that it is possible to place nano meter scaled ~3 nm pores into membrane layers, using traditional lithographic techniques with post processing, to create the hydrophobic layers similar to those shown in this research [54]. Porous silicon devices have also been used as detectors with the ability to distinguish between gram positive and gram negative

microorganisms [37]. Gram testing is a basic test used in the analysis of bacteria and other microorganisms which separates the organisms in two broad groups based on the cellular structure. Gram positive denotes organisms which will retain crystal violet dye while gram negative will decolour when rinsed in iodine solution.

When using silicon based sensors without biological components, there is a lack of inherent selectivity in biological elements which have evolved to bind to specific molecular species. This problem can be remedied, though, by the addition of biological elements such as ion channels. The use of biomolecules, which are themselves selective, leads to selectivity in the biosensor [55]. Various biological elements can be, and have been used as recognition mechanisms. Enzymes, antigens and nucleic acids all offer the potential to activate the surface of a FET allowing it to function as a detector of some analyte. A FET based sensor modified with a dinitrophenyl antigen has shown a sensitivity in of ~20 mV per decade to concentrations of its antibody and enzyme modified FETs have indicated sensitivities to the concentration of penicillin of >50 mV/pH [25]. A schematic of such a scheme is shown in Figure 2.4.

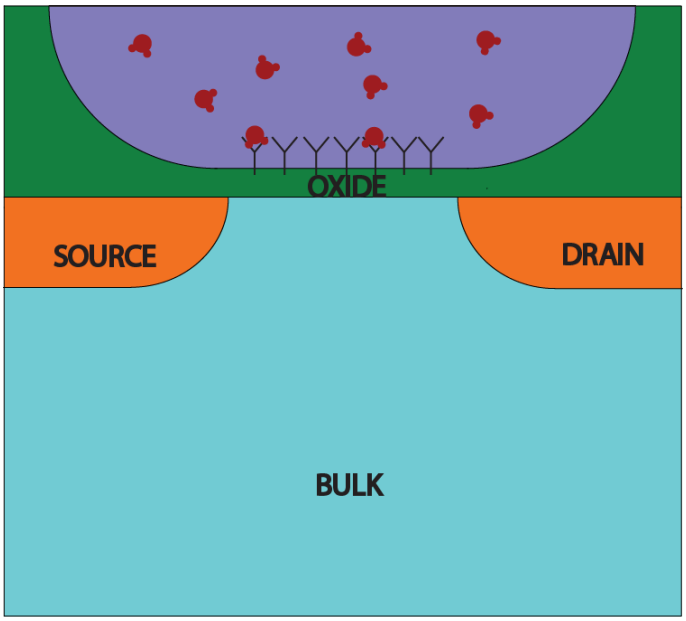

Figure 2.4 – Schematic of a FET based biosensor which has been functionalised with an antigen at the oxide interface, this will bind to a specific analyte which will increase drain current in the FET.

There are three major types of FET based biosensor. Enzyme modified FETS or EnFETs, Cell based FETs which observe changes in the potential of living systems and ImmunoFets which use surface polarisation effects [56]. Some classifications bring EnFETs and ImmunoFets into the same characterisation – ISFETS (Ion Sensitive FETs). These are discussed in greater detail in section 2.3.2.3. The work presented in this thesis investigates a fourth style of sensing structure, which can also be classified as a type of ISFET, where charge transported through a nanopore suspended in a lipid layer above the channel of a MOSFET modulates the current flow in the solid-state device. Some work has already been performed on such a device, in this case using an ion channel as one gate in a double gate device [14].

2.3.2.1 Benefits of FET Based Sensors

Microbiosensors have many potential advantages over current electrochemical and optical methods including size and weight – they are often small enough for hand held device, rapid response since they give results on the scale of minutes rather than hours, and inherent compatibility with microchips [25]. System stability and reliability can be improved by greater integration of the sensing and analysis sections of a biosensor [57,58].

The devices demonstrated in this work are FET based devices which would be easily integrated to analysis circuitry and could be optimised with various biological elements to produce sensors with a range of applications. This means that they are likely to be inexpensive when mass produced allowing for a vast array of applications [59]. One major advantage of FET based sensors made using traditional CMOS fabrication techniques is the ability to create low cost integrated designs, where the sensor and analytical circuitry is on the same piece of silicon [60] and are produced without requiring expensive additional, or custom, process steps. These are plausible because FET based sensors are able to directly translate a signal, caused by analyte interaction, into a signal which can be processed without detection optics.

These sensors allow real time, label free analysis and detection of molecules. Additionally, as semiconductor devices have shrunk in size (with sub 35 nm nominal gate lengths in full production), they have become ideal for interfacing with similarly sized biological structures such as nucleic acids [56]. This leads to the idea that FET based systems would be miniaturised in comparison to current methods [61] leading to the possibility of portable devices able to be used in situ instead of samples being sent to a lab. Furthermore, ion sensitive FETs (ISFETs)

have advantages over more traditional ion selective electrodes as they are smaller – ranging from nano to micrometres, are more robust and cost less since they usually use existing CMOS technology which can be used alongside post-processing to produce devices for <10 cents [57]. However, relying on electrostatic interactions for sensing does present problems in some cases. For example, many applications require that it may be necessary to detect μM to mM range concentrations of a compound leaching through various background materials, and the concentration of the analyte may be much smaller than that of the background ion content of the water in which the sensor resides [37]. A highly selective sensor will go some way to remedying this problem, but an understanding of the issues related to noise in the sensor input signal and the effects of charge screening is essential.

FET based sensors are label free [46,62], meaning that there is no requirement for fluorescent or chemical 'tags' for their functionality. Therefore less processing of a sample is required, and this is especially advantageous in DNA analysis [63]. Label free methods do, however, have some issues. The lack of specific binding may lead to false positives as similar molecules and agents are interpreted incorrectly [26].

2.3.2.2 FET Based Non-Biological Sensors

Chemical and gas sensors which are based on MOSFET structures have been created. A FET based chemical sensor can be described as a standard MOSFET with the metal replaced by a conducting solution and a reference electrode. Similarly the metal in a MOS structure may be replaced with an electrolyte or a

chemically sensitive metal. The conducting solution can be altered to provide the sensor with some degree of selectivity – the selectivity depends strongly on the specific analyte and reaction involved [59]. In each case, the device can be monitored through a change in conductance, around 40 nS/μM, or a shift in threshold voltage of a few microvolts per ppm [38]. Gas sensors have been produced which involve gas sensitive metals, chosen depending on which gas is to be selected and sensed, are deposited on the gate of FET device. This will have the effect of altering one of the parameters of the device such as 100 nA range changes in drain current, or microvolt changes in gate voltage or threshold voltage through changes in the work function. [43]

MOS gas sensors have the distinct advantage of rapid response – less than one minute (essential when dealing with compounds with high toxicity), inexpensive production and simple integration with silicon circuitry. Their response, however, has a strong dependence on the temperature and generally require that the ambient temperature of the sensor must be much higher than normal room temperature (>250 °C) [43]. MOSFET sensors can be produced using standard manufacturing techniques with the addition of an extra gate material. Changes in threshold voltage, source-drain current and gate voltage can all be used as the indicator of gas concentration. As with other devices discussed in this section, MOSFET sensors can be easily integrated with semiconductor circuitry.

2.3.2.3 ISFETs and EnFETs

An ISFET is, in essence, a MOSFET where the metal gate has been replaced by a solution and an additional reference electrode, as shown in Figure 2.5 [64]. In some cases, the oxide is coated with a layer which is sensitive to the particular target analyte and the device is then immersed in a solution along with the

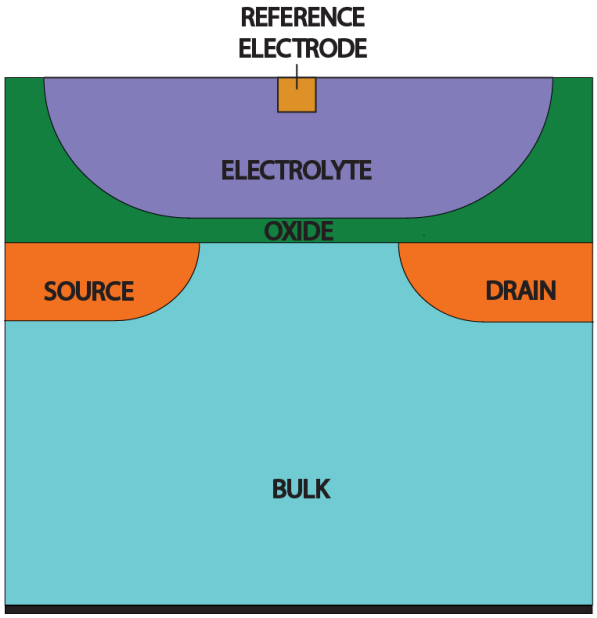

Figure 2.5 – Schematic of an example ISFET. The reference electrode is placed in a solution and, as with earlier examples, the oxide layer may be functionalised with a metallic layer or biological component.

reference electrode [65,58]. ISFETs are not new and the first example of an ISFET was demonstrated in 1970 [66]. This short paper was the precursor to a large amount of research in the following decades, as summarised in Bergveld's review paper in 2003 [64].

Early attempts to construct an ISFET showed that, while the characteristics of the oxide would be altered slightly by immersion in an electrolyte solution (the oxide becomes partially hydrated and thus no longer fully electrically insulates), the operation of the device would remain similar to that of a standard MOSFET where the source – drain current is controlled by the gate potential, or its equivalent [67]. An epoxy resin was used to isolate the contact between the source and drain, and the electrolyte solution [66]. ISFETs have a rapid response –

reactions can be monitored in real time [68], this is in comparison to more traditional sensing methods which may require laboratory preparation, and a high signal to noise ratio. Signal to noise ratios of greater than 64 dB have been reported, reducing for higher ion concentrations and bias conditions [60].

At the advent of ISFETs, the advantages of ion selectivity were already clearly understood [67] and ISFETs with an enzyme sensitive layer can be made sensitive to particular target materials [69]. In later literature, these have been called EnFETs [70]. Research into ISFETs has split into two sub-categories. Enzyme FETs (EnFETs) and Immuno FETS have been introduced alongside the more traditional ISFETs, and all three areas have generated significant interest [71,64]. An enzyme, which depends on the target molecules, is immobilised on the insulator surface of an ISFET to produce an EnFET [72]. Biosensors which utilise specific enzymes can be used in a variety of applications including medicine, environmental analysis, forensic applications and the food industry [70]. A diagram which attempts to separate the categories of sensor is shown in Figure 2.6. It is evident from this diagram that the separation of the sensor types is not always obvious, and the subcategories of ISFET can be particularly difficult to differentiate.

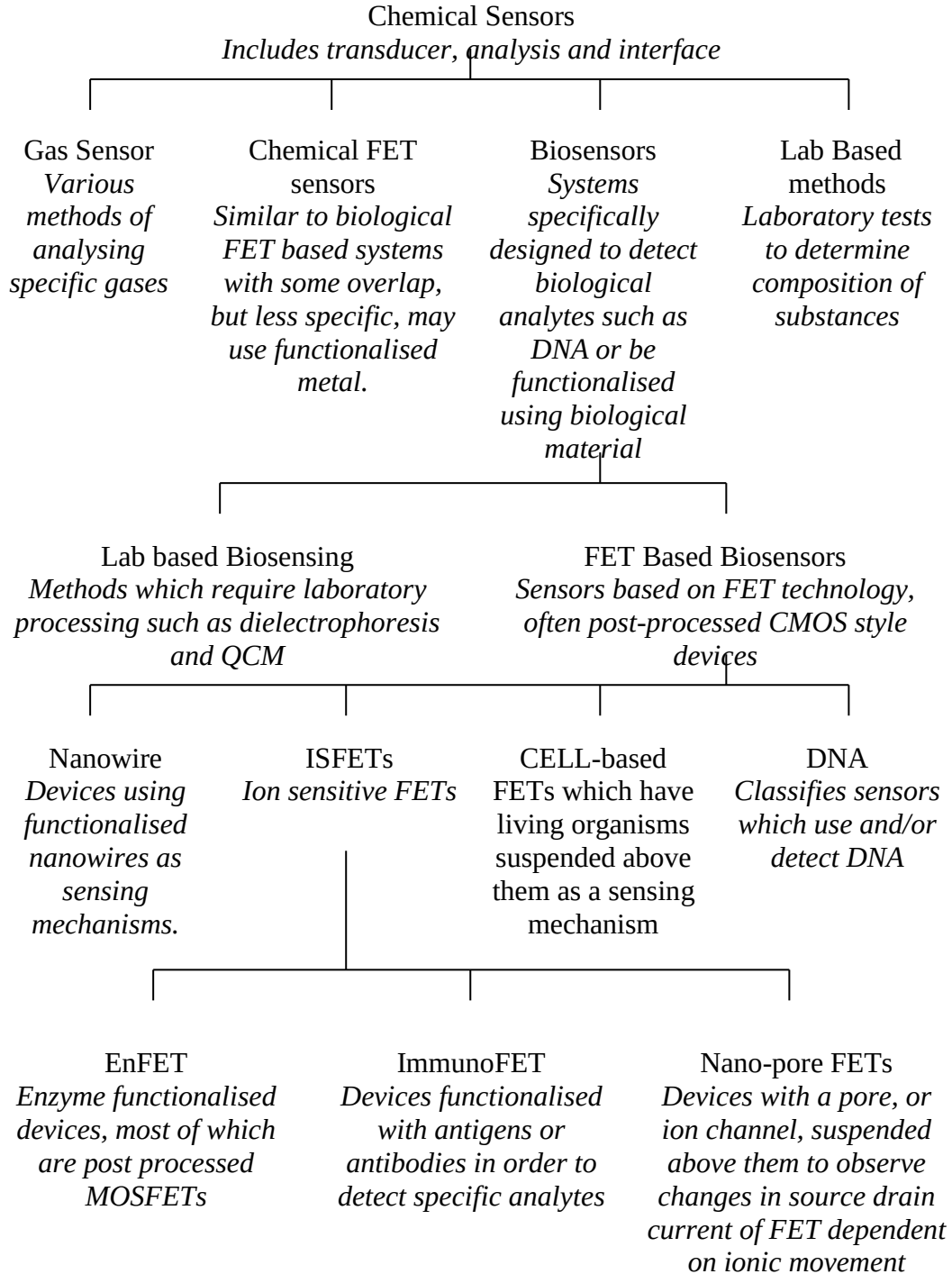

Figure 2.6 – Diagram showing types and sub-types of chemical sensor described in this work.

Additionally, some research has referred to ‘bioFETs’ which are structures comprising of a post-processed MOSFET where the metal gate is replaced with an electrolyte solution and a self-assembled monolayer deposited on the gate oxide which is used to affix biological molecules [60]. The inclusion of the bio-sensitive element in this way differentiates these de vices from traditional ISFETs, though the distinction between the subcategories is not always clear. As a result, bioFETs have not been included in figure 2.6 as they do not differ significantly from other types of ISFETS.

All of these FET based sensors require a low ionic concentration electrolyte solution, in the range of mM or lower, above the FET device and use differential measurements [46]. The low ionic strength means that the Debye length in the solution is greater than 300 nm (assuming <1 mM) and that mobile charge does not screen the interaction of the target molecule with the sensor and provides a strong signal to noise ratio [73,74] though the effect of mobile charges must be accounted for. It has been found that operating the FET in the sub threshold regime can enhance the signal to noise ratio by as much as 20% [41,60].

2.3.2.4 DNA Analysis

DNA sensors using FETs have already been demonstrated [75] and they demonstrate some similarities to EnFETs. Probe DNA is immobilised on the surface of the insulator of a FET. The hybridisation which will occur if the target DNA is present will then change the conductivity of the channel by changing the channel surface potential by ~4 mV, creating a change in source – drain current in the order of nA in the FET. This methodology can be particularly useful in

situations where a particular, known strand of DNA is being sought or tested for, though they lack the ability to detect and identify unknown strands.

As reported by Dekker it has been experimentally demonstrated that molecules may be sensed and interrogated by 'threading' them through artificially constructed nanopores [76] as shown in Figure 2.7, although this method has not, as yet, been used to sequence DNA. Due to the charge held by a strand of DNA, it may be possible to use a ~10 MVm^{-1} electric field in order to control the transit of the molecule through a nano pore. Furthermore, this research suggests that a solid state nanopore may have some benefits over more natural organic counterparts due to the stability of the pore and the extra degree of controllability afforded in the manufacturing process. This would, however, be at the cost of the inherent selectivity exhibited by natural ion channels.

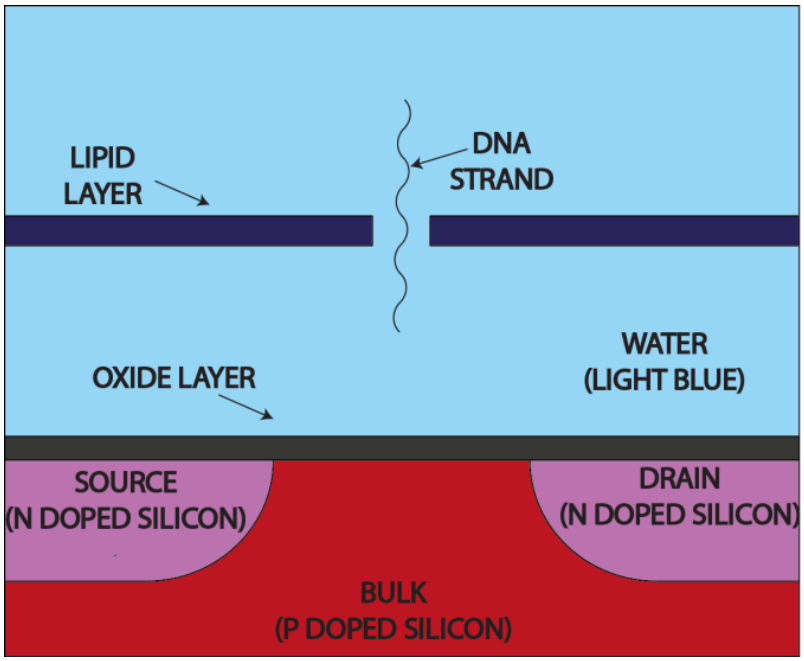

Figure 2.7 – Schematic of a strand of DNA being pulled through an artificial nanopore suspended above a FET.

At the turn of the millennium, 3×10^4 bases per day was the normal throughput of the most efficient DNA analysis tools. Rapid DNA sequencing (thousands of bases per second) could be achieved by utilising a nanopore sensor system [77]. In this case, however, it is essential that each base be accurately differentiated and identified in order to maintain accuracy while increasing throughput. Artificial and natural pores on the scale of nanometres are particularly useful in these types of assays as their physical dimensions ensure that only a single strand of DNA can pass through them at any time [76].

A particular future application of the work contained in this thesis is to model the transit of DNA through an ion channel or synthetic nanopore allied with a sensing FET [78]. The individual strands of DNA have molecular partial charges associated with the base pairs which make them up. These charges produce a strong enough electric field to affect the output of a FET based sensor in close proximity to the molecule [56]. In fact, simple FET based DNA sensors have been demonstrated where the modulations of FET drain current respond to the DNA molecules [28]. The use of simulation will be a key tool in the optimisation and development of such sensors in the future.

2.3.2.5 The Future of Biosensor Research

Much of the current nano-biosensor research is focussed on nanowire and nanotube research [79,56]. These devices operate on the premise that when a targeted molecule or molecules binds to a selective biological element which has been immobilised at the surface of the nanowire there will be a conductance change on the order of 1 nS. A specific example of this is where DNA probe samples have been attached to nanowires in order to detect specific DNA molecules as they bind to the probes. When the complimentary DNA is added to

the solution above the p-type nanowire, the conductance changes by up to 6 nS whereas when non-complimentary DNA is added, there is no observable change in conductance [80]. Similar work on nanowires has occurred in the field of cancer detection. Nanowire sensor arrays, with antibodies attached, have been used in the detection of targeted antigens which are associated with cancer [27]. This system detected much higher changes in conductance, up to ~150 nS, when specific protein markers were detected, though as a percentage of the original conductance, this is a similar change to that mentioned earlier.

It is often desirable to test for multiple targets simultaneously [37]. Future biosensors could be made up of an array of selective ion channels acting as sensors [81] which would allow the construction of portable integrated circuit based systems which are capable of real time diagnosis. Recently it, it has been demonstrated that semiconductor devices could be integrated with microfluidic channels, enabling a fast response in the order of seconds, with high throughput (thousands of pairs per second for DNA sensors, and individual samples taking less than one minute for individual screening tests) and greater accuracy when compared to traditional systems. Integrating these parts would allow single sensing systems to prepare, test and analyse a sample [82]. In order to realise these types of complex multi-physics based sensor platforms, extensive and accurate simulation of their constituent parts will have to form an essential part of the design process.

2.3.3 Summary

Sensors of various types are increasingly used in a variety of situations, and the trend of including biological elements to make them selective to specific analytes, or to investigate specific functions, is likely to continue. A wide array of sensing

technology already exists, with a range sensitivities from fM to mM depending on the function, and operating principles. Systems may use variations in mass to cause a ~2 Hz change in frequency, or alter electrical characteristics such as current (on the scale of nA), conductance (ranging from nS to 10s of µS) and threshold voltages in the range of 10s of mV.

This research focusses on FET based sensors which offer many advantages to the field of biosensors. Firstly, they respond directly to the charge of molecules. Additionally, FET technology allows post manufacture processing of existing devices to alter their functionality in such a way as to make them sensitive to specific analytes. Finally, they can be combined with CMOS based circuitry in a relatively simple manner allowing interpretation of the changes of drain current.

2.4 Simulation Techniques

In the past decade significant steps have been made in both the simulation and understanding of ion channels [83]. Computer simulation (or *in silico* experimentation) provides an efficient and relatively inexpensive method of investigation when compared to *in vivo* experimentation, which cannot take place on living subjects. The use of simulation allows multiple scenarios to be investigated simultaneously at low cost, for example engineered mutations of ion channels. They cannot, of course, replace physical experimentation, but do enable an initial development phase. Here, three widely used methods of simulation will be discussed.

In his review paper, Roux [83] suggests that molecular dynamics (MD) methods provide the most detailed information for the behaviour of biologically relevant molecules. However, he points out that, due to the fact that MD explicitly models the interaction of every atom in a simulation domain, they require prohibitive amounts of computation. Since, in order to model biological processes, μs of total model time are required with very short (sub femtosecond) time steps, the result is very long simulation times with significant computational demands [84].

While a significant proportion of the simulation studies of ion channel behaviour utilised molecular dynamics simulation methods, coarser grained approaches using Brownian dynamics simulation methods [5,85] have been demonstrated to be particularly good at replicating experimental measurements of the conduction of ions through channel proteins. Self-consistent Brownian dynamic (BD) methods are particle simulation methods which are based on Brownian motion [86,87] where the motion of charged particles is described by Langevin's equation coupled to an electric field solution containing both mobile and fixed charges. The field is calculated from the electrostatic potential which is calculated from the solution of a discretised form of the 3D Poisson equation. The drift diffusion approach is heavily used in semiconductor simulation [4] but is commonly known as the Poisson-Nernst-Planck, PNP, method within biological sciences circles [88]. In both cases this self consistently solves Poisson's equation (allowing for drift due to electric field) with a current continuity equation to describe the drift and diffusion of charge carriers.

2.4.1 Molecular Dynamics

In molecular dynamics (MD) simulations, every atom in the simulation domain is modelled explicitly, including the solvent, leading to very large number of particles in each simulation [15]. This method provides simulations which are capable of closely matching experimental results, but at a prohibitively large computational time cost [89]. The time that the simulations take is largely down to treating the water explicitly as individual atoms unlike the other methods mentioned in this chapter. This is beneficial, as a it results in stronger correlation with experimental results, but the interactions between each atom in the whole simulation domain increase the computational overhead. Arguably the most widely used technique, MD has provided great insight into the structure-function relationships of ion channels [90] at the atomic level.

Currently, the realistic maximum model time that a single MD simulation can encompass is in the region of 20 ns to 100 ns [91,92], but simulation times on the order of microseconds [93], or even in some cases as much as milliseconds are required to measure ionic currents on the order of pico-Amps [10]. The time constraints are due to the nature of the model, considering the interactions of individual atoms, often with large velocities, in a dense medium. The changes caused by the small movements over femtosecond timescales [85] mean that the individual time steps within an MD simulation must be smaller than this in order to correctly model the interactions. This accuracy makes MD ideal for investigating the behaviour of channel proteins but, when one considers that single ion transversal events occurring on the timescale of femtoseconds contribute to the macroscopic behaviour of channel proteins [11], simulations would require 1,000,000,000 1 fs time-steps in order to investigate the behaviour of the ion channel over a period of 1μs. Each of these time-steps would require

full resolution of the interactions between more than 4000 atoms for a 5 nm^3 cube of water. It is obvious that, despite the massive increase in the computational power of modern high performance computer systems, MD simulations do not yet offer a realistic option for comprehensive investigation of the conduction behaviour of ion channels. As a result, they will not be used in this research.

2.4.2 Brownian Dynamics

In Brownian dynamics simulations of ionic solutions the behaviour of every mobile ion and atom in the protein structure can be modelled explicitly, but the water in which they are solvated is assumed to behave as a continuous medium. For this reason it is faster than molecular dynamics as there are significantly fewer particles to model in each time step. Brownian motion models the transfer of thermal kinetic energy which occurs between atoms through the inter particle collisions [3]. Like the other two methods described here, Brownian dynamics has already been widely implemented in the analysis and simulation of ion channels [85,94]. It is possible to use this methodology over larger timescales than MD simulations – ranging from tens of ns to the low thousands of nanoseconds (depending on simulation domain and mesh size and particle concentration). This, though, will still take weeks or months to complete compared to hours or days for simulations based on the drift diffusion approach. The Brownian dynamics (BD) simulator used in this work self consistently solves Poisson's equation and a positional form of Langevin's equation, both of which will be discussed in the following chapter.

There has, however, been work where the equations are not self consistently solved. Instead, Brownian dynamics simulations can be performed with the electric field due to the charge and image potential caused by each individual ion and the external field due to fixed charges and applied potentials. The additional electric field due to interaction between ions is then calculated during each time step and a total vector used when calculating the solution to the Langevin equation [95,5]. This has the effect of reducing the computational overhead required to find a solution, but does mean that fluctuations caused in the overall field may not be taken into consideration when calculating the movement of each individual ion.

Recently, work has been performed into stochastic models which attempt to include the Brownian motion and changing diffusion constants in gating ion channels [96]. Furthermore, Brownian dynamics ion channel simulations which model a single voltage point over 1 μs were shown to take approximately seven days on a single 2.4 GHz processor [18]. These simulations modelled the 0.5 nm (minimum) pore of a mutant α-haemolysin channel which is 10 × 10 × 10 nm at its largest point within a 30 × 12.8 × 12.8 nm simulation domain.

2.4.3 Drift Diffusion

The drift diffusion simulation approach (DD), also known as Poisson-Nernst-Planck or PNP approach, has been widely used in semiconductor device modelling for more than 25 years [97,4]. Due to the fact that the particle nature of ion conduction is of importance in ion channels, continuum methods have been

found to differ from their particle counterparts when modelling ion transport, even though they are accurate in many other situations [98]. This is due to the fact that continuum methods do not resolve important single events - especially in narrow channels where the position and charge of individual carriers have a large effect. The percentage difference in measured conductance of sodium in BD and DD simulations ranged from 10% in >0.9 nm pore radii to more than 200% in <0.5 nm pore radii [99]. In MOSFET simulation, for example, the current observed is due to a large number of carriers ($\sim 10^{24}$ m^{-3}), whereas in protein channels, the current is due to single ion transport events separated by ~μs periods of time relative to the time taken for the ion to traverse the pore.

Some PNP simulations have produced results better matching experimental measurements than their Brownian dynamics counterparts, but these have required significant calibration of the physical parameters associated with mobile ions, such as reducing the mobility by several orders of magnitude. This improved comparison with experiment may be due to two errors in these simulations compensating for each other [100]. Additionally, it has been found that when ion channel proteins were simulated with DD, reduction of the Diffusion coefficient in the channel yields a more accurate representation of the current [101]. The issues faced when simulating ion channels using the PNP approach are borne of the continuum nature of the simulation which, while having sufficient flexibility to allow calibration to experimental data [102,17], lacks predictive ability since it fails to capture the discrete nature of ions.

Though, in the past, drift diffusion methods were partly chosen for reasons of efficiency [103], the computational power available in modern systems has increased greatly and so BD simulations on a larger scale are now possible, allowing greater agreement with experimental results than can be expected from

continuum methods which may not allow observation of important events - especially in narrow channels [99].

2.4.4 Combined Simulation Domains

The combination of Brownian simulation and MD could provide accurate simulation of biological molecules [90]. In this work it is proposed that the combination of two simulation techniques is both capable and necessary to accurately model biological systems. However, the accurate description of particle motion and behaviour from BD models and the computational efficiency of drift diffusion models is more likely to be realistically useful due to the ability of such simulation methods to model biologically relevant timescales with close to single atom/ion accuracy. It has been pointed out that computational efficiency is also essential in BD simulation as simulations must be on the μs scale to obtain statistically reliable results due to the pA scale currents involved in ion channel simulations when investigating ion channel gating [104].

The interfacing of particle and continuum simulation methods has been attempted before, but few examples of extensive reliable implementation exist [105,103]. In both cases where a reliable coupling methodology was demonstrated, this was in 2D simulations, combining electron Monte Carlo and drift diffusion methods. In this work, an alternative particle method—Brownian dynamics simulation of the biological portion of a simulation domain—will be coupled with drift diffusion simulation of a semiconductor sensing transistor. The principal test bed for the

simulation methodology will be a model bio-sensing device where a model ion channel acts as the gate of a nano-scale semiconductor MOSFET.

In Kosina and Selberherr's research [103], the combination of MD and DD is used to model the areas where DD overestimates the mobility of charge carriers – i.e. in high field areas. In order to avoid the effects of a large field at boundary conditions where the particle method begins, an overlap method is used to gradually move from particle to continuum. The smallest device in the research is 150 nm which is considerably larger than the whole domain considered in this work. Additionally, the coupling occurs through the charge distribution which, in three dimensions, would be significantly more difficult. As a result, this research restricts coupling to the potential through the device, and the coupling occurs across an insulating layer to avoid a direct boundary between charge as discrete particles and as a continuum.

The method of Cheng *et al* [105] for integrating the two approaches is for a relatively large scale device by modern standards – 400 nm. This technique involved using DD in most sections of the device, but including MD in areas of high electric field through the current flowing towards contacts. This method required the calculation of currents in multiple planes around an MD 'window'. In future research, it is suggested that a similar method, ensuring consistency of charge density, be used to fully couple a BD and DD simulation – therefore allowing more efficient analysis of the general ionic flow in water without losing the important single ion detail in an ion channel region. This would, however, present significant challenges in the injection and removal of particles based on boundary conditions. This research focusses on the ability to combine the two methods in a more simple framework. In order to simplify the initial integration of these two simulation methods a system where the coupling of the two simulation

domains is through the electrostatic potential will be adopted. This will allow bio-nano-devices such as that demonstrated in Figure 2.8 to be investigated, though current research is limited to a synthetic nanopore. In this situation electronic devices will be simulated by DD and the ion based regions by BD, best utilising the strengths of both methods.

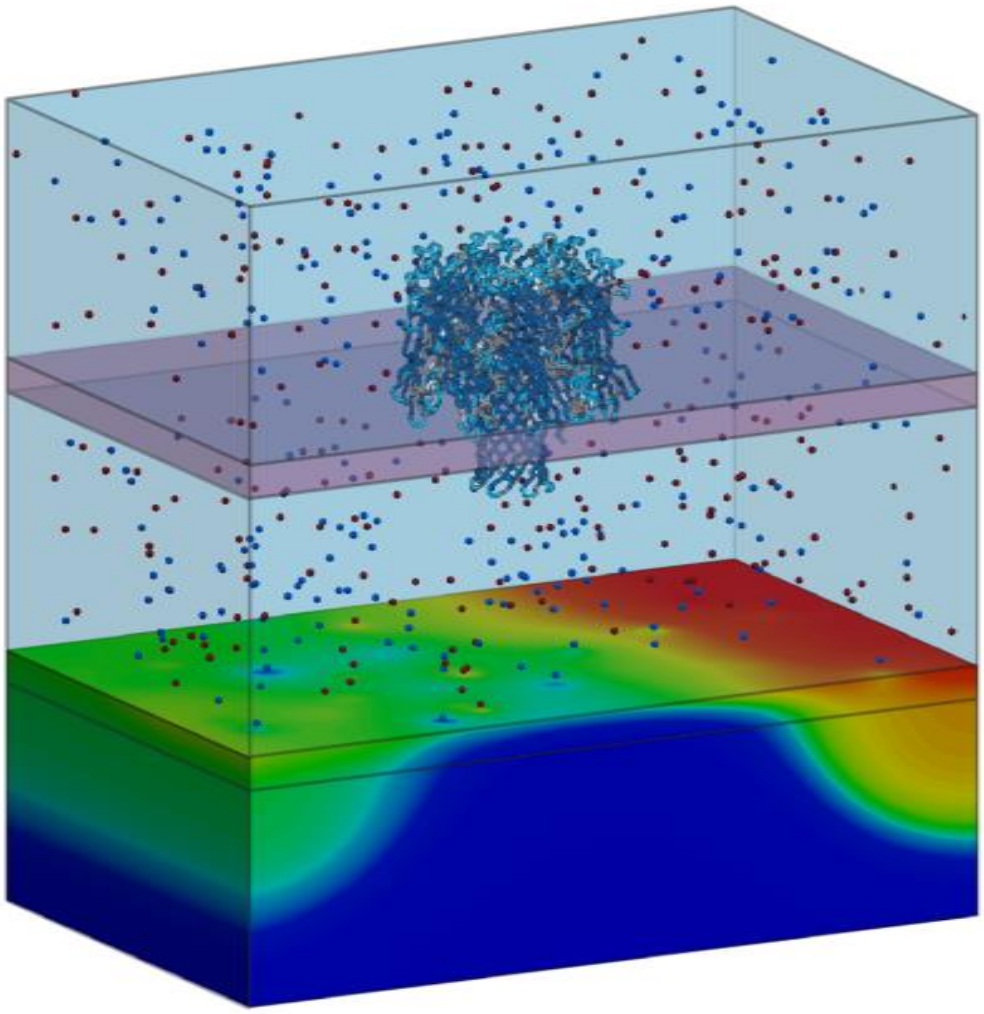

Figure 2.8 - Cartoon showing the simulation domain including concentrations of ions above and below a lipid membrane suspended above a nano-scale FET. An ion channel is embedded into the lipid membrane to allow controlled ion permeation through the lipid layer.

Chapter 3

Simulation Methodology

3.1 Introduction

This chapter describes the numerical techniques used to develop the integrated ion-channel-transistor simulator which is the focus of this research. The focus is on the integration of particle and continuous simulation techniques in a single simulation domain. The two simulation techniques, Brownian dynamics and drift diffusion, provide the essential capabilities necessary to accomplish the aim of this research which is the simulation of a bio-interface between nano-scale pores and semiconductor devices. By capturing the transport of discrete ions in an aqueous solution and joining this with a more computationally efficient solution in a semiconductor device, a single simulation domain offers the simultaneous benefits of two methodologies. The schematic of the target structure that is to be simulated is shown as in Figure 3.1 where the gateless field effect transistor (FET) would be simulated using drift diffusion, and the electrolyte and channel region would be simulated using Brownian dynamics.

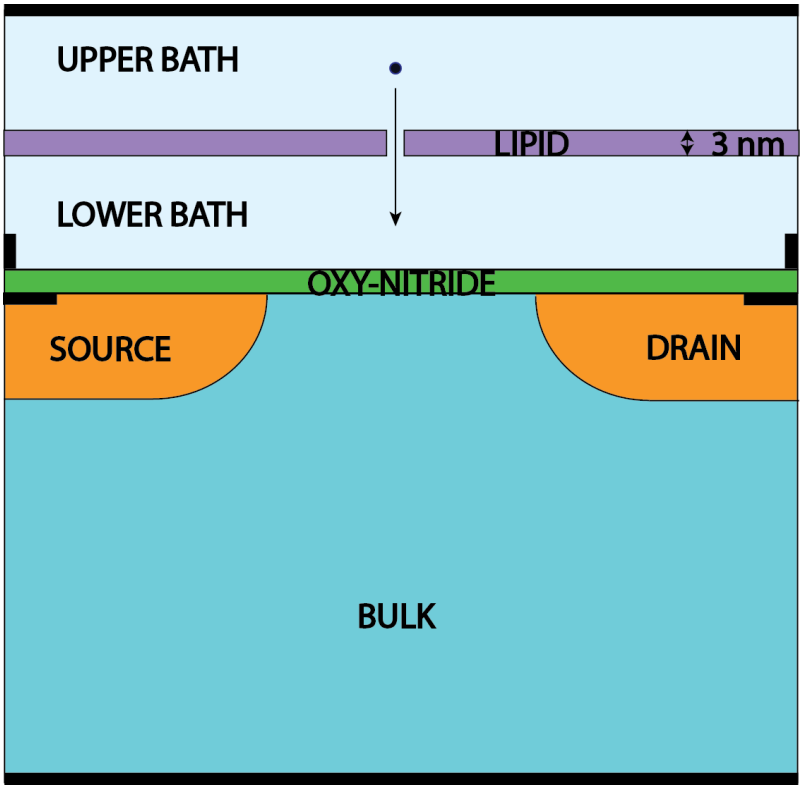

Figure 3.1 – Proposed structure of the simulation domain – the upper section modelled using Brownian dynamics, and the FET structure modelled using drift diffusion combined in a single domain.

The first section of this chapter covers Brownian dynamics. This is a particle simulation method based on the Langevin Equation which describes charge transport, whilst employing the linear Poisson equation to capture the electrostatics of the problem and the interactions between the particles. It is well suited for capturing the physics of systems where the transport of discrete charges is important. This simulation type will be used for sections of the simulation domain where it is desirable to resolve the effect of individual particles.

The next section describes the more common self-consistent Drift diffusion simulation technique, where the current continuity and the non-linear Poisson equations are solved self consistently to capture charge transport. This method is intrinsically more computationally efficient, but fails to capture all the physics of discrete charge transport. In the semiconductor section of our final simulation domain, this simulation method is used to investigate the charge transport within a more traditional semiconductor device.

The formulation of both simulation approaches will be described, including the discretisations of the governing differential equations into sets of algebraic equations, and the iterative approaches used to approximately solve the corresponding algebraic equations.

3.2 Brownian Dynamics

In this section some of the important elements of the Brownian simulator are described. The Brownian simulation approach is based on the Langevin equation which describes the discrete charge transport, and is discussed first, including the method used to introduce the stochastic aspects of the simulation which is critically important in implementing the Brownian simulation approach. In addition to an accurate calculation of the charge transport, the electrostatics of the simulation domain and the particle interactions must be calculated at each transport time time-step. The linear Poisson equation, which is used to perform this calculation is then discussed.

3.2.1 The Langevin Equation

The stepping stone in the development of the Brownian simulator was the implementation and testing of a simple Brownian simulation algorithm to act as a foundation to the full scale simulator used in this study, and to improve the understanding of the dynamics of the system. The basic simulator models the movement of a single particle according to the Langevin equation, which describes the behaviour of particles in a solution, and will be used to describe the behaviour of ions in this work. The original Langevin equation describes the motion of ions in a viscous fluid taking into consideration the random thermal motion of the ions and the drag of surrounding fluid. Equation 3.1 is a modified version [106] of the equation which not only accounts for the thermal motion and drag, but also the Coulombic interactions between particles and the externally applied electric field. This modification is important as, when looking at particles in such concentrations over a small area, the interactions between the individual particles play a significant role in their motion.

(3.1)

$$m\frac{d\boldsymbol{v}(t)}{dt} = q\boldsymbol{E}(\boldsymbol{r},t) - \frac{m\boldsymbol{v}(t)}{\tau} + \boldsymbol{F}(t)$$

(3.1)

In equation (3.1) , m is the mass of the particle, $\mathbf{v}(t)$ is the particle's velocity, $\mathbf{E}$ is the electric field, q is the charge on the particle and $\mathbf{F}(t)$ is a rapidly fluctuating random force caused by stochastic kicks from the molecules of the surrounding solution which, over a long enough time, will average to zero. Finally, τ is the momentum relaxation or average free flight time, which is the time it takes for the average velocity of the ion to reach $1/e$ of its equilibrium value after a step

application of electric field [3]. The momentum relaxation time is due to the damping of acceleration due to the viscous fluid causing friction. It is defined by the equation $\tau \equiv \frac{m\mu}{q}$. The mobility, which is a measure of the response of a charged particle to an electric field, can be calculated, using the Einstein relation from the diffusion coefficient, shown in equation (3.2) where k_b is the Boltzmann constant and T is the temperature.

$$D = \left[\frac{k_b T}{q}\right]\mu \tag{3.2}$$

The right hand side of equation 3.1 an be split into three components. The first, $q\mathbf{E}(\mathbf{r}, t)$, represents the combined forces on the ion from the applied electric field and the field due to other particles. The second, $\frac{m\mathbf{v}(t)}{\tau}$, represents the interaction of the ion with the medium it is passing through since m/τ represents a ratio which gives the proportion of velocity lost to friction. The final component, $\mathbf{F}(t)$, represents the stochastic force which is associated with molecular collisions as previously mentioned.

As described in [106] and [3] equation (3.1) can be discretised with respect to time to give

$$\mathbf{v}_{n+1} = \gamma\mathbf{v}_n + \frac{q}{m}\mathbf{E}_n\Delta t + \Delta\mathbf{V} \tag{3.3}$$

where γ is the equivalent of the frictional coefficient in discrete time given by equation (3.4).

$$\gamma = \left(1 - \frac{\Delta t}{\tau}\right) \tag{3.4}$$

Again, equation (3.3) can be split into its three constituent parts. The first, $\gamma \mathbf{v}_n$, is the relaxation in velocity over the time step due to friction. The second, $\frac{q}{m}\mathbf{E}_n \Delta t$, represents the change in velocity due to electric field, combining both the applied electric field, and the local field due to other particles. The last term, $\Delta \mathbf{V}$, represents the change in velocity due to stochastic kicks. It is given by the integration of the random fluctuations from equation (3.1).

$$\Delta \boldsymbol{V}(t) = \frac{1}{m}\int_{t}^{t+\Delta t} F(t')dt' \tag{3.5}$$

This requires separate integration from the other parts of the equation due to the rapid nature of fluctuations on any timescale. As described in [3] the result of $\Delta \mathbf{V}$ is the integral of a large number of un-correlated random events and so can be described by a Gaussian distribution, as suggested by the central limit theorem. The result averages to zero over time and can be viewed as a random walk in velocity space. The resulting Gaussian distribution has a variance which is related, through the diffusion length, to the diffusion coefficient as shown in equation (3.6).

$$\langle(\Delta \boldsymbol{V}(t))^2\rangle = 2D_v\Delta t = 2\frac{k_b T\Delta t}{m\tau} \tag{3.6}$$

Where the diffusion length in velocity space, D_v, is related to that in real space, D_x, over short timescales by the equation $D_v = \frac{D_x}{\tau^2}$ [106].

The discrete form of the Langevin equation, shown as equation (3.3), is only valid in a regime where the time step, Δt, is much smaller than the momentum relaxation time τ. Figure 3.2 shows the behaviour of a single particle in response

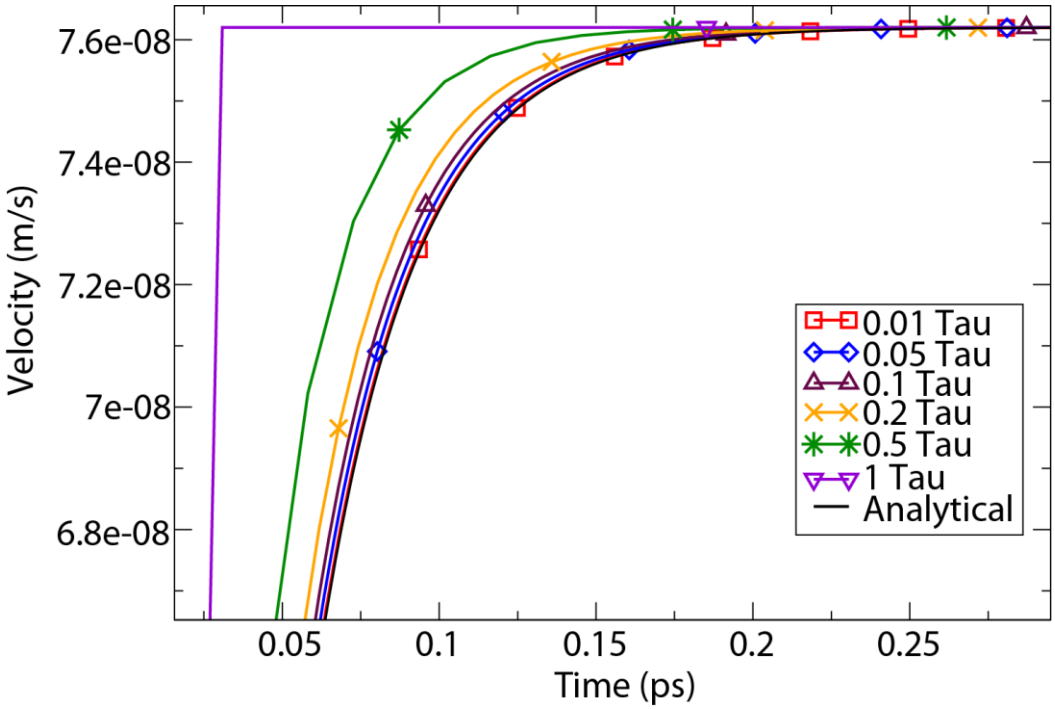

Figure 3.2 - Velocity of a single particle when a unit step electric field is applied at time $t = 0$. The various values of time step show how a smaller time step allows greater accuracy when compared to the analytical solution. A time step equal to the momentum relaxation time poorly represents the analytical solution.

to a unit step electric field when the stochastic component of the equation is omitted. Its behaviour can be accurately described analytically, and therefore comparison between this analytic response and the responses from simulation using varying time steps indicates the relative accuracy of using different τ values in the numerical solution.

Note that as the time step is reduced, the number of times equation (3.3) must be evaluated in order to reach the same overall simulation time increases. To illustrate this, Figure 3.3 shows the percentage error at 5τ as a function of the time step. It is clear that the time step of $0.1\,\tau$ provides a significant increase in

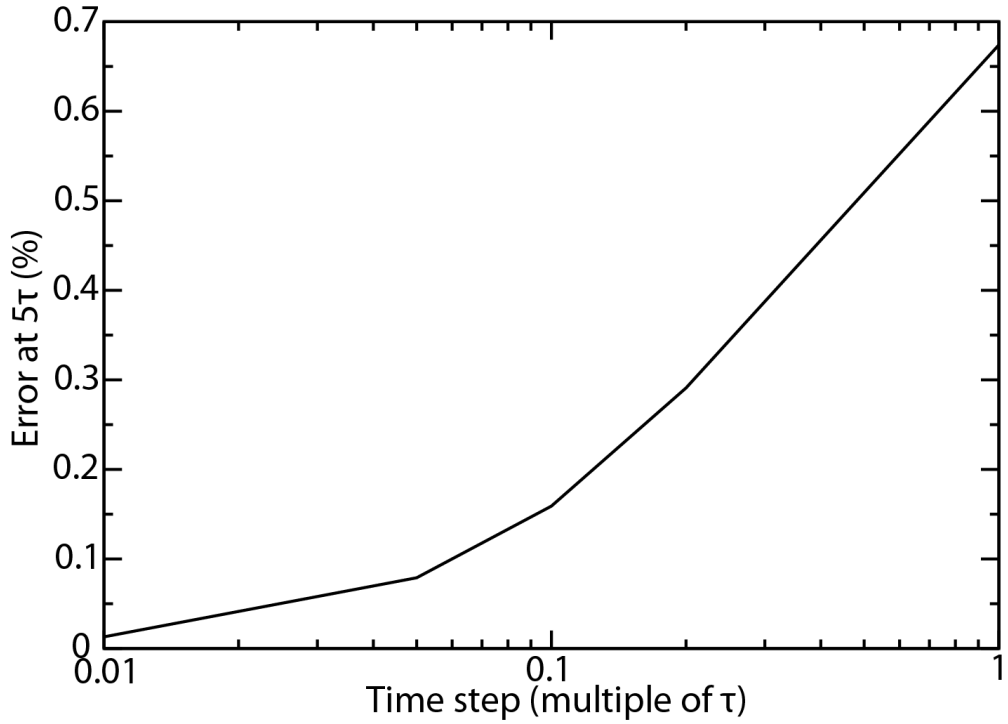

Figure 3.3 – Error in the velocity of a single particle when a unit step electric field is applied at time $t = 0$. The various values of time step show how a smaller time step allows greater accuracy when compared to the analytical solution. A time step equal to the momentum relaxation time poorly represents the analytical solution.

accuracy compared to $0.5\,\tau$ time step, at the price of approximately 5 times increase in computational time. The $0.01\,\tau$ trace compared to the $0.1\,\tau$ trace shows a much smaller increase in accuracy, with a much larger increase in simulation overhead (approximately 10 times). This shows that there is a diminishing return from a reduction in the time-step. It is important to note that the error in simulation as a function of time step could be additive meaning that the larger at times greater than 5τ the percentage error may increase. This is taken into consideration when deciding what constitutes a "large" error since none of the simulations in figure 3.3 show an error greater than 1% after 5τ .

The stochastic element of equation (3.3) can be introduced using a random number generator to create random velocity vectors. In this case, Ran4 was selected from Numerical Recipes [107] which has a long period and high quality random deviates [3] when compared to computationally quicker schemes such as Ran2 which already has a period longer than 2×10^{18}. Ran4 generates numbers with a random distribution which were converted to a Gaussian distribution with a zero mean using the Box-Muller transformation [108].

These stochastic velocity vectors were added to the overall velocity, the result of which can be seen in Figure 3.4 and Figure 3.5. The mean velocity does not change, but the instantaneous velocity after equilibration varies due to the stochastic kicks.

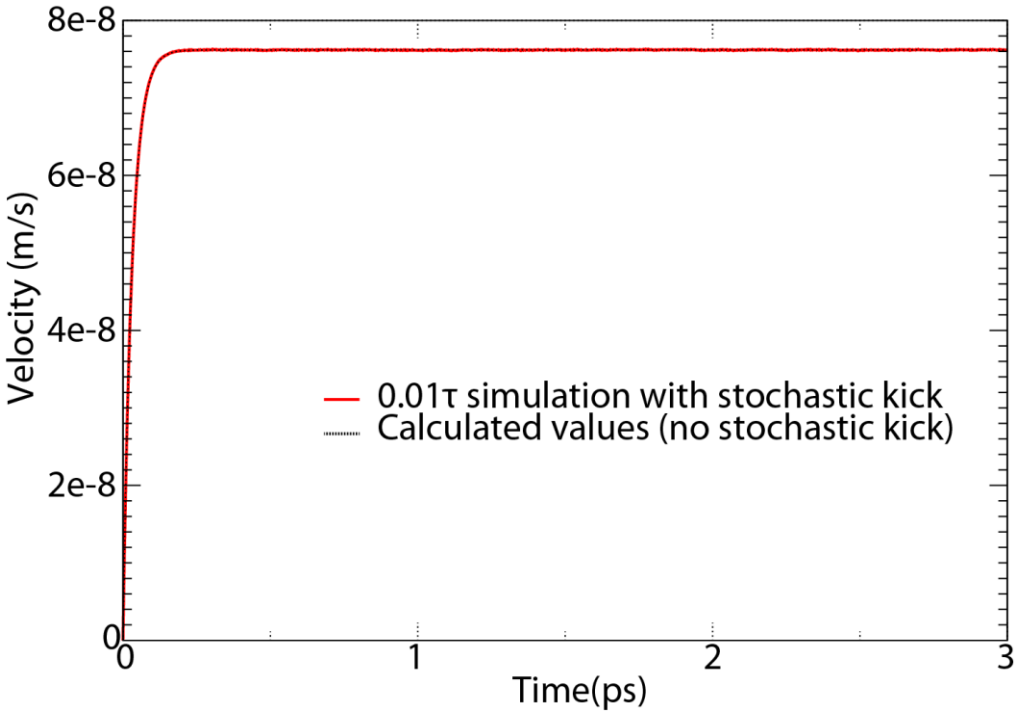

Figure 3.4 - Velocity of a single ion subject to a unit step in electric field at time t=0. This simulation was performed with a time step of 0.01τ. This trace shows the full simulation, showing that the 'steady-state' velocity is approximately constant.

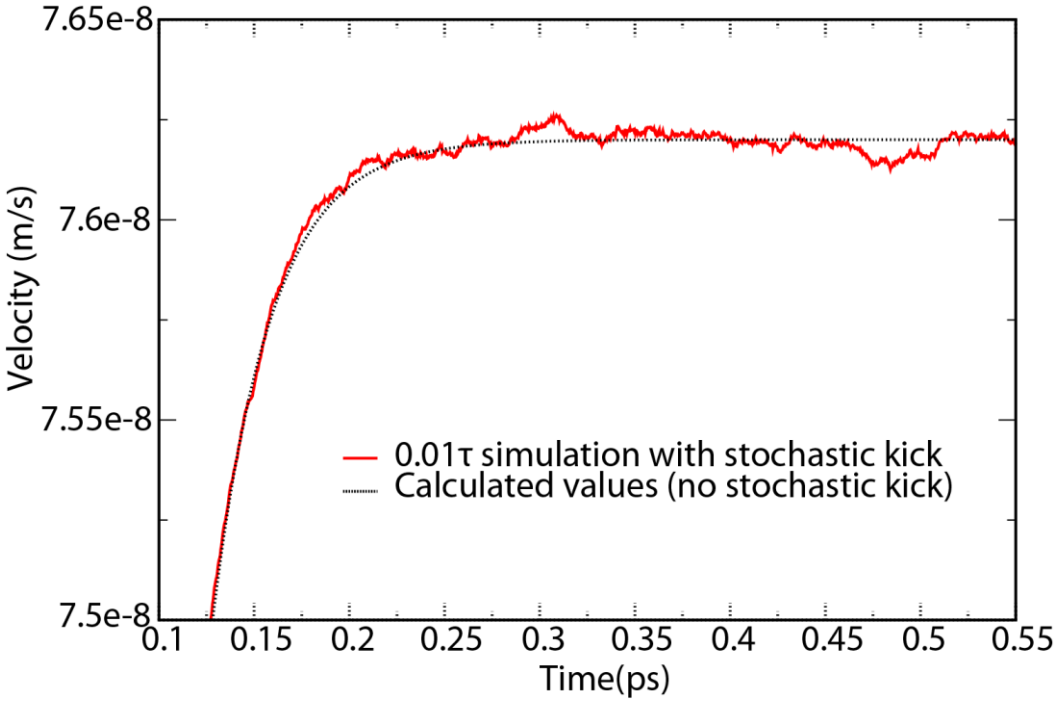

Figure 3.5 – Close-up view of the velocity of a single ion subject to a unit step in electric field at time t = 0. This simulation was performed with a time step of $0.01\,\tau$. This shows a closer image of Figure 3.4 showing the small variance caused by the random stochastic kicks. The random stochastic kicks have almost no effect on the general shape of the curve as can be seen by the similarity to Figure 3.4.

Equation (3.3) can be integrated to give Equation (3.7), a discrete analogue of the Langevin equation in the positional space, rather than in the velocity space.

$$x_{t+1} = x_t + \mu \boldsymbol{E}(t)\Delta t + \Delta \boldsymbol{X} \tag{3.7}$$

x is the position of the particle at time t, μ is the mobility and $\Delta\mathbf{X}$ is the change in position caused by the integration of each of the stochastic kicks in the velocity space which is given by a Gaussian distributed Wiener process described by

$$\langle(\Delta \boldsymbol{X}(t))^2\rangle = \sqrt{2D_v\Delta t} = 2\frac{k_b T_\tau \Delta t}{m} \tag{3.8}$$

where D_x is the diffusion coefficient in real space with units $m^2 s^{-1}$. [3]

Again, as with equation (3.3), certain criteria must be satisfied in order for this equation to remain accurate. $\Delta\mathbf{X}$ must be small enough to resolve the changes in the electric field correctly, and Δt must be chosen to be large allow particles to come close to the equilibrium velocity. If Δt is chosen to be close to τ, the velocity will only reach 63% of $\mu\mathbf{E}$, the equilibrium velocity. For time steps greater than 5 τ, a velocity within 1% of the equilibrium velocity will be obtained. The fulfilment of the above conditions allows the simulator to be both stable and accurate when using relatively large time steps resulting in significant computational efficiency. The disadvantage, of course, is that the velocity distribution of the particles is completely lost.

3.2.2 The Linear Poisson Equation

The Poisson equation couples the particle motion to the long range electrostatics of both its surrounding particles and the externally applied potential.

$$\nabla.(\varepsilon_0 \varepsilon_r \nabla\psi) = -\rho \tag{3.9}$$

where ψ is the electrostatic potential, ρ is the charge density and ε_r and ε_0 are the relative dielectric permittivity of the material and the permittivity of free space respectively. It is essential to solve this equation after each time step since the particle positions change, and different materials are present with the dielectric permittivity changing rapidly throughout the system.

The discretisation of the Poisson equation, (3.9), is carried out using a box integration method illustrated in Figure 3.6. This results in a system of algebraic equations given by

$$\frac{\partial}{\partial x}\left(\varepsilon_{(x,y,z)}\frac{\partial\psi_{(x,y,z)}}{\partial x}\right) + \frac{\partial}{\partial y}\left(\varepsilon_{(x,y,z)}\frac{\partial\psi_{(x,y,z)}}{\partial y}\right) + \frac{\partial}{\partial z}\left(\varepsilon_{(x,y,z)}\frac{\partial\psi_{(x,y,z)}}{\partial z}\right) = -\rho_{(x,y,z)} \tag{3.10}$$

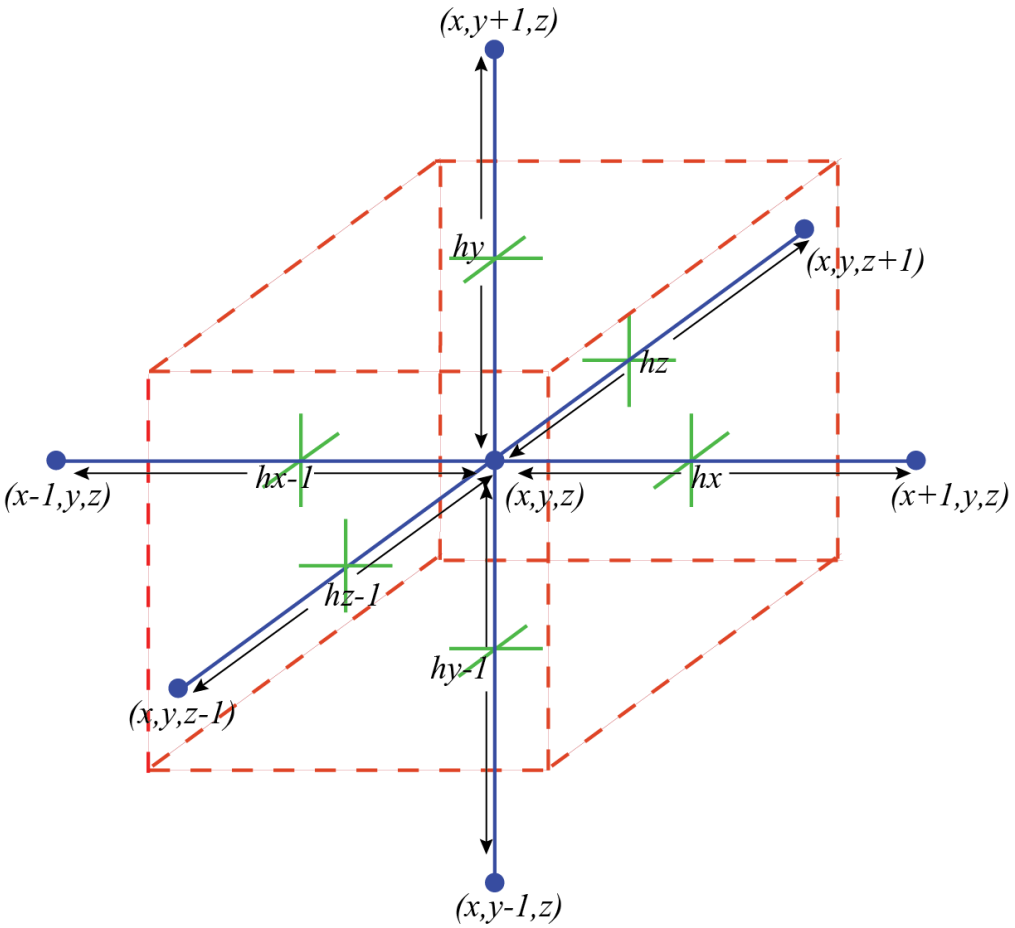

Figure 3.6 - Gaussian box discretisation for three dimensions. This scheme, is used to work out the components for each node depending on seven nodes, the node itself and those one mesh spacing forward and back in each dimension.

It is possible to use a finite difference or a finite element technique for the discretisation of equation (3.10). In this work, finite difference is used to simplify the numeric of the solution. Using this scheme, the equation for each node is given by equation (3.11) where h is the size of the mesh in each direction.

$$
\begin{aligned}
&-\rho_{(x,y,z)}hxhyhz \\
&= \frac{\left(\varepsilon_{(x-1,y,z)}\psi_{(x-1,y,z)} - 2\varepsilon_{(x,y,z)}\psi_{(x,y,z)} + \varepsilon_{(x+1,y,z)}\psi_{(x+1,y,z)}\right)}{hx} hyhz \\
&+ \frac{\left(\varepsilon_{(x,y-1,z)}\psi_{(x,y-1,z)} - 2\varepsilon_{(x,y,z)}\psi_{(x,y,z)} + \varepsilon_{(x,y+1,z)}\psi_{(x,y+1,z)}\right)}{hy} hxhz \\
&+ \frac{\left(\varepsilon_{(x,y,z-1)}\psi_{(x,y,z-1)} - 2\varepsilon_{(x,y,z)}\psi_{(x,y,z)} + \varepsilon_{(x,y,z+1)}\psi_{(x,y,z+1)}\right)}{hz} hxhy
\end{aligned}
\tag{3.11}
$$

To solve the Poisson equation, the simulation domain is divided into a particle particle particle mesh (P3M) system [109] with a mesh spacing which can be varied non uniformly on each axis to allow finer meshing in areas of most interest but greater computational efficiency from a coarse mesh in areas with a low rate of change. A 3D example of the discretisation is shown in Figure 3.6. The Poisson solution mesh is discretised by summing the field contributions from the six surrounding cardinal points for each cell, providing a coefficient for each mesh point which is used to calculate the potential at each node.

3.2.3 Charge Assignment

An accurate solution of the Poisson equation requires that the charge in the system is carefully described. Interpolation must be used in order to assign single point charges associated with individual ions to the Poisson solution mesh. There are various methods available to accomplish this task, the simplest if which is the

nearest grid point (NGP) approach. In this approach, the full charge of an ion is assigned to the nearest node on the mesh. This is simple to perform computationally, especially on a uniform mesh, and has a great advantage in that it best describes the single point nature of the charge. However this leads to a serious problem – the position of the point charge in the solution is not the position of the point charge in the system. [4] This can lead to serious errors in the simulation including those induced by self-force. Self-force errors occur when a particle which is not directly on a node experiences the effect of its own electric field which has been assigned to a local node. This means that the particle will shift position during the next time step.

For the above reasons, an alternative charge assignment method was used in this work called cloud in cell (CIC). It requires more computation, but provides greater simulation accuracy as it better describes the position of the particle. CIC, illustrated in Figure 3.7, assigns a weight of a charge q_p with position $p_{(x,y,z)}$ to the eight grid points surrounding a point charge based on equation (3.12).

$$\rho_{(x,y,z)} = \frac{q_p}{v_{(x,y,z)}}\left(1 - \frac{|x - p_x|}{h_x}\right)\left(1 - \frac{|y - p_y|}{h_y}\right)\left(1 - \frac{|z - p_z|}{h_z}\right) \qquad (3.12)$$

CIC loses the point charge nature of a particle, and the effective ‘size’ of the particle is directly dependent on the grid spacing. However, the errors involved are reduced compared to that of NGP, and it does retain information about of the relative position of the particle to the grid [109]. Additionally, this technique can be utilised for any rectilinear grid, and allows the introduction of non-uniform

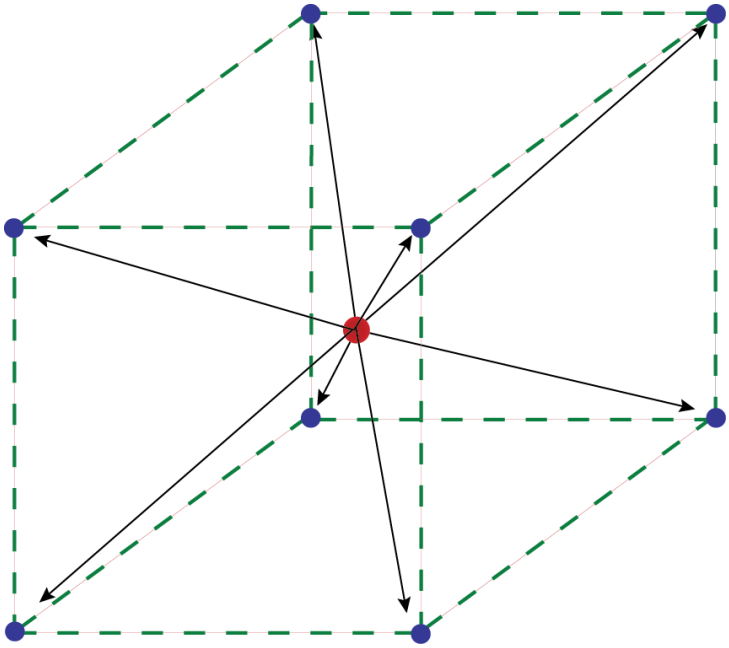

Figure 3.7 – Cloud in cell charge assignment system. The total size of the charge on the particle at the centre of the box will be assigned, proportional to the distance, to each of the surrounding mesh points.

spacing. The improvement in charge description when compared to the computational overhead makes this an attractive option for charge assignment.

However, problems are still apparent with this method. If a charge is close to a particular node, the system will closely resemble the NGP method, and the self-force will remain an issue. Overall, though, CIC allows for a better description of the charge in a system while significantly reducing the errors associated with NGP.

3.3 Drift Diffusion

This section introduces the drift diffusion simulation technique. drift diffusion is used in combination with the Brownian dynamics simulation in this work with the intention of improving computational efficiency, while allowing the description of discrete ions in a solution.

In semiconductors, the amount charge available for transport included in the right hand side of the Poisson equation can often be considered as continuously distributed charge with space dependent density, $\rho(x)$. The mobility of the mobile charge carriers in the semiconductor region is also significantly larger compared to that of ions in an aqueous solution. The impact of the current charge density on the potential distribution necessitates the solution of the non-linear Poisson equation self-consistently with the Current Continuity equations which are used to describe the charge transport in Drift Diffusion.

The system of drift-diffusion equations includes the non-linear Poisson equation, and the current continuity equations which are described below. Finally the iterative methods employed in the drift diffusion simulation will be discussed at the end of this chapter.

3.3.1 Gummel Iteration

Gummel iterations are used to provide unconditionally stable solutions to the drift diffusion set of equations [110]. In this case, the non-linear Poisson equation and

the current continuity equation for electrons are iterated self-consistently (and each equation itself is also solved using iteration). Each equation must be solved iteratively on its own, before repeating a solution to the other. In this way a final, self-consistent, solution is reached.

In the Gummel iterations, the Poisson and current continuity equations are linked through the quasi Fermi level. Initially the quasi Fermi level is approximated in the different regions based on the bias conditions. After the solution of the current continuity equations, the quasi Fermi level is extracted based on the new carrier and potential solution and the non-linear poisson equation is solved again. The process is then repeated, recalculating the quasi-fermi levels before each solution to the Poisson equation. This system continues until a predefined tolerance in the solutions of both equations are reached in the same iteration.

In the case for both current continuity and the Poisson equation, the simulations in this research were performed with the maximum number of iterations set to 1000. The tolerance was set to 1×10^{-8} for the Poisson solution and 1×10^{-12} for the current continuity equation. These are small values which ensure that the changes in charge density and electric field at each node change are multiple orders of magnitude smaller than the magnitude of the values. As noted, each equation is solved individually using a separate iterative method, as will be described in the following section.

3.3.2 Non-Linear Poisson Equation

As with the Brownian dynamics simulation technique, the Poisson equation must be solved when using the drift diffusion simulation approach. In both cases the

Poisson equation is self consistently coupled to the charge distribution, but in the drift diffusion case, the relationship between the potential and the electron and hole charge density is provided by the Boltzmann statistics;

$$\nabla.(\varepsilon_0\varepsilon_r\nabla\varphi) = q(n - p + N_A - N_D) \tag{3.13}$$

The differential operator $\nabla.(\varepsilon_0\varepsilon_r\nabla\varphi)$, is the same as equations (3.9), (3.10) and (3.11). On the right hand side of the equation n and p denote the concentration of electrons and holes, which depends non-linearly on the potential, while $N_D$and N_A denote the concentration of donors and acceptors. Assuming Boltzmann statistics, equation (3.13) can be expanded to explicitly show the detail of the dependence of n and p on the potential, φ;

$$\nabla.(\varepsilon_0\varepsilon_r\nabla\varphi) = q\left(n_i e^{\frac{q(\varphi-\phi_n)}{k_BT}} - n_i e^{\frac{q(\phi_p-\varphi)}{k_BT}} + N_A - N_D\right) \tag{3.14}$$

where n_i is the intrinsic carrier concentration of the material, ϕ_n and ϕ_p are the quasi n and p fermi levels respectively, k_B is the Boltzmann constant and T is the temperature in Kelvin. As the electron and hole concentrations depend on the current flow driven by the electric fields, the Poisson equation must be solve self consistently with the current continuity equation that describes the current flow.

In order to solve this equation in must be discretised and linearised. To reach a solution the equation is reduced to

$$Ax = b \tag{3.15}$$

where A is a matrix of size $n \times n$ where the size of n is dependent on your simulation mesh and is equal to the product of the number of nodes in each dimension, x is the unknown vector and b is a known vector.

In the case of the non-linear Poisson equation A is the discretisation coefficient matrix – where each node will have 7 non-zero values in the matrix, x is the unknown potential vector and b is the charge density whose values are the right hand side of equation (3.14) for each node. As the charge density is dependent on the potential, the equation must be linearised using the Newton Raphson method.

While the discretisation of the left hand side of equation (3.14) can continue as shown in section 3.2.2, (equations (3.10) and (3.11)), the right hand side of the equation requires further consideration.

$$\int_V (n - p + N_D - N_A)\, dv =$$

$$(n - p + N_D - N_A)\left(\frac{h_x + h_{x+1}}{2} + \frac{h_y + h_{y+1}}{2} + \frac{h_z + h_{z+1}}{2}\right) \tag{3.16}$$

The dimensions of the box refer to Figure 3.6. Combining the left hand side from equation (3.11) and the result of equation (3.16) gives the full equation;

$$\begin{aligned}
&\frac{\left(\varepsilon_{(x-1,y,z)}\psi_{(x-1,y,z)} - 2\varepsilon_{(x,y,z)}\psi_{(x,y,z)} + \varepsilon_{(x+1,y,z)}\psi_{(x+1,y,z)}\right)}{hx} hyhz \\
&+ \frac{\left(\varepsilon_{(x,y-1,z)}\psi_{(x,y-1,z)} - 2\varepsilon_{(x,y,z)}\psi_{(x,y,z)} + \varepsilon_{(x,y+1,z)}\psi_{(x,y+1,z)}\right)}{hy} hxhz \\
&+ \frac{\left(\varepsilon_{(x,y,z-1)}\psi_{(x,y,z-1)} - 2\varepsilon_{(x,y,z)}\psi_{(x,y,z)} + \varepsilon_{(x,y,z+1)}\psi_{(x,y,z+1)}\right)}{hz} hxhy =
\end{aligned} \tag{3.17}$$

$$(n - p + N_D - N_A)\left(\frac{h_x + h_{x+1}}{2} + \frac{h_y + h_{y+1}}{2} + \frac{h_z + h_{z+1}}{2}\right)$$

The n and p terms on the right hand side of this equation are dependent on the potential and as a result this equation remains non-linear and must be converted to the form;

$$A\varphi_n = A\varphi_{n-1} + J(\varphi_n - \varphi_{n-1}) \tag{3.18}$$

Where A is the discretisation matrix, J is the Jacobian matrix and φ_n and $\varphi_{n-1}$are the values of the potential at the current and previous iterations respectively. The Jacobian matrix allows the removal of the non-linear term by taking into consideration the charge density at the node. The charge density must be repeatedly calculated over the same volume as the potential. It is assumed that the concentration is constant throughout the volume of the Gaussian box, and can be calculated by multiplying the charge density by the volume of the box.

Equations (3.19) and (3.20) are evaluated over the volume of each node and the values of the fixed charge density in each part of the grid is known.

$$n = n_i e^{\frac{q(\varphi - \phi_n)}{k_B T}} \tag{3.19}$$

$$p = n_i e^{\frac{q(\phi_p - \varphi)}{k_B T}} \tag{3.20}$$

As with the Brownian section, the equation is discretised using a finite difference method. The charge values are re-calculated before each iteration of the solver, as is the Jacobian matrix giving the charge density at each node. As a the potential and the charge density directly affect each other, the exit criteria will only be satisfied when a consistent solution is reached. The method of solving the equations will be discussed in section 3.4.

3.3.3 Current Continuity

The next stage in performing drift diffusion simulations involves describing the charge transport via the current continuity equations, which describe the charge conservation in the simulation domain. The current continuity equations are shown in equations (3.21) and (3.22) for electrons and holes respectively;

$$\nabla \cdot J_n = qR \tag{3.21}$$

$$\nabla \cdot J_p = qR \tag{3.22}$$

Where R is the average net recombination rate. In the simulations used for this thesis, current continuity is only solved for electrons, not for holes. This is due to the negligible contribution of the holes to the current in n channel devices (around 18 orders of magnitude lower in modern devices) which are used throughout this research.

Using the box integration approach illustrated in Figure 3.6 for the Poisson equation, it is possible to discretise the current continuity equation by integrating equation (3.21) over a volume to obtain

$$\int_V \nabla J_n \, dv = q \int_V R \, dv \tag{3.23}$$

which, for a closed piecewise surface, s, can be rewritten as

$$\int_S J_n n \, ds = q \int_V R \, dv \tag{3.24}$$

In this research, however, the effect of holes is neglected as it is assumed to be negligible in comparison to the electron contribution. This means that the recombination rate must tend towards zero and the total flux of electrons over the surface integral must be equal to zero as the recombination rate is the right hand side of equation 3.24 and consequently is rewritten as

$$\int_S J_n n \, ds = 0 \tag{3.25}$$

As a result, the contribution from each surface must be calculated and summed in a similar fashion to that for the potential. The expression for the current density in the drift-diffusion approximation is:

$$J_n = -qn\mu_n \nabla\psi + qD_n \nabla n \tag{3.26}$$

where μ_n is the electron mobility, and D_n is the electron diffusion coefficient. This equation accounts for the drift and diffusion of carriers. As in the discretisation of the Poisson equation, it is assumed that the potential varies linearly between nodes and so can be calculated by taking the mean of the two values. The carrier concentration, however, has an exponential dependence on the potential.

To overcome this problem, an approximation for the current between two nodes derived by Scharfetter and Gummel in their seminal paper [111] has been adopted. In this approximation, the current flow between nodes a and b is given by;

$$J_{n_{ab}} = \frac{qD_{n_{ab}}}{h_{ab}} \left[B\left(\frac{\psi_a - \psi_b}{\frac{kT}{q}} \right) n_a - B\left(\frac{\psi_b - \psi_a}{\frac{kT}{q}} \right) n_2 \right] \tag{3.27}$$

In equation (3.27) the function $B(x)$ is the Bernoulli function and is defined as

$$B(x) = \frac{x}{e^x - 1} \tag{3.28}$$

In this simulator, the Bernoulli function is not evaluated directly as it may cause instability when the value of *x* tends towards zero. Instead, an approximation is made which will ensure relative accuracy, but maintain computational stability. These values are dependent on the floating point precision of the computer but allow for all values of x.

Finally, equation (3.21) can be shown in the discrete form which must be solved iteratively for each node in the simulation domain.

$$D_{n_{x+1/2,y,z}} \cdot \left[B\left(\frac{\psi_{x,y,z}-\psi_{x+1,y,z}}{kT/q}\right) n_{x,y,z} - B\left(\frac{\psi_{x+1,y,z}-\psi_{x,y,z}}{kT/q}\right) n_{x+1,y,z} \right] \cdot \frac{A_{yz}}{h_x} +$$

$$D_{n_{x-1/2,y,z}} \cdot \left[B\left(\frac{\psi_{x,y,z}-\psi_{x-1,y,z}}{kT/q}\right) n_{x,y,z} - B\left(\frac{\psi_{x-1,y,z}-\psi_{x,y,z}}{kT/q}\right) n_{x-1,y,z} \right] \cdot \frac{A_{yz}}{h_{x-1}} +$$

$$D_{n_{x,y+1/2,z}} \cdot \left[B\left(\frac{\psi_{x,y,z}-\psi_{x,y+1,z}}{kT/q}\right) n_{x,y,z} - B\left(\frac{\psi_{x,y+1,z}-\psi_{x,y,z}}{kT/q}\right) n_{x,y+1,z} \right] \cdot \frac{A_{xz}}{h_y} +$$

$$D_{n_{x,y-1/2,z}} \cdot \left[B\left(\frac{\psi_{x,y,z}-\psi_{x,y-1,z}}{kT/q}\right) n_{x,y,z} - B\left(\frac{\psi_{x,y-1,z}-\psi_{x,y,z}}{kT/q}\right) n_{x,y-1,z} \right] \cdot \frac{A_{xz}}{h_{y-1}} +$$

$$D_{n_{x,y,z+1/2}} \cdot \left[B\left(\frac{\psi_{x,y,z}-\psi_{x,y,z+1}}{kT/q}\right) n_{x,y,z} - B\left(\frac{\psi_{x,y,z+1}-\psi_{x,y,z}}{kT/q}\right) n_{x,y,z+1} \right] \cdot \frac{A_{xy}}{h_z} + \quad (3.29)$$

$$D_{n_{x,y,z-1/2}} \cdot \left[B\left(\frac{\psi_{x,y,z}-\psi_{x,y,z-1}}{kT/q}\right) n_{x,y,z} - B\left(\frac{\psi_{x,y,z-1}-\psi_{x,y,z}}{kT/q}\right) n_{x,y,z-1} \right] \cdot \frac{A_{xy}}{h_{z-1}} +$$

$$= qR\left(\frac{h_x + h_{x-1}}{2} \cdot \frac{h_y + h_{y-1}}{2} \cdot \frac{h_z + h_{z-1}}{2}\right)$$

Where A_{yz}, A_{xz} and A_{xy} are the areas of the respective sides of the box surrounding the node.

3.4 Linear Solvers

This section describes the methods used in this research to solve the linear sets of equations obtained from the described discretisation of the Poisson and the current continuity equations. Initially there is a general discussion of the iterative solvers, followed by two specific methods, each of which is used in the simulations in this thesis.

3.4.1 Iterative Solvers

Iterative solvers repeatedly approximate the solution to a linear algebraic system of equations until a pre-set tolerance is reached. The iterative solvers have the advantage over their direct counterparts in that, since the matrices are sparse, it is only necessary to store the diagonals, allowing the reduction of the data storage required. In many cases, without these methods, it would not be practical to solve equations over large, fine meshes which could easily require several matrices of tens or hundreds of Gigabytes. They may, however, require many iterations to reach a solution, and may even diverge from the solution in some cases.

When solving an equation over a large mesh, the direct solution will quickly become cumbersome. Taking equation (3.15), if the Poisson equation is to be solved for a mesh with dimensions $100 \times 200 \times 10$ as required in this research, the matrix A will have the dimensions 200000×200000 meaning that 4×10^{10} 8 byte values must be stored. This will require approximately 300 Gb of storage. However, as shown in Figure 3.8, the matrix is sparse, with only seven diagonals containing values, and it is possible to simply store these 7 values for each node. Direct solvers would require the use of the whole matrix at once, but instead

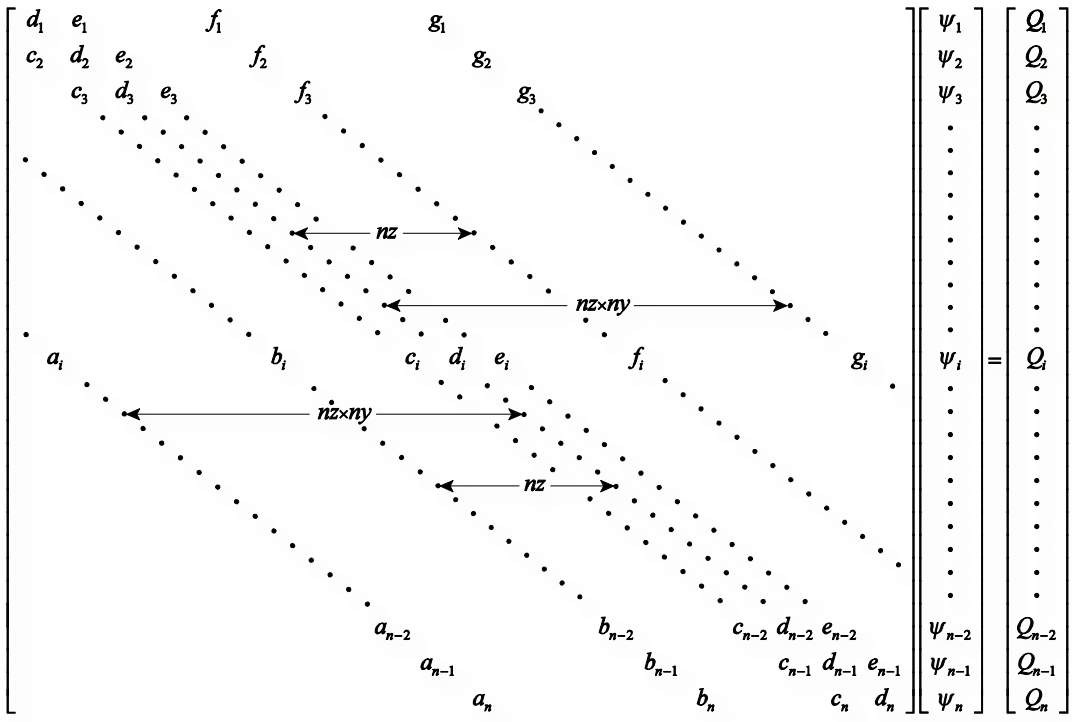

Figure 3.8 – Full equation matrix showing that all values not in the 7 diagonals are zero. The size of the matrix depends on the dimensions of the mesh. After A. Brown [112].

iterative solvers allow us to keep the structure of the matrix without the huge memory requirement. This makes finer meshes computationally realistic allowing more detailed simulations of smaller structures.

The structure of the matrices defined in the discretisation system of equations is determined by the discretisation mesh as described in more detail in section 3.2.2. Contributions from the surrounding nodes must be included when calculating a given node. The number of neighbouring nodes taken into consideration depends on the simulation technique being used, but in the box discretisation adopted in this research, only the nearest neighbours in each dimension were used according

to equation (3.11). The contribution of each node is added to the matrix 'coefficients' which means that the complex calculations can be separated from the more simple calculations of the effect of a specific node. In some iterative schemes and for some equations, these coefficients must be calculated before each iteration of the solver. This requires a significant computational overhead. In this research, the coefficients are calculated once for the Poisson equation, but are calculated before every solution to the current continuity equations.

A 3D example of the coefficients assembly is shown in Figure 3.6. The example shows a uniform mesh spacing. By taking the distance between mesh nodes into consideration when calculating the coefficients, it is possible to account for a non-uniform mesh.

The solution is repeatedly executed in order to make the value of r in equation (3.30), where r is the residual, b is a known value, x is the solution, and A is a matrix of the coefficients, as small as possible. This is where. The value of the matrix x will be changed in order to reduce the size of r until r becomes smaller than the pre-set error tolerance.

$$r = b - Ax \tag{3.30}$$

The simulator used in this research makes use of two iterative solvers, a successive over-relaxation solver (SOR) and a bi-conjugate graduate stabilised solver (BiCGSTAB). Both of these processes use repeated estimates of a solution, with gradual changes, in order to reach a final solution within a predetermined error level. While an in depth investigation of these methods is beyond the scope

of this document, the following two sections briefly describe each of these systems, and indicate particular points of importance to this research.

3.4.2 SOR

Successive over relaxation is a stationary mesh relaxation method. Instead of the traditional relaxation, where the ‘guess’ of the solution is altered by the residual, the guess; is altered by the residual multiplied by a number between 1 and 2. This scheme significantly increases the speed at which high order errors are eradicated, over traditional relaxation methods, but can become problematic as it nears the final solution, since the multiplication factor may force the method to repeatedly overshoot the final solution [3]. SOR was chosen as it allows the relatively simple implantation of the charge calculation within the iterative solver. While there are more efficient methods available, SOR was chosen as a trade-off between reasonable efficiency combined with rapid development.

This method is more computationally stable than the biconjugate gradient method (BiCG), and has the benefit that it is easier to implement non-linear equations, but it is less efficient [113]. The practical efficiency of the solution can be improved by employing the red black Gauss Siedel method of iteration, which will allow parallelisation of the calculations since no adjacent nodes will be changed simultaneously. This has benefits on almost all modern computing platforms, red-black Gauss Siedel solves alternate nodes of the solution in the fashion shown in Figure 3.9.

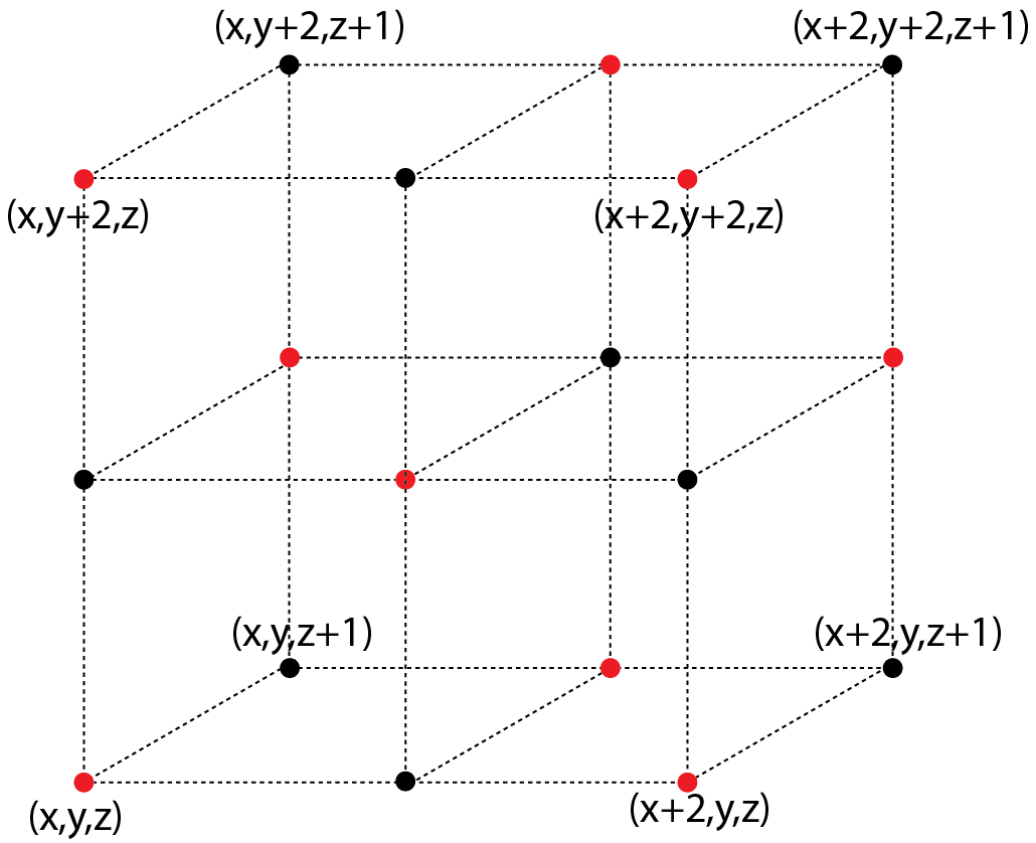

Figure 3.9 - Example showing red black Gauss Siedel methodology. No red node is adjacent to any other red node, meaning that the solution can be parallelised without causing inconsistencies in numbers being used. The update of the red nodes only depends on the black nodes, with the opposite also being true.

The SOR iterations proceed as follows; once the coefficients have been calculated with the charge contribution included, the solution to the Poisson equation can be calculated as follows:

$$a\psi_{(x-1,y,z)} + b\psi_{(x,y-1,z)} + c\psi_{(x,y,z-1)} + d\psi_{(x,y,z)} + e\psi_{(x,y,z+1)} + f\psi_{(x,y+1,z)} + g\psi_{(x+1,y,z)} = Q \quad (3.31)$$

$$\psi'_{(x,y,z)} = (a\psi_{(x-1,y,z)} + b\psi_{(x,y-1,z)} + c\psi_{(x,y,z-1)} + e\psi_{(x,y,z+1)} + f\psi_{(x,y+1,z)} + g\psi_{(x+1,y,z)})/d \quad (3.32)$$

$$\psi'_{(x,y,z)} = \psi_{(x,y,z)} + \omega\left(\psi'_{(x,y,z)} - \psi_{(x,y,z)}\right) \quad (3.33)$$

$$where\ 0 < \omega < 2$$

In equations (3.31) to (3.33), a-g are the coefficients of the nodes including the charge contribution, $\psi_{(x,y,z)}$ is the initial potential at node (x, y, z), $\psi'_{(x,y,z)}$ is the potential at node (x, y, z) after the calculation and ω is the over relaxation coefficient which is chosen to be between 0 and 2 to converge on the solution more quickly. Strictly speaking, if the value of ω is less than 1, the process is called successive under relaxation, and in this research the value is always chosen

between 1 and 2. As shown in equation (3.31), the difference between the current solution and the updated solution is multiplied by ω, meaning that the change in approximation of the potential is greater than in a traditional relaxation method.

3.4.3 BiCGSTAB

Biconjugate gradient stabilised method is an iterative method which aims to reduce the residual of an estimation and thereby reach a solution to a linear, or linearised equation [114]. While SOR is a stationary method (the information that the solution depends on does not change after each iteration), BiCGSTAB is a non-stationary method, where after each iteration one or more of the variables on which the final solution depends changes. This is more difficult to implement, but is in general more effective than a stationary counterpart [113]. This is particularly difficult to implement for non-linear equations, and as a result it was decided that this method should not be used for the solution to the non-linear Poisson equation.

BiCGSTAB is an evolution of the conjugate gradient and bi-conjugate gradient methods in turn. By working to reduce the residual of equation (3.30), the system converges on the final solution to the linearised equation. While this may take many iterations, only the vectors associated with the previous attempt need to be stored in order to reduce the solution further. The system uses the value of the residual, and the previous residual to decide the ‘search’ direction for the next iteration. As with most iterative methods, the solution will continue until a pre-set

number of iterations unless it satisfies an exit criterion, such as the residual falls below a pre-defined minimum.

In this research, the BiCGSTAB scheme is used in two separate instances. Firstly, it is used to solve the current continuity equation for electrons in the drift diffusion sections of simulations. This is because the current continuity equation is non-stationary and as a result requires a non-stationary iterative method. If a point iteration method such as SOR were used, in some instances, the iterative solution to the current continuity equation could diverge since the matrix will not be diagonally dominant due to the Bernoulli functions which determine the value of the current continuity matrix. Instead, current continuity requires a direct or conjugate method. Secondly, since it is simpler to implement for linear equations than for non-linear equations, it is used for solving the linear Poisson equation in the Brownian regions of simulations where drift diffusion is not solved over the whole domain after each iteration.

3.5 Conclusion

The numerical techniques used to develop the integrated ion-channel-transistor were discussed – in particular the integration of particle and continuous simulation techniques. The importance of both Brownian dynamics and drift diffusion simulation methodologies was shown, with particular reference to the particular attributes which are required for different sections of this research. Brownian dynamics enables the investigation of the transport of individual charge carriers while benefitting from computation efficiency elsewhere in the simulator.

The combination of these methods allows the simulation of a bio-interface including nano-scale pores and field effect semiconductor devices.

Additionally, the solvers used in this research were briefly described. By highlighting the important attributes which make them desirable for particular equations it was shown that SOR was appropriate for the non-linear Poisson equation due to the relative simplicity of implementation, while BiCGSTAB was chosen for current continuity as it requires a conjugate gradient method in order to converge.

Chapter 4

Software Development

4.1 Introduction

This chapter describes the practical development of the integrated Brownian dynamics and drift diffusion dual simulator. Drift diffusion simulation was integrated into a pre-existing Brownian dynamics simulator. However the significant differences between the two simulation approaches meant that this task was non trivial in nature, and the bulk of this chapter describes the staging of the work and the strict testing regime employed at each stage of code development to ensure consistency with previous simulations and analytic results. In addition, the strategy to achieve self-consistency between the two types of simulation in a heterogeneous simulation domain are discussed, with final results showing a stable coupling of the two simulation methodologies – one of the most significant achievements of this body of work.

4.2 Development and Testing

The step-by-step development of the simulator is documented in this section. The development involved rigorously testing the simulator after every significant addition. This involved comparison with working examples of a separate drift diffusion simulator and analytical results of resistors, diodes and both analytical and real MOSFETS. Starting with a working Brownian dynamics codebase, elements of a drift diffusion methodology were added.

Initially a non-linear Poisson solver was implemented within the Brownian framework, as described in section 1. This was extended to include a self-consistent Poisson and current continuity solver, detailed in section 4.4.2. A system of 'flags' was then developed in order to fully solve a drift diffusion simulation within a larger domain which includes Brownian 'regions.' These flags were integer variables assigned to each node denoting which type of region the node lay in. Before attempting a combined solution, the ability to create a more complex structure was developed as discussed in section 4.5. As the original codebase had not been designed for FET structures, and the various shapes and materials required, including Gaussian distributions, these systems had to be developed and tested. Finally, as shown in section 4.5.6, an ionic solution was introduced and a fully integrated combined drift diffusion and Brownian dynamics simulation was performed.

4.3 Implementation Challenges

As both the drift diffusion, and Brownian dynamics code bases have been in development for many years, it was a complex task to plan and execute this simultaneous implementation in a single simulation domain. It was decided to adapt and add the DD capabilities into the structure of the existing Brownian code – this meant aligning it to the existing arrays, structure and domains and ensuring that applicable solvers were available. Considerable time was spent ensuring that the new drift diffusion implementation fitted into the existing structure of the Brownian code, especially the input structure system and material identifiers.

There were two stages in the development of the software in this PhD project. Initially, a version of a pre-existing drift diffusion code had to be translated and implemented within the structure of the Brownian dynamics code. It is essential that the two methods are implemented in the same code base in order to simplify the second stage, the creation of a dual simulation domain. This development required strict and careful testing of the drift diffusion code, which was set up to use as much of the existing structure and definitions of the Brownian code as possible in order to minimise the chance of creating errors in older sections.

Since drift diffusion is a continuum method, the expected output potential is smooth and linear while Brownian dynamics is a particle method containing discrete charges, meaning the time averaged potential output is expected to tend towards those from DD. The difficulty in aligning these two code bases can be demonstrated by comparing a simple resistor simulation using each method, for this purpose, identical resistors were simulated using each simulation methodology. A basic resistor was chosen of size $20 \times 18 \times 18$ nm in the *x*, *y*

and z directions respectively with a substrate of dielectric $\varepsilon_r = 80$ representing water.

While the Brownian simulator is capable of modelling a system with both positive and negative ions, the DD simulator only solves the current continuity equation for negative carriers. For this reason, the resistor was doped with a concentration of $6.0221415 \times 10^{26}\, m^{-3}$ (equivalent to one Molar concentration) of chloride ions, with no positive mobile charge, in the Brownian simulation. In drift diffusion a substrate of water and N type doping emulated these conditions.

The results of these simulations can be seen in Figure 4.1. In the initial work, a C version of the Glasgow 'Atomistic' drift diffusion (DD) simulator [115] was used.

Figure 4.2 shows the results of the simulation for Brownian dynamics and drift diffusion alongside the solution to Ohm's law – equation (4.1).

$$I = n\mu_n qA\frac{E}{L} \tag{4.1}$$

For this simple resistor simulation it can be seen that the DD simulation provides a more accurate solution compared to the Brownian solution. The average calculated error in the Brownian simulation is 3.5% caused by noise, whereas the drift diffusion simulation better matches Ohm's law with an error of 0.011%. These are simple simulations, though, and the advantage of using Brownian

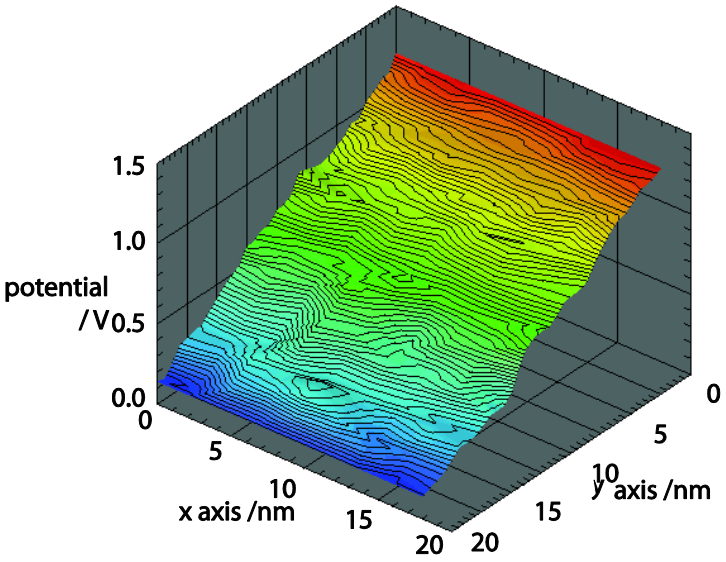

A

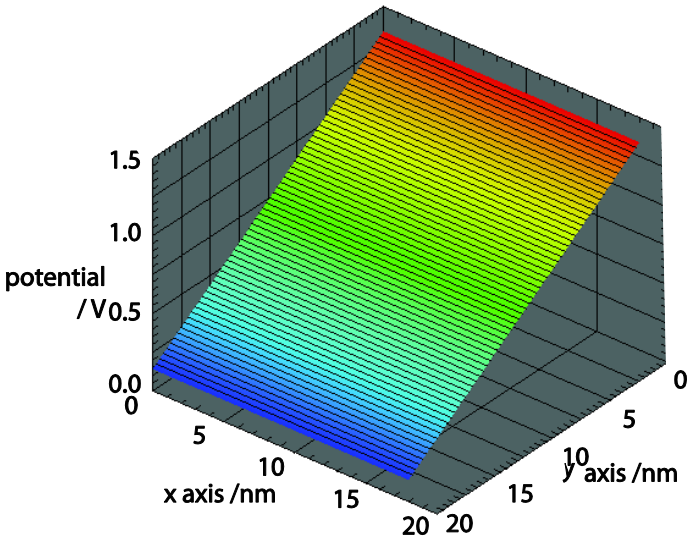

B

Figure 4.1 – 3D potential profile of a resistor, modelled as a 20 × 18 × 18 nm volume of 1M solution of chloride ions in water, simulated using Brownian Dynamics (A) and Drift Diffusion (B). The figure shows a plane in the z axis with a gradient applied to indicate the potential at each point. The lines indicate points of equipotential.

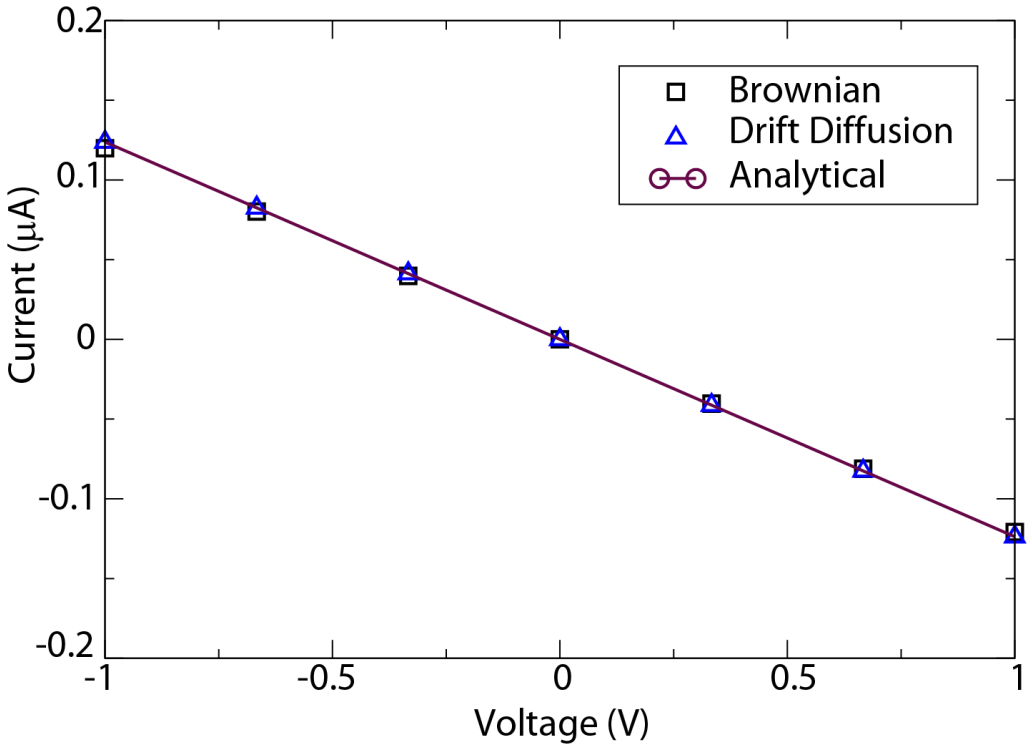

Figure 4.2 – Calculated current against applied voltage for a 20 × 18 × 18 nm volume of 1 M solution of chloride ions in water, obtained from Brownian simulation, Drift Diffusion simulation and analysis assuming a mobility of 7.92×10^{-8} $m^2 s^{-1} V^{-1}$.

dynamics methods is that the effect of discrete ions in a solution can be modelled, resolution which is lost when using a continuum method such as drift diffusion.

4.4 Drift Diffusion Implementation

This section details the practical implementation and testing of the drift diffusion simulator within the framework of the Brownian simulation code. The first part details the development and testing of the code developed to solve the non-linear

Poisson equation. The second part details the implementation of the solution to the electron current continuity equation and demonstrates results for a fully self-consistent drift diffusion simulator. At each stage the practical difficulties of including two distinctive methodologies in a single simulation will be flagged, and solutions to these difficulties will be commented upon.

4.4.1 Solving the Poisson Equation

The implementation of the drift diffusion code within the existing Brownian dynamics code framework began with the development of a 3D solver for the non-linear Poisson equation. As noted above, a working and extensively tested drift diffusion code with 3D solvers was used as a reference for this work, although the C codebase could not be transferred directly to the Brownian code as it was written in a different programming language.

An important part of the implementation of the drift diffusion was that it not only had to work within the Brownian framework, but it was essential for the latter parts of the research that data could be transferred between the two sections of the code. For this reason, the structure of the mesh and arrays of data from the original code were used to implement the new sections of the simulator. The definitions of some sections of the code were altered to accommodate this, but wherever possible variables which were already present were used to hold the data.

The solver in the C based drift diffusion simulator used an indexing system to work through the arrays, and this had to be modified to ensure that, in future tests

where only certain sections of the simulation domain were being modelled by drift diffusion, this did not cause incorrect values to be used.

New material definitions were created, to allow the introduction of silicon, silicon oxide and silicon oxynitride. These were added to the current software system which already allowed various materials to be included in a simulation. Parameters were added to the structure definition to allow intrinsic carrier concentration and mobility values to be attached to each node in the mesh, and finally to allow fixed charge to be stored at each mesh point. As with the previous changes, wherever possible, these changes were made to match the current system to avoid disruption to the working Brownian codebase.

The benchmark chosen at this stage to test the newly created non-linear Poisson solver was a simple NP diode, 1D in nature, but implemented in 3D. This test was purely electrostatic in nature, only involving the non-linear Poisson solver, and its operation with the input/output and support routines from the Brownian code. No Brownian particles were used at this stage. The diode dimensions were $150 \times 150 \times 150$ nm with a mesh of $71 \times 3 \times 3$ nodes. The physical dimensions were chosen in order to make the device significantly wider than the depletion region, while the mesh was chosen to allow for the clear resolution of the depletion region along the axis of interest. The other two dimensions were much coarser as these were used to test the implementation of the indexing systems described above, and data was not required from them. The acceptor concentration on the P side and the donor concentration on the N side are equal and were chosen as $1.0 \times 10^{24}\,\mathrm{m}^{-3}$ and the value of the intrinsic carrier concentration, n_i, set to $1.0 \times 10^{16}\,\mathrm{m}^{-3}$ The value of ε_{si} was selected as 11.9 to model silicon and the device was modelled at 300 K. Dirichlet boundary conditions (where the values at the boundary are fixed) were set up in a plane

across the first nodes and last nodes of the device, no bias was applied. Neumann conditions (where the rate of change of the values is fixed at the boundary) were used at all other boundaries.

The result of simulations carried out using the Brownian code, compared to the original C based Drift Diffusion code are illustrated in Figure 4.4 and Figure 4.5. In the Brownian code, the diode is set up for test three times, in the *x*, *y* and *z* directions to avoid any bugs in the 3D implementation. The solutions in all three cases match at all points to 'machine precision' and converged in the same number of iterations.

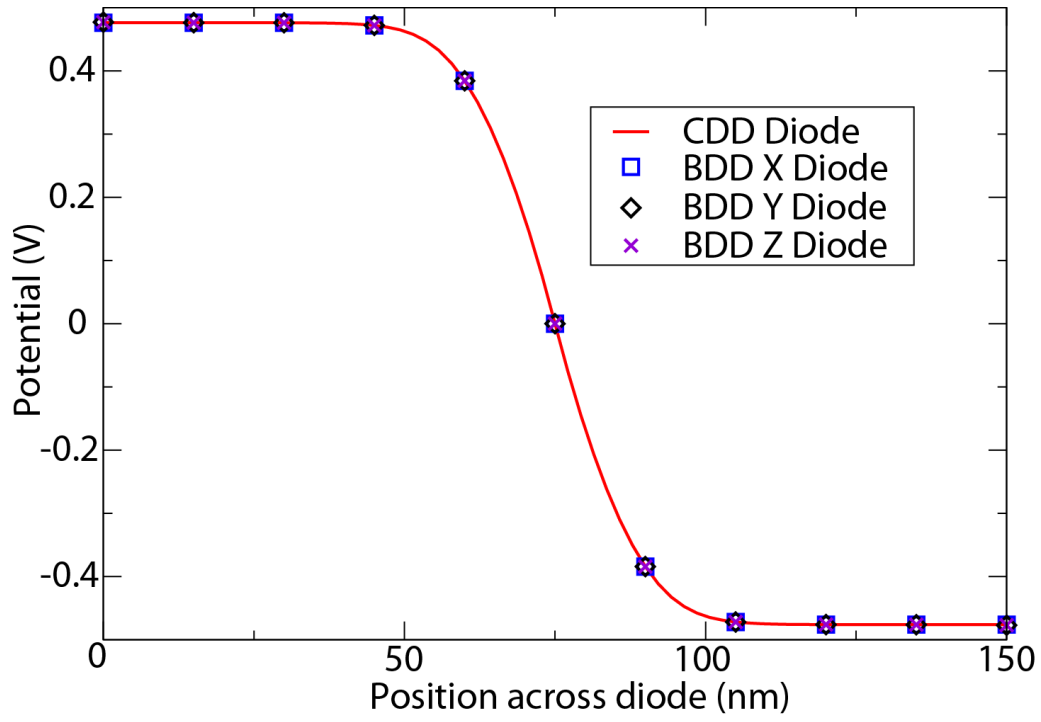

Figure 4.4 - Potential in a diode. The result from the C based version of the code is compared to the Brownian based code. The Brownian based drift diffusion result is shown solved with the diode over each axis, this is to ensure correct software operation for future simulations.

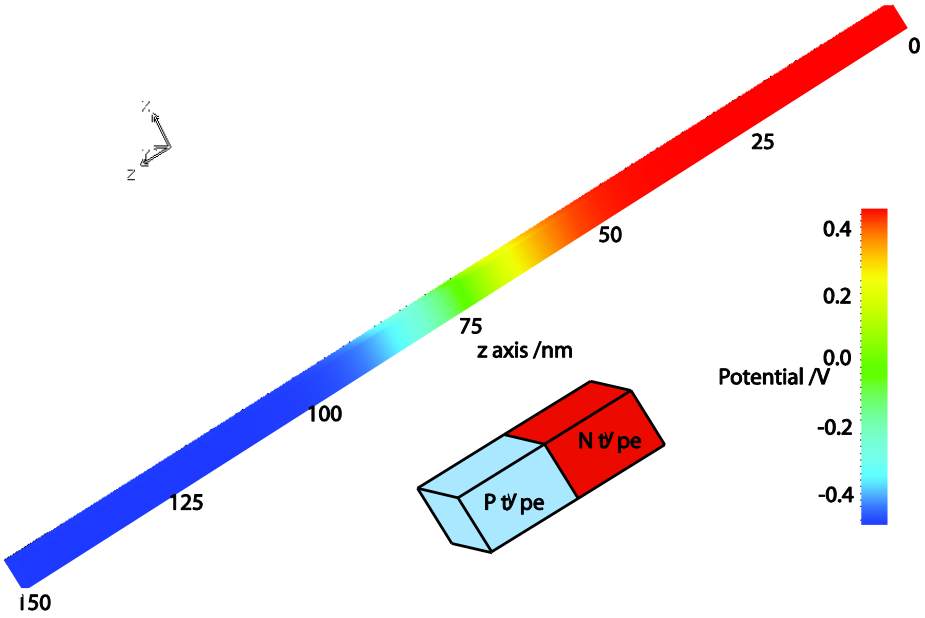

Figure 4.5 – 3D output of the NP diode where the doping concentration varies over the Z axis. This is shown to demonstrate that the potential is correct throughout the device, not only in 2D.

4.4.1.1 Modelling the Depletion Region

With a potential profile matching the previous version of the code, the next test was to ensure the consistency of the depletion region. This test allowed us to compare the simulation to analytical theory with a single number – the depletion layer width – showing the accuracy of the simulator at high and low charge density.

In order to calculate the expected size of the depletion region, an approximation is used [116]. This is based on an abrupt junction where the N and P sides of the depletion region are assumed to have no net charge, while outside of the depletion

region the N and P regions are electroneutral. This is, of course, not the case in real devices as there is a transitional region and the edges of the depletion region are not perfectly abrupt. This means that the electric field in the simulation will not have a linear dependence inside the depletion region showing gradual gradient change towards the electroneutral bulk regions where no net electric field is present.

Using the approximation, a value of 56.7 nm was calculated for the previously described diode structure. Using the plots of the electric field the simulated depletion region is approximated to the linear section of the electric field which is an approximation valid for all but large applied biases. When the region approximated in this way, Figure 4.6 this gives a value of 55 nm which is in close agreement with the expected value.

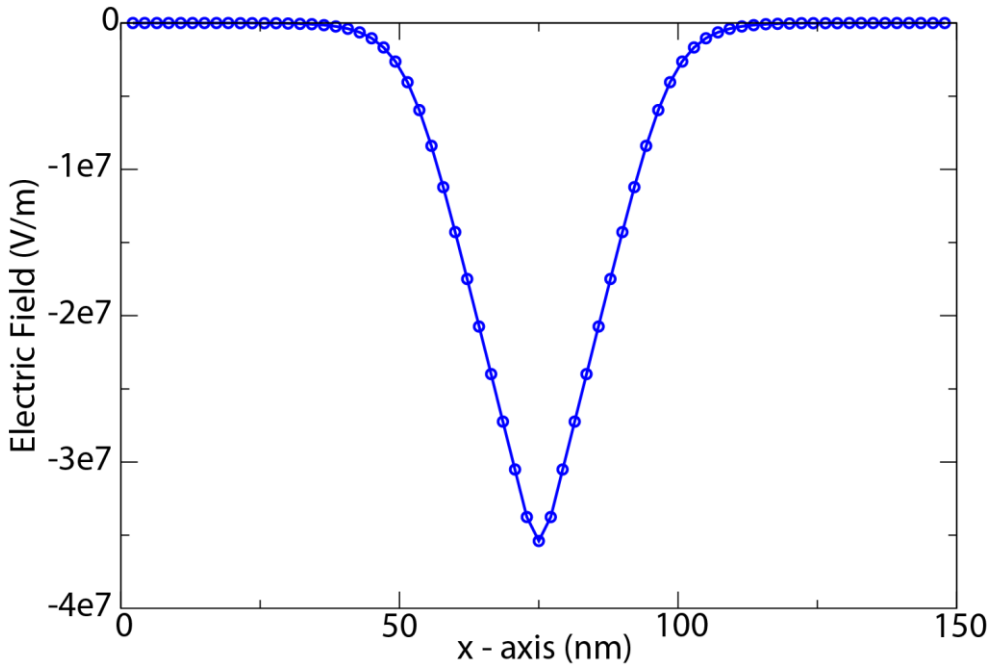

Figure 4.6 – Electric field of an NP diode 150 nm long, doped with a concentration of $1.0 \times 10^{24}\ m^{-3}$ donors and acceptors in the N (0 to 75 nm) and P (75 to 150 nm) regions respectively.

To ensure that the code operates correctly with a variety of input structures, an alternative diode was simulated. This diode was an asymmetric PN type, with a P type doping concentration of $1.0 \times 10^{24}\,\mathrm{m}^{-3}$ as before but a $2.0 \times 10^{24}\,\mathrm{m}^{-3}$ concentration of N doping. This was simulated in a $300 \times 200 \times 200$ nm device, chosen to be significantly larger than the maximum expected depletion region to ensure that the depletion region would not be affected by the Dirichlet boundaries which were unbiased. The transverse directions were chosen to separate any effects of boundary conditions from the depletion region. The grid size of $71 \times 21 \times 21$ was chosen to ensure detail in the depletion region because of the sub 5 nm spacing in *x*, while also avoiding any effects of the Neumann boundaries at all other edges in the simulation.

The depletion region was calculated to be 43.0 nm and was measured to be 44 nm when approximating the depletion region to the linear section of the electric field. Figure 4.7 shows a 2D potential profile through the device, with the 3D profile

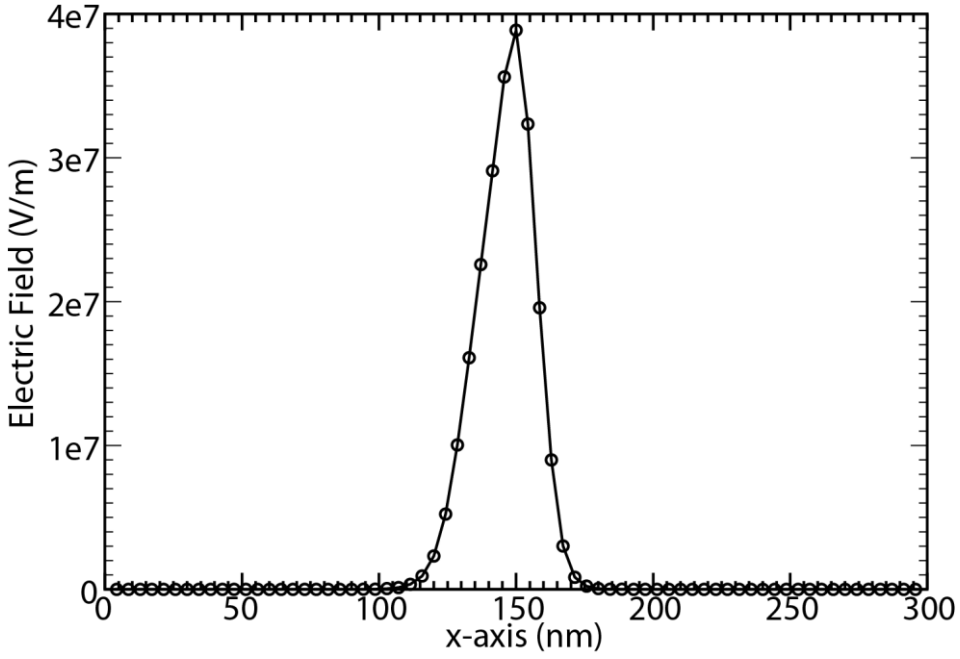

Figure 4.7 – Electric field of an unbiased PN diode with $1.0 \times 10^{24}\,\mathrm{m}^{-3}$ acceptors on the P side which is between 0 and 150 nm and $2.0 \times 10^{24}\,\mathrm{m}^{-3}$ concentration of donors on the N side which is the remainder of the device.

showing the potential throughout the device shown in Figure 4.8.

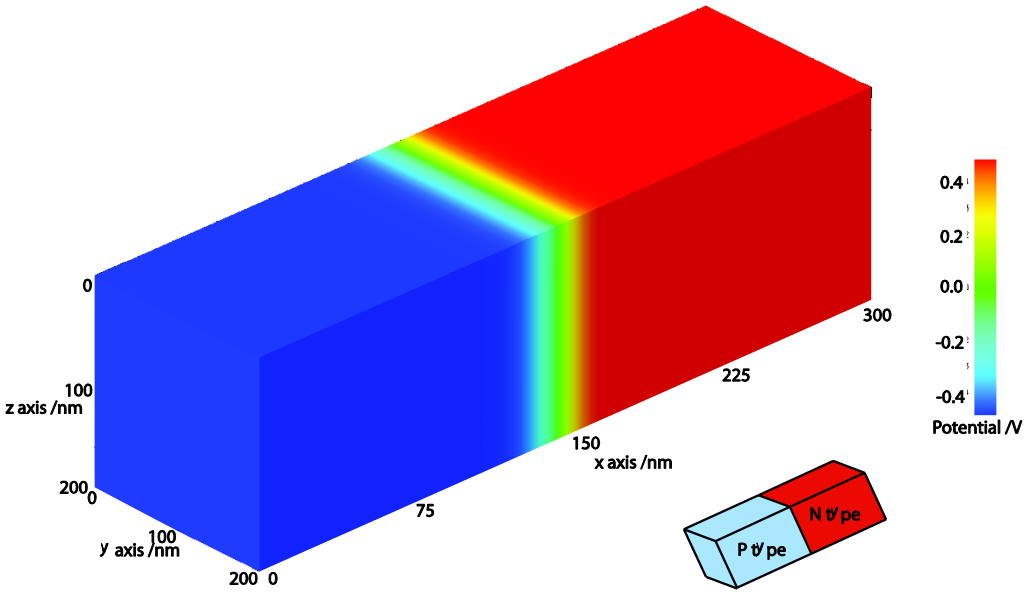

Figure 4.8 – 3D version of the PN diode. The depletion region stretches further into the P type region due to the higher level of N type doping. The solution is correct throughout the domain. All dimensions are in nm.

4.4.1.2 Adding Bias

The final stage of testing the implementation of the non-linear Poisson solver was to ensure correct simulation of the diode under bias conditions. For this test, a 200 nm cube was chosen as, though tests are presented here for the x direction, simulations were performed in all three spatial directions , and the structure was held the same for all tests. The grid size of $101 \times 3 \times 3$ was chosen to ensure good resolution (2 nm) in the x dimension, while the transverse dimensions were simulated with a small number of nodes as this was essentially a 2D test. Dirichlet

boundary conditions were set up at 0 nm and 200 nm in the *x* dimension. All other boundaries used Neumann conditions.

The doping concentration on both sides of the metallurgical junction was $1.0 \times 10^{24}\,\mathrm{m}^{-3}$ to represent a heavily doped semiconductor. The intrinsic carrier concentration was set to $1.0 \times 10^{16}\,\mathrm{m}^{-3}$ and the value of ε_{si} chosen as 11.9. Figure 4.9 shows the potential distribution along the *x* axis through the centre of the device for multiple biases which were applied to a Dirichlet boundary at 0 nm. Table 4.1 shows the expected depletion region widths, and those measured

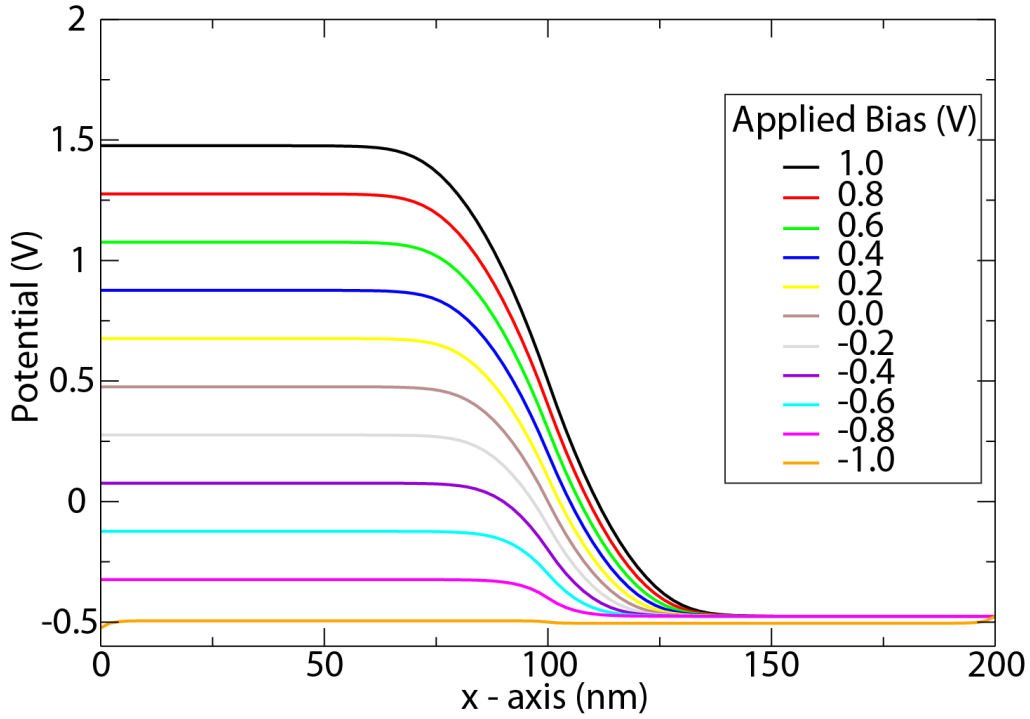

Figure 4.9 – NP diode with multiple bias conditions on the first contact. The depletion region rises in proportion to the square root of the applied voltage.

approximately from the graphs.

Applied Bias on Contact 1(V)	Expected Depletion (nm)	Approximate Measured depletion (nm)
-0.8	20.0	24
-0.4	38.1	36
0.0	50.1	48
0.4	59.7	56
0.8	67.9	64

Table 4.1 - Expected and measured depletion regions for various biases. The measured depletion regions are approximate since it is difficult to read them exactly from the graph.

4.4.2 Self-Consistent Drift Diffusion Solver

Having tested and verified the non-linear Poisson solver, the next stage is to develop and test code to solve the current continuity equation. Once again, changes were made to the definition of the mesh to include storage arrays for all required variables.

As the code design was object oriented, much of the development related to the Poisson solver could be used to create the necessary framework for the current continuity. However, the solution of the current continuity equation necessitates the use of the BiCGstab solver. The corresponding code was translated from the previous C version, and several basic tests were carried out in order to ensure that the discretisation coefficients were calculated correctly, including comparison after single iterations to the Atomistic code. Current calculations based on the flux

of charge were also matched to the previous code. Additionally, all previous tests were completed and compared regularly to ensure that changes made to the codebase had not caused errors in previously working sections.

To fully test the current continuity and in order to test the coupling of the Poisson and the current continuity equations, a resistor with size $200 \times 200 \times 200$ nm was created with an N type doping concentration of $1.0 \times 10^{24}\,\mathrm{m}^{-3}$. The mesh size was chosen as $21 \times 5 \times 5$ for the *x* orientation test of the resistor. The mesh is altered to give finer detail to the axis of interest in both the *y* and *z* cases. The mesh size of 5 in *y* and *z* allowed for two mesh points to ensure that the Neumann boundaries were implemented correctly for what is essentially a 1D problem. 21 was chosen for the dimension of interest to allow for fault finding in boundary conditions and a reasonable resolution of the 1D problem.

Figure 4.10 shows the results of the simulation of the resistor structure compared to the solution of Ohm's Law. A resistor oriented in any of the three dimensions was simulated correctly. Figure 4.11 shows the resistor with the bias conditions reversed in order to test the implementation of the discretisation of the current continuity equation. It is compared to Ohm's law achieving good agreement.

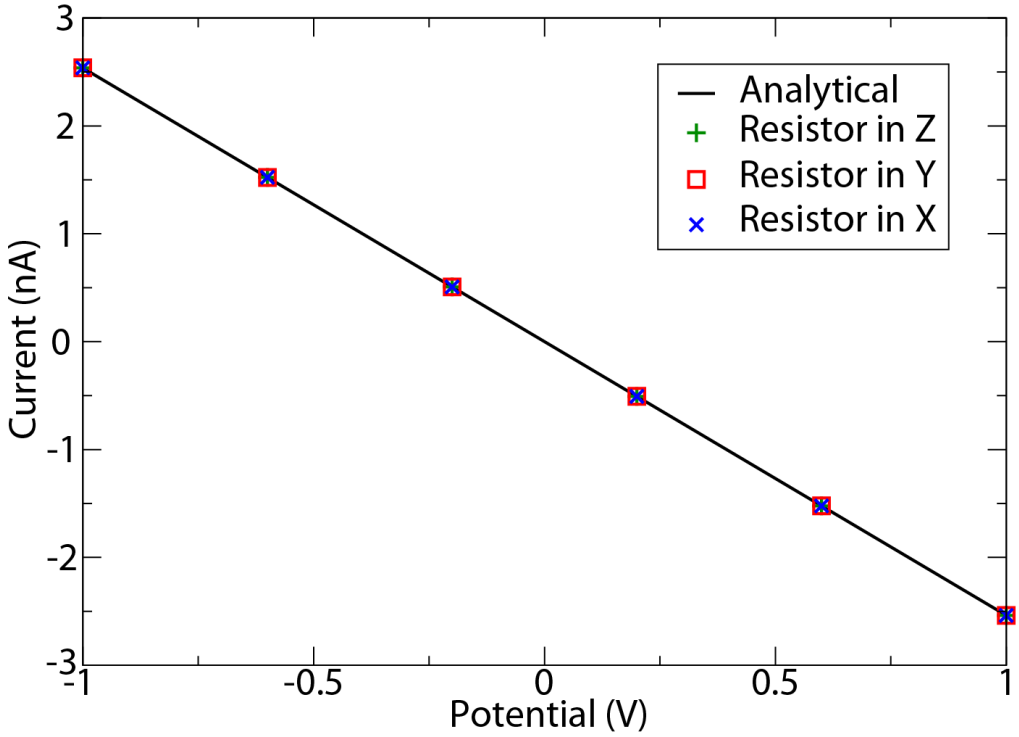

Figure 4.10 – Current Voltage characteristics of a resistor. The analytical solution is shown alongside the solutions in three dimensions from the Brownian based Drift Diffusion simulator.

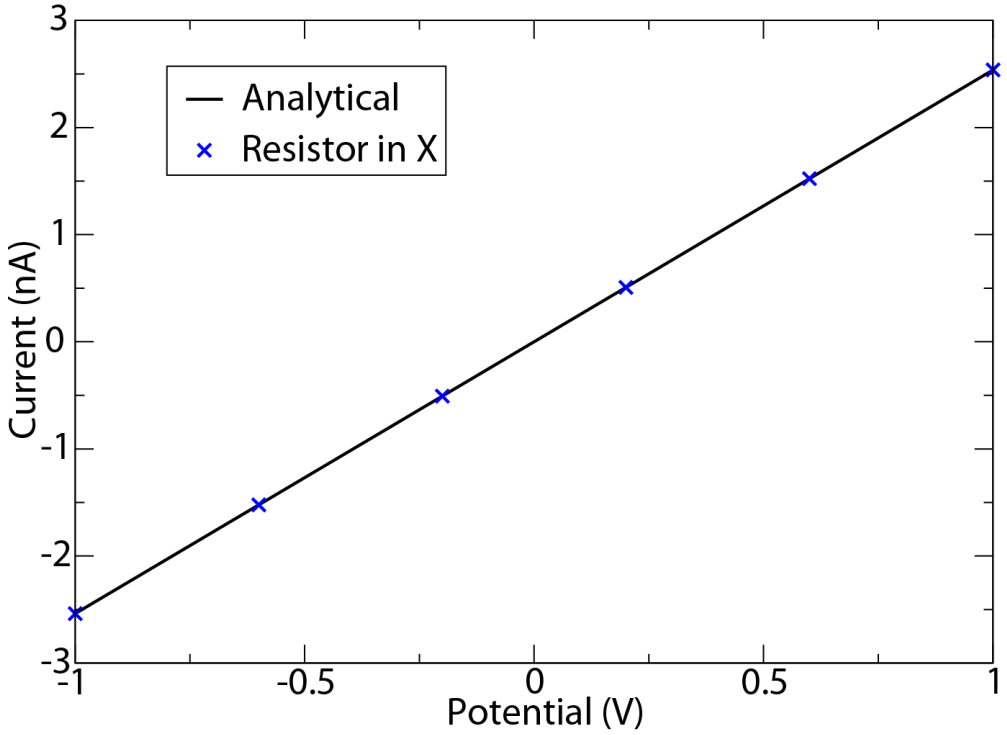

Figure 4.11 – Current voltage characteristics of a resistor which has reversed conditions. This test ensures the directionality of the nodal contributions is correct.

The results of the self-consistent solution of the nonlinear Poisson equation and current continuity equation agree with the analytical results for these structures to machine precision. In summary, drift diffusion simulation has been integrated into an existing Brownian dynamics code harness and successfully tested independently of the Brownian simulation itself.

4.5 Integrating the Simulators

The integration of the two simulation methods was designed to use as much of the current structure generating code as possible, obviating the need to redefine many material model parameters. The mesh and material description were shared between the two simulation techniques but, in order to make the iterative solutions simpler to implement, the areas storing the potential and the charge density at each point were duplicated for use in each separate simulation method, with systems to transfer updates between the two arrays. Additional flags were also added allowing the code to discriminate between regions of the simulation domain indicating which simulation technique should be used in a specified volume. (Note that the current structure only allows for a single cuboidal volume for each simulation technique, a limitation which does not constrain the research reported in this thesis, and is surmountable through some increase complexity in future work.)

There are two critical areas where the behaviour of the code differs between the simulation techniques, firstly the contact definition and secondly the region definition. It is beneficial for the sections of the contacts and regions to be flagged as one of three types – “BD” “DD” or “DUAL.” A Brownian contact (BD) allowed particles to be created and removed from the simulation depending on their trajectory, and holds a constant potential. The DD contact also holds a constant potential, but does not allow mobile charges to be added or removed, since in this region, no individual particles are present.

The “DUAL” contacts and regions are used for the crossover boundaries between drift diffusion and Brownian domains, where the potentials and charge densities

must be solved in the two domains self consistently. These sections hold the potential constant for the duration of the solution to that individual simulation methodology. The contact is essentially reset before each full iteration of a solver to ensure that the solutions to each simulation domain are consistent.

4.5.1 Drift Diffusion Simulations Using the New Structure

In order to ensure that the partitioning of the simulation domain has been correctly implemented tests have been performed on a simple resistor structure where Drift Diffusion is solved in only a portion of the simulation domain and the rest of the domain defined as 'Brownian' remains unsolved, or 'dormant'. The dimensions of the entire structure remain at $200 \times 200 \times 200$ nm with $21 \times 3 \times 3$ nodes in the *x*, *y* and *z* directions respectively. The semiconductor was N type doped with a concentration of $1.0 \times 10^{24}\,\mathrm{m}^{-3}$. The electron mobility is $7.92 \times 10^{-8}\,\mathrm{m}^{2}\mathrm{s}^{-1}\mathrm{V}^{-1}$.

The simulation domain was divided into two sections, initially in half with the region from $x = 0$ to $x \leq 100$ nm solved using drift diffusion and the area from $x > 0$ to $x = 200$ nm as a 'dormant' Brownian region, with boundary potentials between the drift diffusion and Brownian regions fixed to the value expected from the solution of the drift diffusion over the whole simulation domain. As the Brownian simulation code was not being tested, no solution was performed in this region. The solution is shown in Figure 4.12 alongside a drift diffusion solution carried out over the whole domain for comparison. While this is essentially a 1D problem, it is important for test purposes that the solution works throughout the

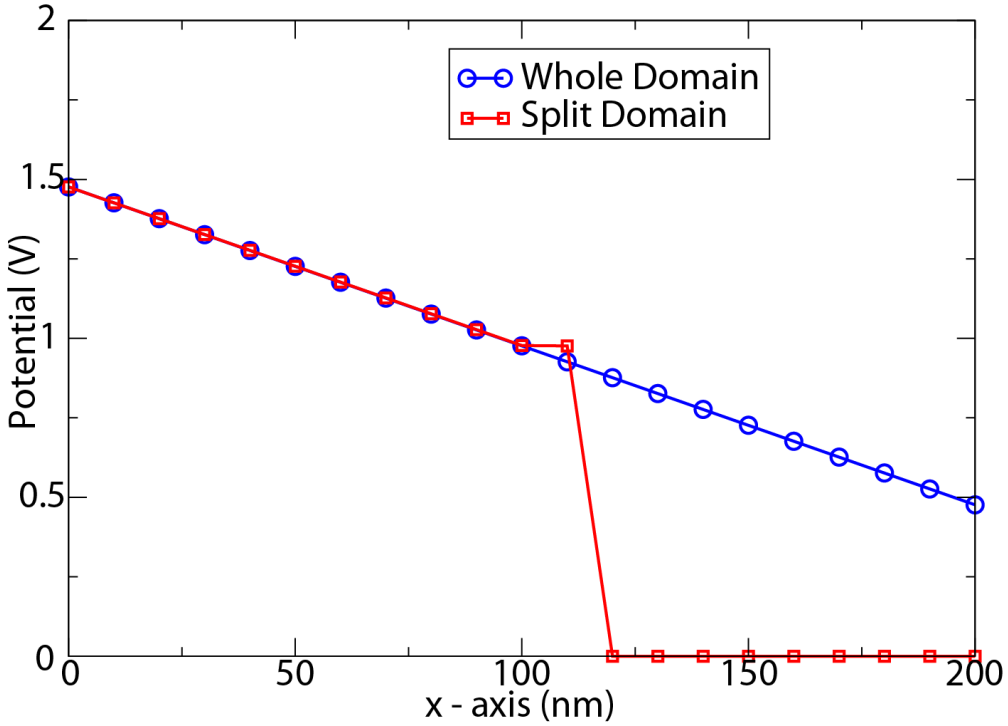

Figure 4.12 – Drift diffusion solution potential for a resistor with 1 volt applied to the first Dirichlet boundary. The blue line shows the correct solution if the whole domain is simulated, the red line shows the result of a split solution. Since the 'contact' region is defined in the XY plane, the potential is fixed in the middle of the device.

simulation domain – and the simulation values were checked throughout the *y* and *z* planes. The temporary Dirichlet boundary between the two simulation domains stretched over two nodes, causing the straight line in the potential profile between 100 and 110 nm.

The results confirm that the drift diffusion simulation is still being carried out correctly with the newly written region partitioning code. As an additional test, the partition boundary was moved from one end of the overall simulation domain to the other, with the code behaving as expected.

4.5.2 Testing a Diode

Additional tests were performed on an NP diode defined using a 200 nm cube with a $25 \times 5 \times 5$ mesh in the *x*, *y* and *z* dimensions. From 0 to 100 nm on the x-axis a donor concentration of $1 \times 10^{24}\,\mathrm{m}^{-3}$ was applied. From 100 nm to 200 nm the same concentration of acceptors was applied. The simulation was carried out over the whole domain using drift diffusion, then over half the domain with a region fixed to the appropriate potential at $x = 100$ nm. Figure 4.13 shows the 1D potential distribution in the test simulations.

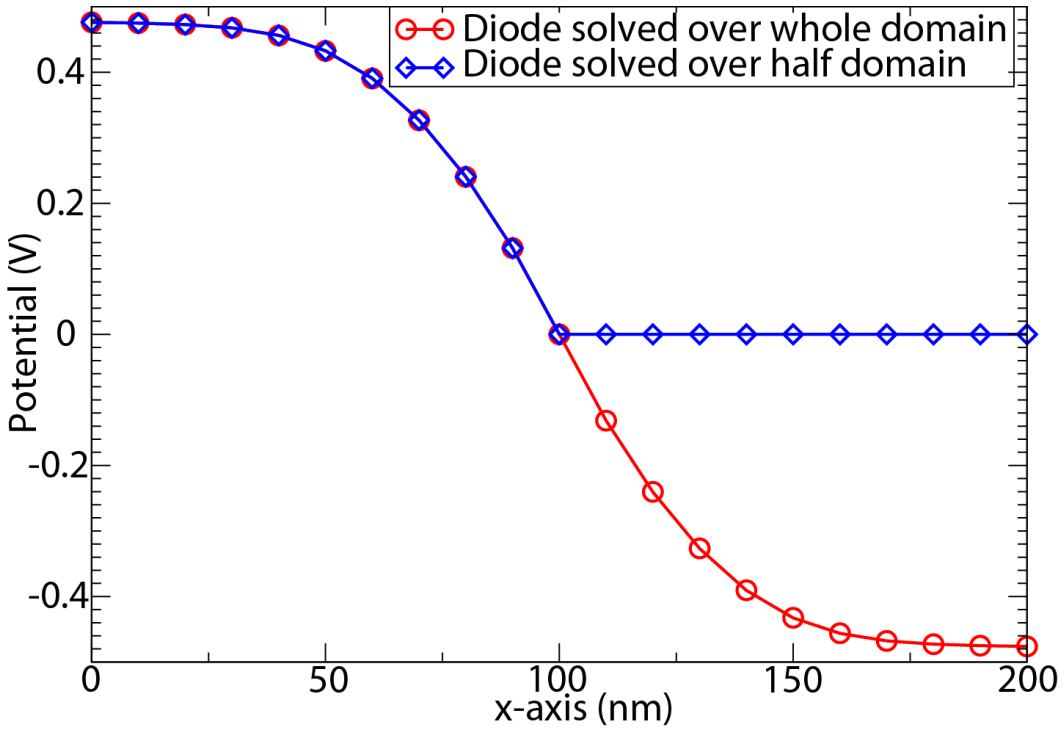

Figure 4.13 – NP diode potentials for the two test structures. A diode structure covering the whole simulation domain and one with a boundary condition at 100nm, solving only between 0 and 100nm.

The results for all solutions behave as expected. In the split solution, it was necessary to set not only the potential at the contact to match the full solution, but also the Fermi levels and carrier concentrations. A 2D plot of the potential in the full device is shown in Figure 4.14. This is included to demonstrate that the potential is correct throughout the device.

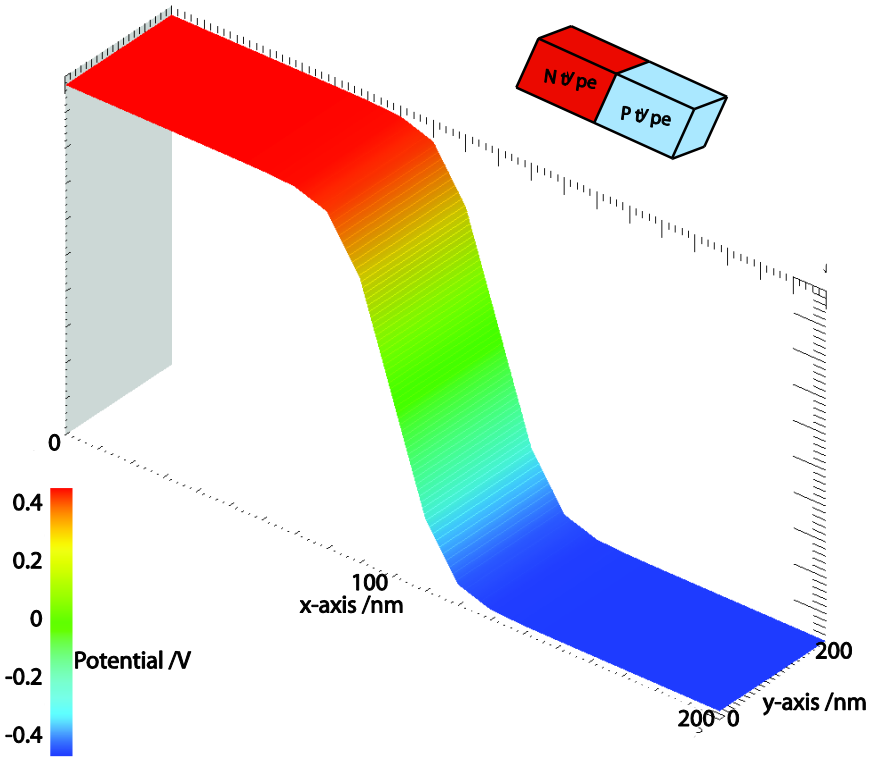

Figure 4.14 – Potential profile through the diode which is solved throughout the domain. This 'slice' is from the centre of the *z* axis.

The carrier concentration distribution must remain consistent even if the domain is split. To demonstrate this, Figure 4.15 shows the electron concentration in the split device. The carrier concentration is 0 in the areas which do not belong to the drift diffusion simulation domain. The code holds values for this area, though, since it will be necessary to store the results of the cloud-in-cell procedure when ions are placed in this region. This more complex structure was included to extend the testing regime in order to ensure that carrier concentrations were solving correctly and charge densities were stored correctly, without interference from the added code.

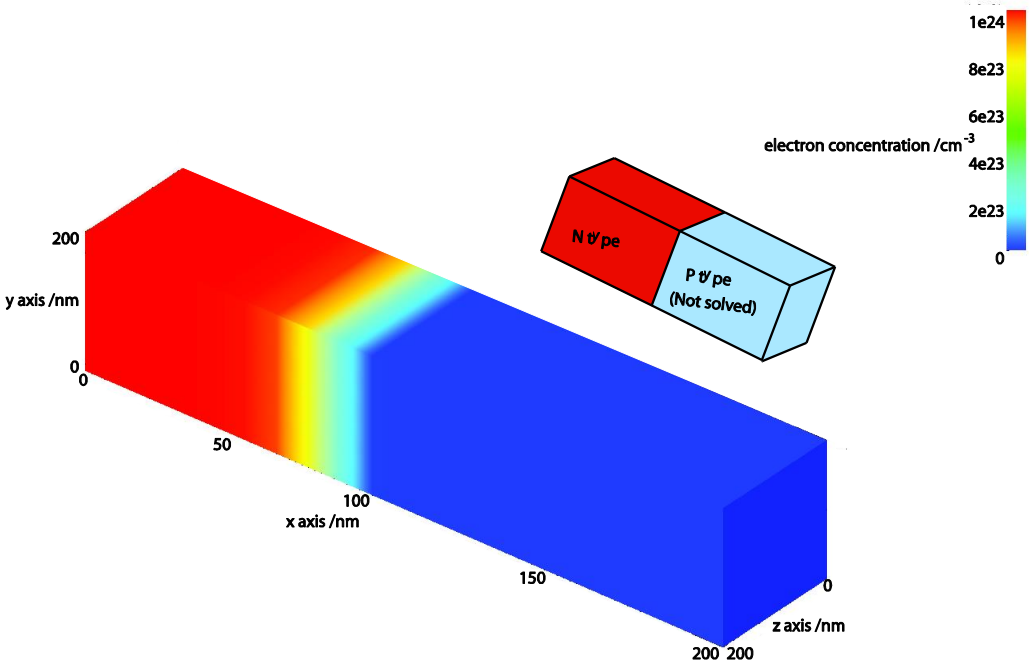

Figure 4.15 – Electron concentration in a split domain simulation. The concentration is zero throughout the non-solved area, while the depletion region is clearly visible in the solution area.

4.5.3 Testing a MOSFET

As a final test of the drift diffusion simulation engine correctly functioning in the software harness of the Brownian code, it was considered useful to simulate a more complex, but still well understood device. A typical state-of-art MOSFET was chosen for this test, and this choice had two additional advantages. Firstly, one research application of a combined drift diffusion / Brownian code is to simulate bio electronic sensors – such as a FET whose gate is sensitive to charge passing through one or more nearby ion channels. The test simulations will therefore have immediate application. Secondly, the natural separation between the two simulation domains in such a problem (Brownian around the active regions of the ion channel and drift diffusion in the FET substrate, separated by a gate oxide), allow a staged testing regime of the full code.

A basic MOSFET structure was therefore developed. In order to ensure that the interface and oxide were being treated correctly, a MOS capacitor with a P type substrate was simulated. The simulation domain was a 100 nm cube with a $201 \times 201 \times 5$ grid size. The size of the device was chosen to accommodate the depletion width, and to allow for additional features to be added to the same device in subsequent tests. A 0.5 nm mesh spacing in x and y was chosen to allow the correct simulation of the oxide. The permittivity of the silicon oxynitride was set to 5.45, and was assigned from 95.5 nm to 100 nm on the x axis and over all nodes on the y and z directions. The remaining area was P type silicon with uniform doping concentration 1×10^{24} m^{-3}. The dielectric constant of the substrate was set to 11.9 and the mobility was set to 900 $cm^{-2}V^{-1}s^{-1}$ which was chosen for this test case – it is not representative of a substrate at this concentration.

The first node on the x axis had an applied bias of 0 V and the final node (acting as the gate) had an absolute bias of 1 V. The depletion region in the MOS capacitor was measured and matched the calculated value from equation for the maximum depletion width [116]. This gave a value of 35.4 nm. Figure 4.16 shows the potential profile of the capacitor, demonstrating that the oxide is operating as expected.

A 2D MOSFET structure was then created. To implement doping profiles more realistic than rectangular blocks of constant doping, Gaussian distributions of

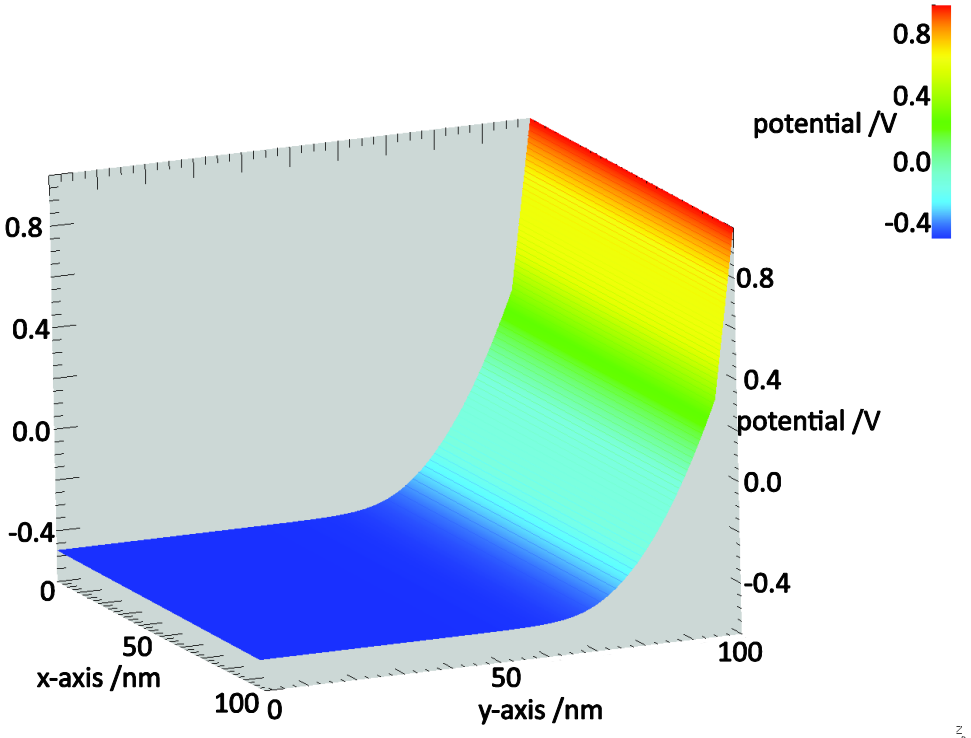

Figure 4.16 – Potential in a MOS capacitor with 1 V absolute bias. (The bottom contact has no applied bias, but is set to the built in negative potential). There is a linear drop across the oxide followed by an exponential drop across the depletion region. The dimensions shown reflect the mesh spacing of 0.5 nm.

dopants was introduced in up to three dimensions. The doping at any location follows a Gaussian distribution depending on the distance from a defined ‘volume of maximum doping’, determined by the maximum doping value, and a standard deviation value. A test case was set up with a single point-like ‘volume of maximum doping’ in the centre of the domain, to check that the Gaussian fall-off in each direction was working correctly. Figure 4.17 shows one of the test cases which demonstrates this distribution.

The simulation domain for the 3D MOSFET was a $100 \times 200 \times 100$ nm with a

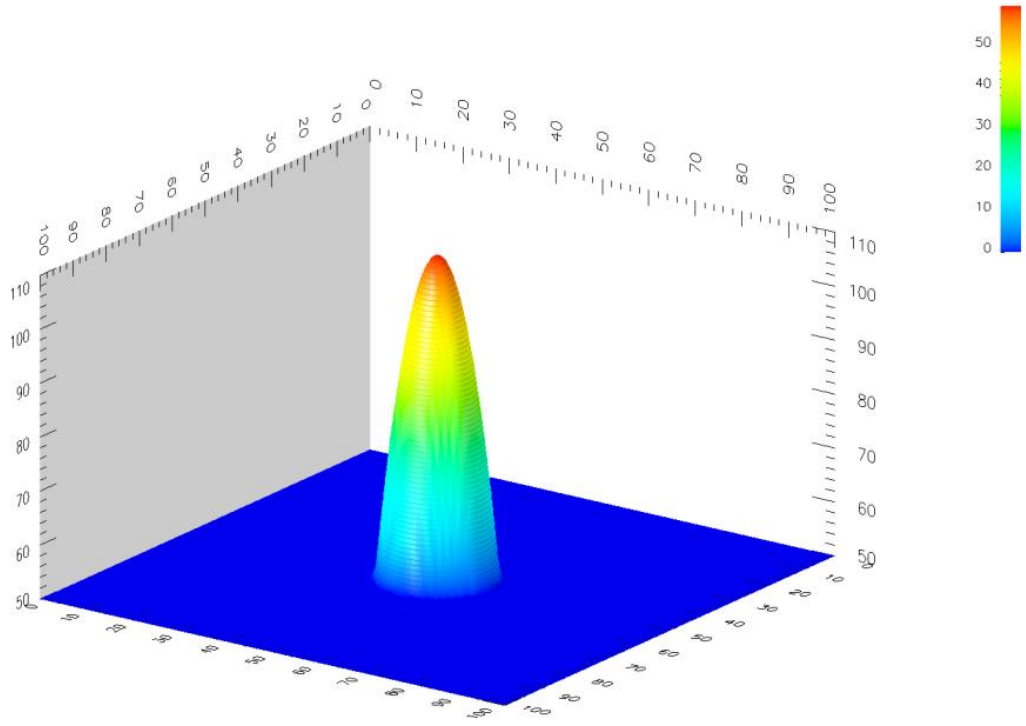

Figure 4.17 – Doping concentration in a Gaussian distribution in two dimensions. This demonstrates that the doping profiles can be created and altered to provide the desired structure.

regular 1nm mesh spacing in all directions. The domain was split 50:50 in the *y* dimension to create the future Brownian simulation area above the oxide. Thus the MOSFET gate oxide and substrate were defined in a 100 nm cube. Gaussian N type regions with peak doping concentration set to 1×10^{26} m^{-3} were added. The oxide was 2 nm of silicon oxide, with a dielectric constant of 5.45. These were constant from $0 \times 90 \times 0$ nm to $20 \times 95 \times 100$ nm for the source region and $80 \times 90 \times 0$ nm to $100 \times 95 \times 100$ nm for the drain region. The *x*, *y* and *z* deviations for the Gaussian profiles were set to 5 nm on the *x* axis and 2 nm on the *y* axis. Source and drain contacts were added as planes at the top of the silicon substrate from 0 to 15 nm and 85 to 100 nm in the *x* axis. The source and drain have applied biases of 0 V and 0.5 V respectively. 1 V was applied to the gate contact which was a plane across the top of the oxide, and 0 V applied to the substrate contact which was a plane across the bottom of the substrate. Figure 4.18 shows the potential distribution after the simulation on this device has been completed. The potentials at the contacts are made up of the built-in bias in addition to any applied bias.

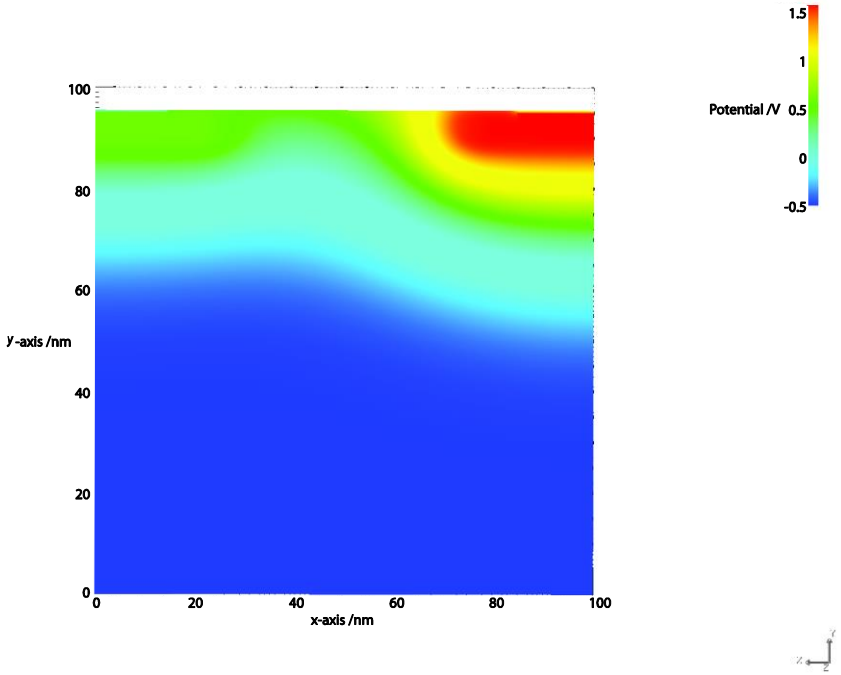

Figure 4.18 – Potential in a MOSFET, the region shown is below the 2 nm oxide layer. The applied bias is 1 V on the gate, 0.5 V orain and 0 V on the source contact.

Having confirmed that the electrostatics of the MOSFET structure at fixed gate potential are as expected, by considering the potential profile of Figure 4.18, an I_dV_g curve was simulated under the same source/drain bias conditions. 20 bias points were simulated between V_g = 0 and V_g = 3 Volts. Figure 4.19 shows the output of this voltage sweep. The device has a threshold voltage of approximately 1 V and a subthreshold slope of 120 mV/decade, though it should be noted that this is not a manufacturable device.

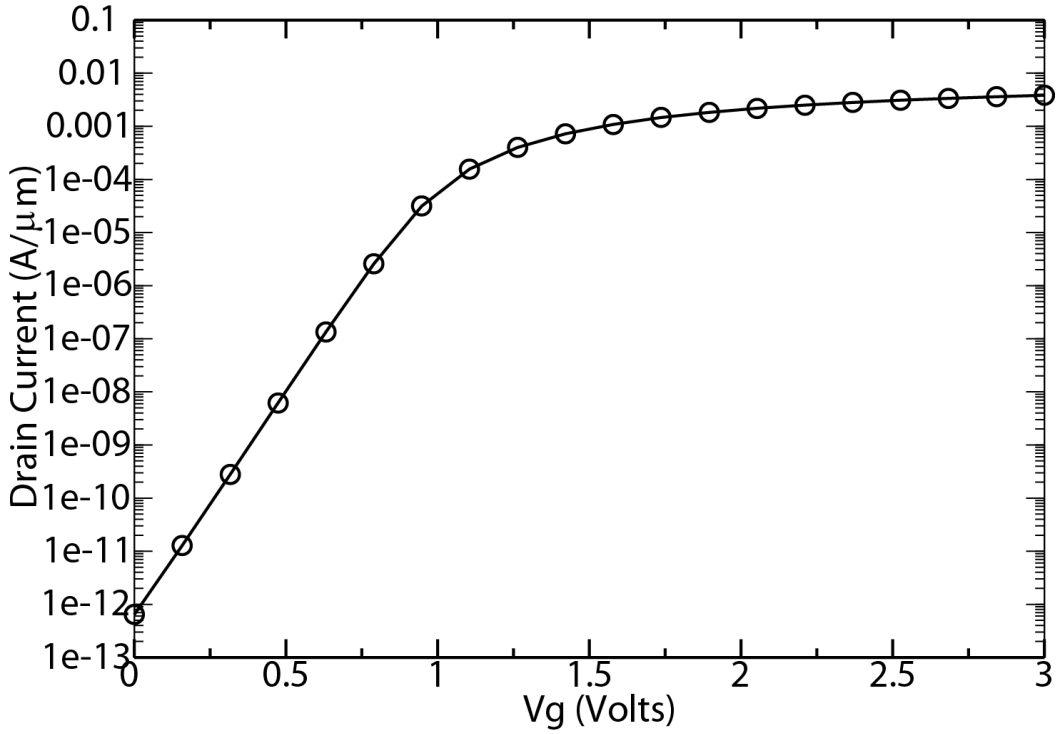

Figure 4.19 – Current Voltage characteristics for a basic MOSFET. The threshold voltage is approximately 1 V and the subthreshold slope 60 mV./decade. This device is, however, not manufacturable.

The final stage in testing a MOSFET was to introduce a test case against a previous known working code. A system was developed to produce identical devices in the Glasgow "Atomistic" Simulator [115] and the newly developed drift diffusion simulator. These devices were created to have a nominal 35 nm gate [117]. The solution domain representing the analytical MOSFET has dimensions $108 \times 75 \times 3$ nm with peak source and drain N^+ doping concentration of $1 \times 10^{26}\,m^{-3}$ and a P type doping throughout the substrate of $5 \times 10^{24}\,m^{-3}$. The source and drain doping profile is approximated using a Gaussian distribution. The oxide layer is 2 nm of silicon oxynitride. A Dirichlet boundary is applied at the top of the gate dielectric to approximate metal gate conditions. Ohmic contact

boundary conditions are applied at the source and drain contacts and at the bulk contact. Neumann boundary conditions are applied at all other boundaries.

The Current-Voltage characteristics of the prototype MOSFET are shown in Figure 4.20 where low drain conditions are with 0.1 V applied to the drain contact, and high drain conditions are 0.8 V applied to the drain contact. The transistor has a threshold voltage of approximately 300 mV and a reasonable subthreshold slope of approximately 86 mV/decade. These graphs match to 0.08% worst case error at high drain voltage and 0.03% worst case error at low drain voltage.

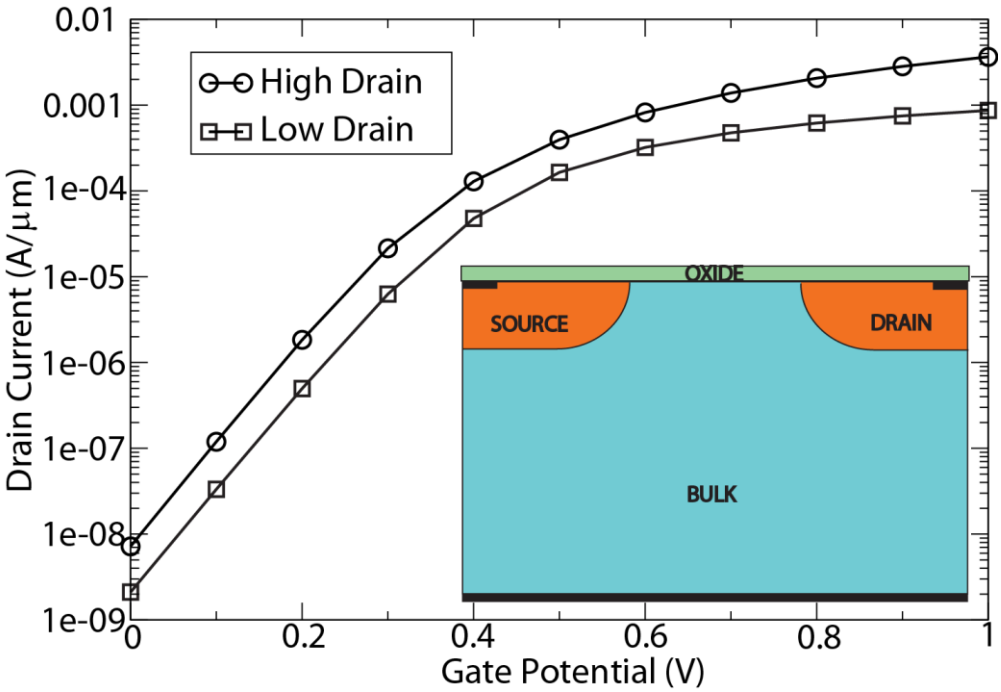

Figure 4.20 – Analytical MOSFET current for high (0.8 V) and low (0.1 V) drain potential cases. The device structure is shown inset. The black sections denote a contact modelled as a Dirichlet boundary, and there is an additional Dirichlet boundary across the top of the oxide which acts as the gate. The threshold voltage is approximately 300 mV and there is a subthreshold slope of approximately 86 mV/decade.

4.5.4 Extending the Domain

Having created a working MOSFET structure, the creation of a single domain employing both simulation domains is the next step. The structure chosen to move towards jointly active Brownian dynamics and drift diffusion simulations used the same MOSFET structure, but now including a 77 nm region of water which directly interface the oxide. A Dirichlet contact is placed as a plane – a single mesh point in the *y* axis at the bottom of the bulk, where it covers the *x* and *z* axes. Dirichlet contacts are also placed in the source and drain covering the top point of the source and drain regions and the mesh point of the oxide, and extending 15 nm from the edges of the device in the covering the top point of the source and drain regions and the mesh point of the oxide, and extends 15 nm from the edges of the device in the y dimension. All other boundaries were Neumann boundary conditions.

To allow both techniques to operate, a contact at the 'bottom' of the oxide (75 nm on the *y* axis stretching from 15 to 93 nm in *x*) which will operate on the Brownian region and one at the 'top' of the oxide (77 nm on the *y* axis stretching from 15 to 93 nm in *x*) which will operate on the Drift Diffusion region. This means that the oxide overlaps each simulation type in order to reduce the non-physical effects of the Dirichlet boundary conditions, since the oxide is an insulator, there is no requirement to convert the charge of single ions into an equivalent concentration. The simulation domain regions and contacts are illustrated in Figure 4.22 and Figure 4.23.

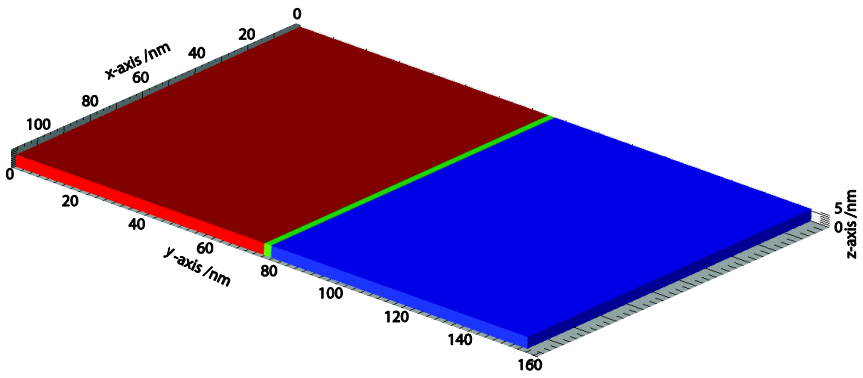

Figure 4.22 – Simulation domain showing simulation types. Red denotes DD, blue denotes Brownian. The green region which is the oxide identifies the region which is simulated in both simulation techniques.

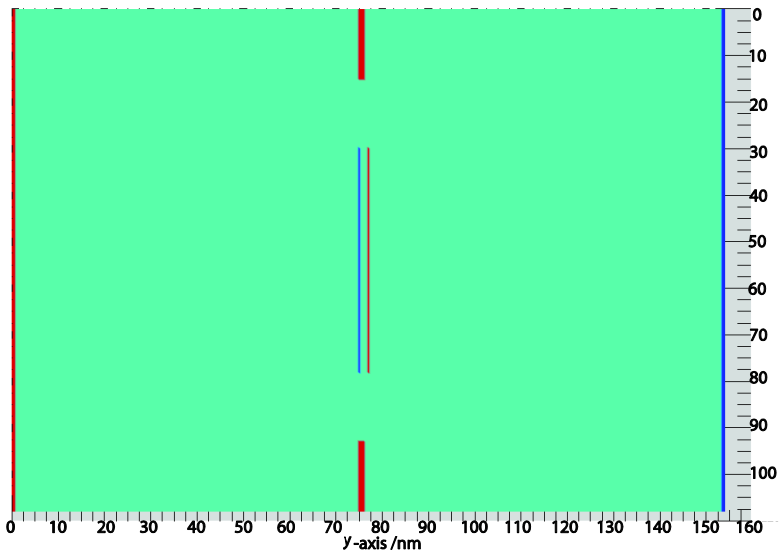

Figure 4.23 – 2D representation of the simulation domain. Red denotes Drift Diffusion contacts, and dark blue shows the Brownian contacts. The surrounding regions in light blue are the non-fixed areas.

The boundary conditions at the oxide are considered ‘static’ during the solution of the corresponding simulation technique, but are updated during the calculation of the ‘opposite’ simulation technique, i.e. drift diffusion simulation changes the Brownian contact values and vice versa. Iterating the simulation, until these boundary conditions converge, allows the simulation of the whole domain to be solved self consistently.

Poisson’s equation must be solved over the whole domain. A linear SOR solver was used in the Brownian region while Poisson’s equation is solved in the drift diffusion area using the original non-linear SOR solver.

While it is important that both simulation domains can operate independently, it was decided that, when the domain is being solved as a single unit, a single Poisson solver would create the best coupling. This allows the effect of the charge in the Brownian region to affect the potential throughout the simulation domain, as it should. This, in turn, allows the domains to affect the charge carrier concentrations in their respective domains. This results in direct coupling between the two simulation domains.

The non-linear SOR solver developed for the drift diffusion solver is the best candidate for the solution in the whole domain. It already calculates the right hand side of the Poisson equation for the mobile charge concentrations as required in drift diffusion, but was developed so that it would do this in selected material types only. As a result, a small change to the code ensured that, while solving over the whole simulation domain, the charge concentration in the Brownian domain of the simulation was not altered, while the potential could be updated.

In this case an individual SOR solution to the Poisson equation in the Brownian region using the boundary condition at the bottom of the oxide used as a starting point to the full solution using the non-linear solver over the whole domain. This was tested and the potential profile in Figure 4.24 was generated. It is clear that the solution in the Brownian region is almost linear, as expected in a uniform dielectric. The solution is still being affected by the source and drain contact regions, which were also found to increase the local potential gradient in the surrounding oxide.

While this solution allows the calculation of the potential throughout the domain, three additional changes were implemented. The first was the removal of the contacts in the centre of the gate. Instead, the drift diffusion solution was always

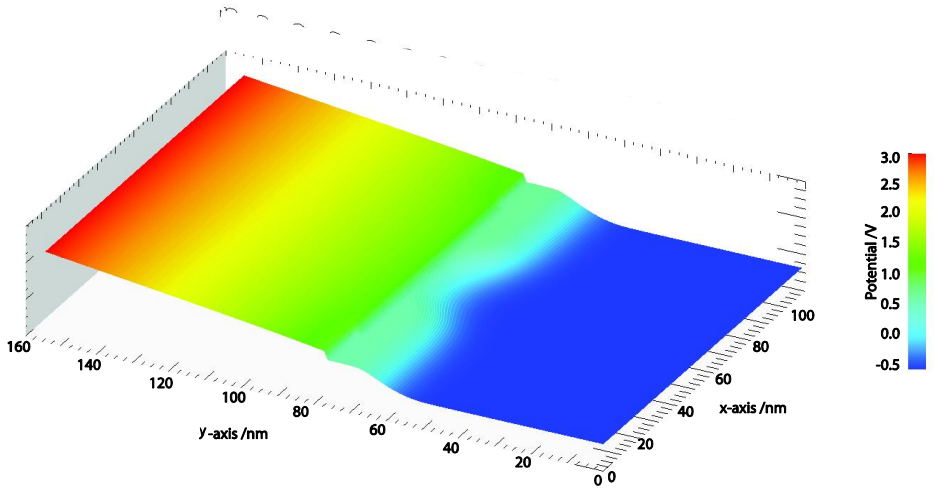

Figure 4.24 – Top view of the potential in the device as solved with a single Poisson solver.

conducted over the whole domain, while the top of the oxide was used as an unchangeable reference point for the Brownian dynamics solution. Secondly, the source and drain contacts were altered to be a plane at the top of the silicon substrate, ensuring that the localised effects seen in Figure 4.24 are reduced.

Finally, the SOR solution for the intermediate Brownian steps was too slow, and an alternative BiCGStab solver has been developed for intermediate steps where only the Brownian regions are simulated, since this allows a significant speed-up. The following section describes the reason for this change in more detail.

4.5.5 Using Dual Solvers

The Non-linear SOR Poisson solver is stable but computationally slow when used in conjunction with a particle simulation, which does not require the recalculation of the right hand side of Poisson's equation. For this reason it was decided to use the BiCGstab solver for intermediate iterations of the Brownian solution, but to use the non-linear SOR solver, working as a linear solver in the Brownian region, for the whole solution.

To ensure that the interface between the solvers worked, it was necessary to implement the solver in a way that guarantees correct values in both regions. For this test, a 33 nm slab of water replaced the gate electrode at the top of the FET described above. This was chosen to allow an area large enough to accommodate the addition of a nano-pore in later tests. A gate electrode modelled as a Dirichlet boundary was placed as a plane contact at the top of the water. The device was

108 × 110 × 3 nm in total, with the *y* dimension being including 75 nm of silicon to form the FET, 2 nm of oxynitride and 33 nm of pure water. The dimensions of the silicon section of the device were chosen to match the previously described 35 nm FET.

The major advance of this test was the use of the oxide as an interface. As an insulator, it is assumed to have no mobile charge. This makes it the ideal interface region and, instead of having contacts at either side of the oxide to act as boundary conditions, the whole oxide is simulated in both techniques and the nodes adjacent to the oxide act as a Dirichlet boundary. The use of the same arrays within the code mean that the solvers have identical values of potential at the nodes on both sides of the oxide, but cannot change their values, thus acting as Dirichlet boundaries.

In order to achieve a mix of efficiency and ease of programming, the goal was to allow a solution in the aqueous region which uses a linear BiCGstab solver, and a solution over the whole domain, including the aqueous region, using the SOR solver. This is because charge movement in the aqueous region is significantly slower than that in silicon, meaning that it will take a number of iterations for a change in the aqueous solution to have a significant effect on the electrostatics in the FET. While this is a large assumption, the decision was made to proceed in this way as it allowed for a significant reduction in compute time for a simulation.

To ensure that this method does not introduce changes in the basic electrostatics of the whole system, a test was designed whereby the solution was carried out in two separate ways. The first involved solving the aqueous region using the BiCGstab method and using the boundary data from this region to solve the FET region. The two solvers were used self consistently. The second method used

SOR over the whole region to ensure solutions, linear in the aqueous solution and non-linear in the FET region. While this is a somewhat simple test without mobile charges in the aqueous region, it ensures that no major errors were introduced when using both systems in combination in later, more complicated tests.

The initial conditions are identical in both cases; all water is set to the same voltage as the top contact – in this case 1 Volt. This top contact is the only completely fixed point in the Brownian region. The silicon and oxide are set up as before: The oxide potential is 0 at the start. The silicon is set up so that the source region is at the built in potential, the whole drain region is at the built in potential, with an additional bias of 1 V. The bulk contact is set to 0 V plus the built in voltage (in this case negative because it is a P-region). All other regions of silicon are initialised to ensure electroneutrality. The 4 Dirichlet boundaries are at the top of the water, the bottom of the silicon and at the top of the source and drain regions. In the split system, the BicgSTAB is used from the oxide to the top of the water and the SOR is used from the bulk to the top of the oxide creating an overlap of solutions throughout the oxide.

A Gummel loop is used to secure convergence between the solutions. This is done for 200 iterations, with no early exit criteria. The SOR solution is performed first, for 100 iterations. The BiCGstab loop is then performed for the same number of iterations and the process repeats. This solution was then compared to one which uses the non-linear SOR in the whole domain. The results over the whole domain for both simulations are shown in Figure 4.25 which shows that the potential profile throughout the device matches to machine precision. To further illustrate this, a sample through the centre of the *x* and *z* plane is shown along the *y* axis in Figure 4.26.

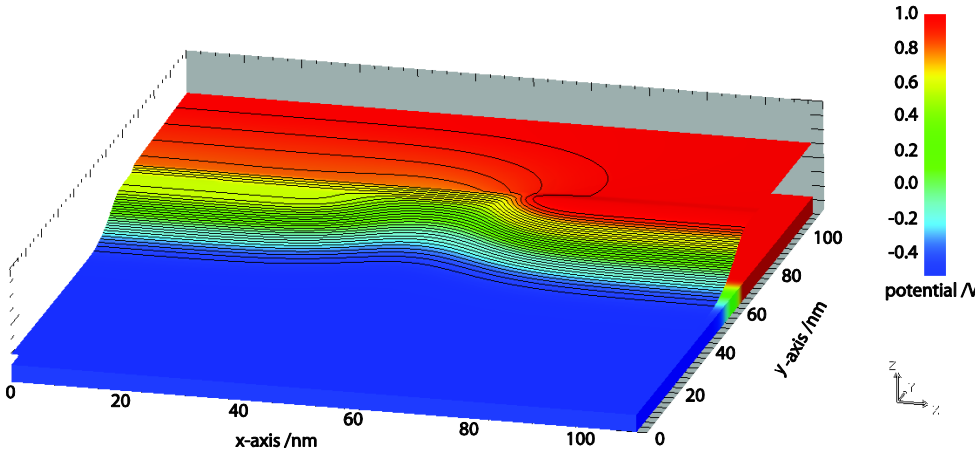

SOR Only

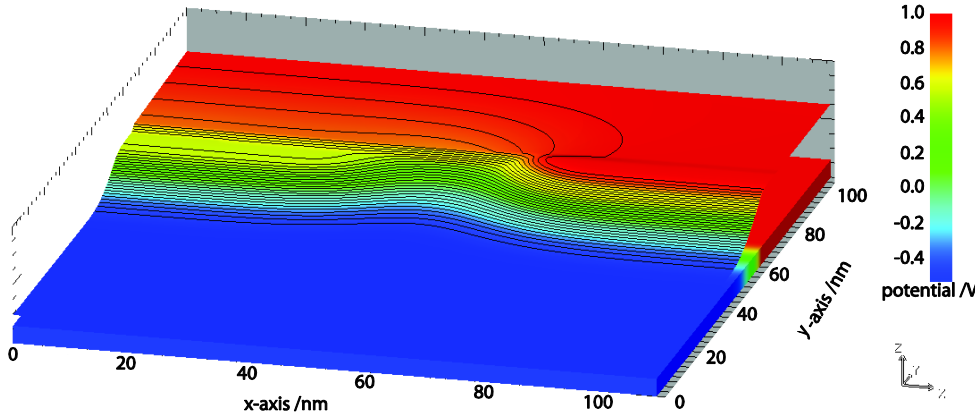

SOR and BiCGStab Combined

Figure 4.25 – 3D potential profiles of the SOR only simulation and the combined simulations.

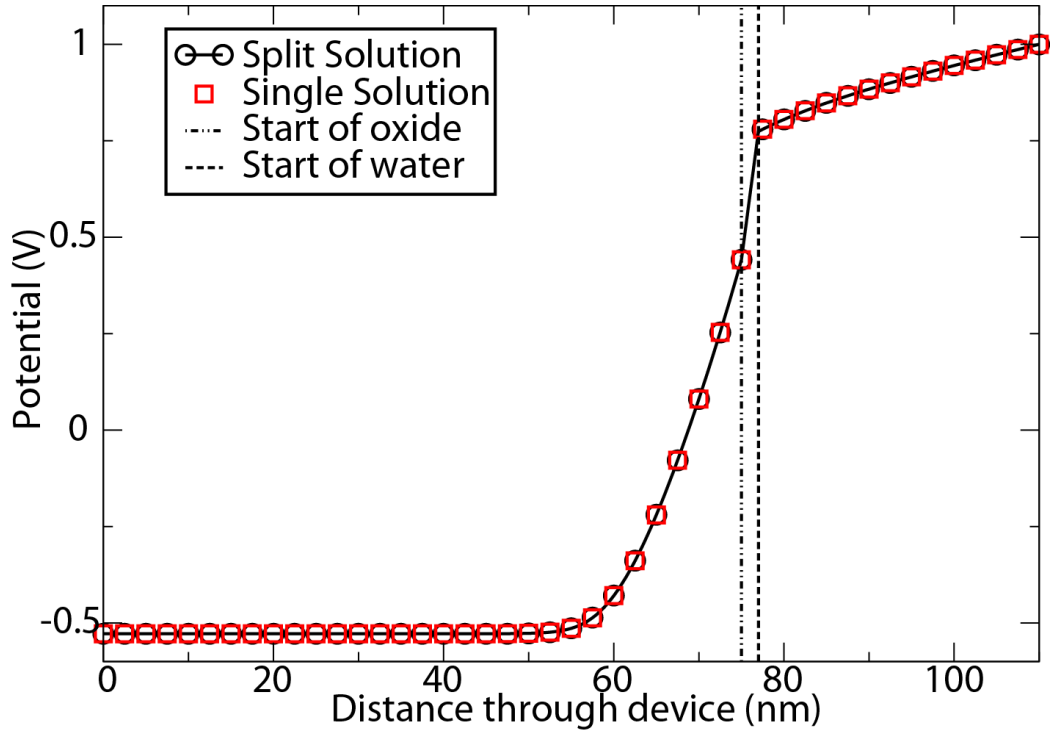

Figure 4.26 – Cross section of the potential running from bulk contact through the channel to the top contact of the water. A small depletion region is visible between 77 nm and approximately 82 nm. The red squares denote the single SOR solution, the black line with circles is the split solution.

4.5.6 Introducing Ions

The next stage of the simulation development is to introduce ions to the Brownian region. This is in the form of particles, but the charge in each cell must be passed into the Poisson solver. The final test before moving onto new simulations, the use of the SOR solver alongside within the Brownian region with Brownian dynamics charge transport enabled. There were two elements to this test, first to ensure that the movement of ions had been unaffected by changes made to the

codebase, and secondly to ensure that the new elements, including movement of the description of charge density between domains, and flag setting, operated correctly.

To do this, the region of water above the MOSFET was changed to emulate a resistor, with the FET structure maintained to allow error checking in this region. The structure remained the same – 108 × 110 × 3 nm with 0.5 nm mesh spacing, The *y* dimension consists of 75 nm of silicon to form the FET, 2 nm of oxynitride and 33 nm of water. A 1 molar concentration of chloride and sodium ions was included in the aqueous region.

The simulation was performed using the SOR solver in order to check the operation of a resistor in the Brownian region using this solver. The applied potential across a Dirichlet boundary at the top of the water region was altered between 0 V and 1 V at 0.1 V steps and the solution repeated, with 0 V applied to a Dirichlet boundary placed across the top mesh point of the oxide throughout the tests. As stated, the FET structure remained intact to ensure no errors occurred in this region during the solution to the Brownian simulation, and this region remained set to the initial conditions throughout the simulation.

The current matched the analytical result showing that the charge movement and current calculations are accurate. Figure 4.27 shows the potential in the device. The FET region of the device remains consistent with the initial conditions setup in the code, and this region was checked against known values to ensure consistency of numerical values. The water region at the top of the solution shows the peaks and troughs in the potential distribution expected due to the distribution of individual ions, with the overall trend showing a constant gradient between the contacts.

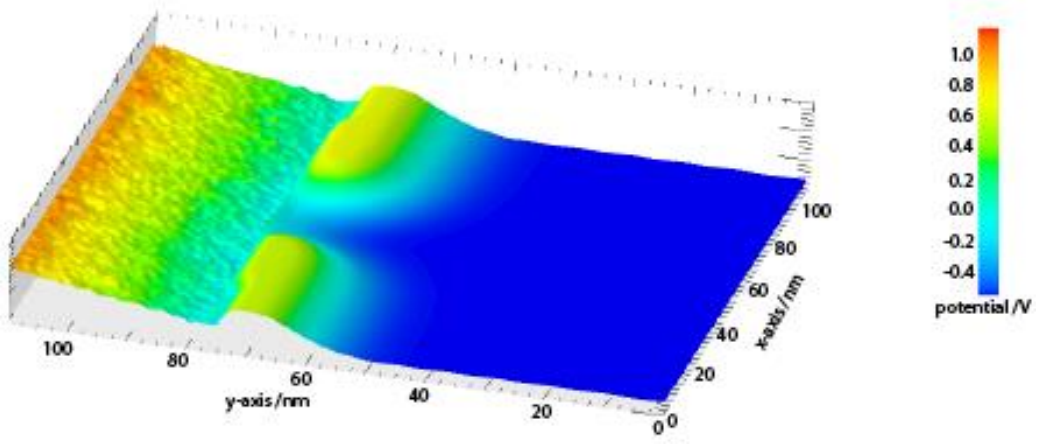

Figure 4.27 – Sample potential (not averaged) when the bias is 1 V on the contact. The MOSFET potential is isolated from the Brownian resistor region in this simulation since there is a contact across the top of the oxide. The MOSFET has been left in the picture to show that the numerics are unaffected by the Brownian region.

This confirmed that the ions were being treated correctly, and that the solution in this region had no adverse effects in the FET region. This was the final step in allowing simulations using both regions in combination, as described in chapter 6.

4.6 Conclusion

In this chapter, the development and testing of a simulation framework including drift diffusion and Brownian simulation domains coupled through the solution of Poisson's equation has been described. To the best of my knowledge this is the first simulation framework of this kind. It combines the advantages of two

separate simulation methodologies to be combined to create an efficient bio-nano-sensor simulator which is capable of resolving the effect of individual ions.

A strict testing regime was employed to ensure accuracy throughout the whole process of development. Multiple comparisons were made to both analytical results and previous standards. This testing included interfacing an analytically doped gateless MOSFET to an aqueous ionic solution in order to test the functionality of the simulator. The rigorous testing has shown that the simulation methodologies can work in tandem, and that the oxide provides an ideal interface for the two systems.

Chapter 5

Static Simulations

5.1 Introduction

This is the first of two chapters presenting research results obtained by the newly developed dual particle/continuous simulator. The research presented in this chapter aims to investigate whether the drain current of a nanoscale FET will be sensitive enough to detect the movement of an individual ion through an ion channel, or a nano-scale pore. This is relevant to the detection of single ion charge under practical experimental conditions. This chapter presents simulations which were performed without the impact of natural stochastic ionic movement in the solvent above the FET structure. It analyses the core response of the FET and the best case sensitivity of the system. It details simulations which are performed with and without a bath of ions in the aqueous solution, but with the ion bath modelled by using the drift diffusion approximation. These simulations serve as a baseline to understand the impact of a single ion on the drain current of the FET, and also after the opportunity to rigorously test the simulation harness.

The simplest possible material structure is first tested, including all the necessary contacts and boundary conditions needed for a more realistic simulation. After confirming that the results of this simulation agree with analytic results, the effect of a single additional localised ionic charge into the aqueous solution is investigated. Finally a realistic lipid layer is introduced with a nano-pore at the centre and single ions are artificially moved through this pore to observe the resultant changes in the FET drain current.

5.2 Electrolyte Solution Interfacing a FET

As a first step in constructing the sensing analytical FET the metal gate electrode of the MOSFET from the previous chapter (see section 4.5.3) was substituted by pure water with a reference gate electrode at the top of the solution domain implemented using a Dirichlet boundary condition. This simulation structure is shown as an inset diagram in Figure 5.1. The overall simulation domain is $108 \times 110 \times 3$ nm with a uniform mesh spacing of 0.5 nm in all dimensions. The gate dielectric is a 2 nm layer of silicon oxynitride with $\varepsilon_{ox} = 5.45$ above which is a 33 nm layer of pure water with a dielectric constant of 80. The size of the layer was chosen to allow for the introduction of a 3 nm lipid layer in later tests allowing a viable distance between the FET and the nanopore. By including this area at this testing stage, direct comparisons can be made between tests with and without the lipid layer. This significantly larger area allows for the placement of electrodes above and below the lipid, and an investigation of the importance of the placement of the lipid layer in later tests.

The solution domain representing the analytical MOSFET has dimensions $108 \times 75 \times 3$ nm with peak source and drain donor doping concentration of

1×10^{20} cm^{-3} and a continuous acceptor doping of 5×10^{18} cm^{-3} throughout the substrate. The device has a nominal channel width of 35 nm. The source and drain doping profiles are approximated using 2D Gaussian distributions. Ohmic contact boundary conditions are applied at the source, drain and substrate contact. Neumann boundary conditions are applied at all other boundaries, including at z = 0 nm and z = 3 nm. This means that the effect of the mirror charge (at 3 nm) in the z dimension will be lower than 3% of that at 0.5 nm.

Simulations were carried out with drain biases of 0.8 V and 0.1 V. In both cases a gate voltage sweep was performed from V_G = 0 to V_G = 1.0 V. The corresponding current-voltage characteristics are shown in Figure 5.1. Compared to the equivalent metal gate MOSFET characteristics (see Figure 4.20), the subthreshold slope is approximately 1.5 times larger at 140 mv/decade and the threshold voltage is approximately 2.2 times greater reaching 660 mV, although the slope of the characteristics remains the same. This reflects the increase in the equivalent oxide thickness of the transistor due to the insulating layer of water. The corresponding value of C_{ox} is 1.8 times greater when the water is introduced. Figure 5.2 shows the 3D potential distribution across the transistor at a gate bias of 0.2 V and a drain bias of 0.1 V. Due to the high dielectric constant of water, there is only a voltage drop of approximately 0.6 V across this region.

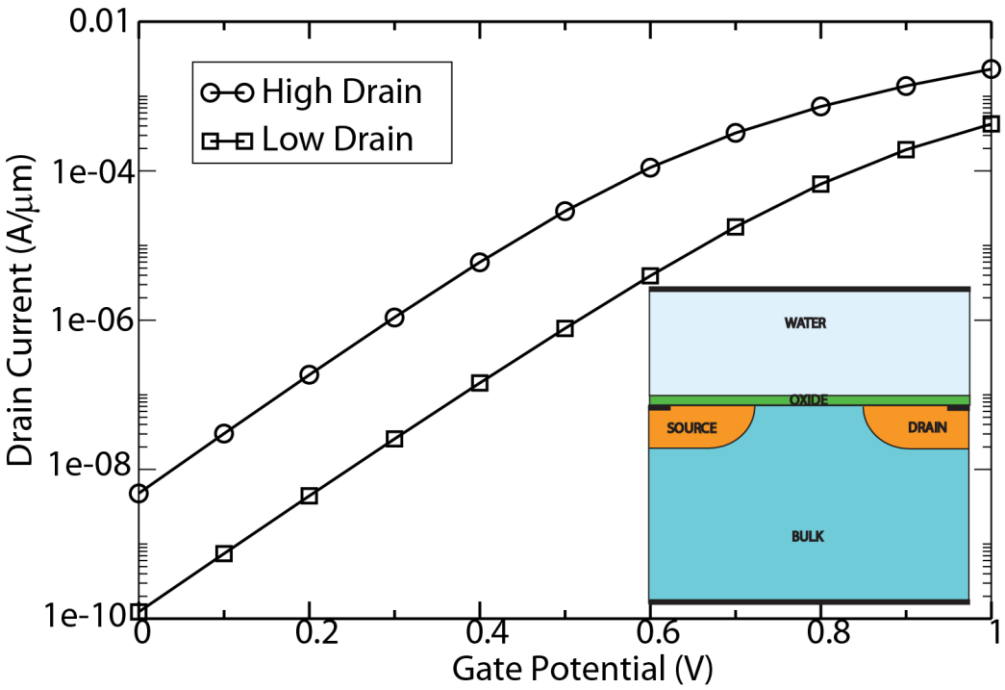

Figure 5.1 – Drain current in an analytical WOSFET. The device operates in the same way as the MOSFET, but requires higher gate potential for the same output current. Both high (0.8 V) and low (0.1 V) drain cases are considered. The device structure is shown inset with the reference contact at the top.

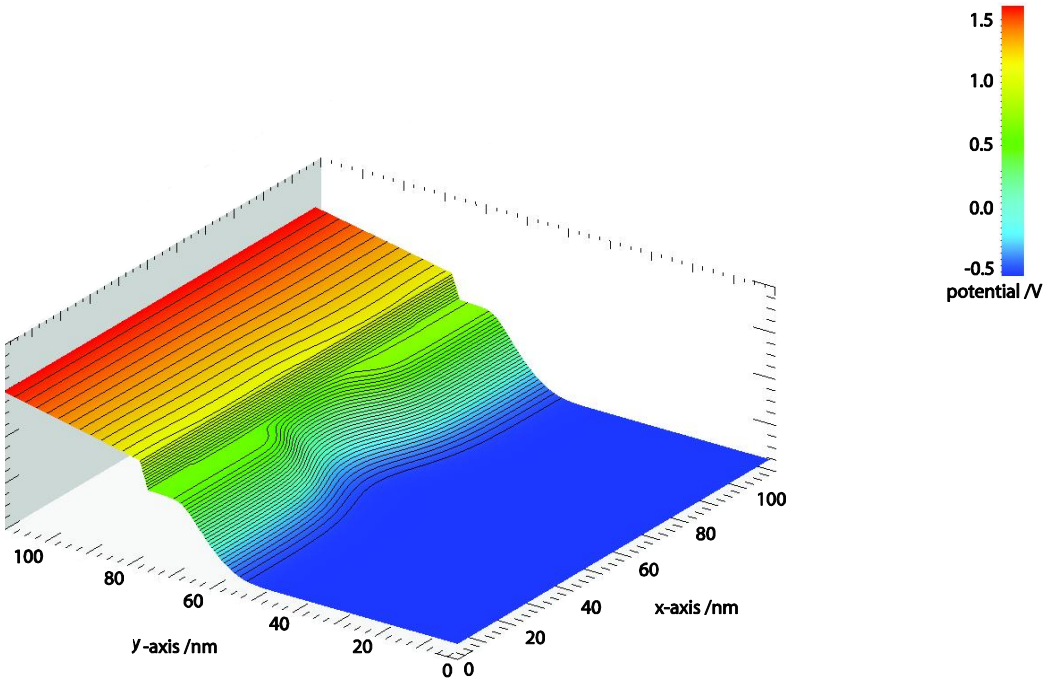

Figure 5.2 – 3D potential plot of the analytical FET device. The voltage drop across the water is almost constant, with slight bending towards the drain end as the drain potential (0.1 V) causes a slightly smaller drop at the drain end.

This simulation domain was then altered to include two further ohmic contact Dirichlet boundaries at the left and the right of the aqueous area. These were required for future simulations which would allow the introduction and removal of ions from the simulation domain when bias is applied between the top and the side solution electrodes. These contacts are set to identical potentials as the source and drain contacts as this is the expected mode of operation for any real experimental arrangement. The position of these contacts is shown as an inset diagram in Figure 5.3. At this stage equal $6.02 \times 10^{26}\,\mathrm{m}^{-3}$ concentrations of sodium and chloride 'ions' were introduced as positive and negative charge mobile concentrations in the water – although not yet modelled as discrete

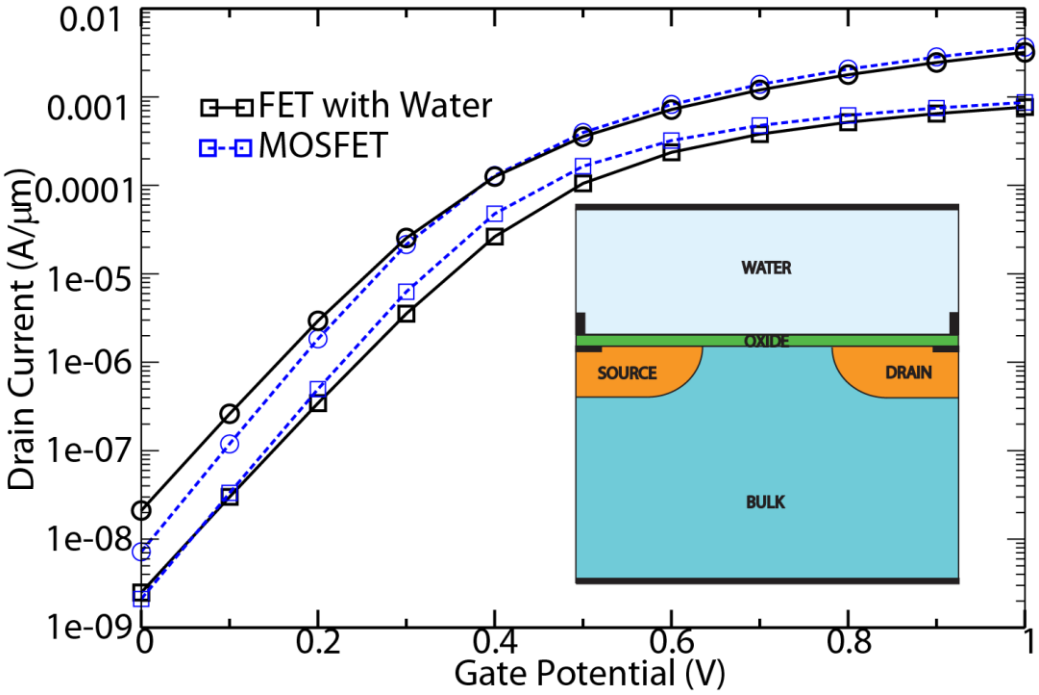

Figure 5.3 – Drain Current – Gate Voltage characteristics for the improved structure compared to the analytical MOSFET for high (0.8 V) and low (0.1 V) drain potentials (denoted by circles and squares respectively). The structure of the improved device is shown inset.

particles but as charge concentrations in a full drift diffusion simulation. With an ionic aqueous solution the system should now behave more as a typical MOSFET.

Using the same high (0.8 V) and low (0.1 V) drain biases, a voltage sweep (from $V_G = 0$ to $V_G = 1.0$ V) the results of Figure 5.3 were obtained and compared to the equivalent characteristics of the MOSFET as previously described in section 4.5.3. The subthreshold slope has worsened from 84 mV/decade to 92 mV/decade, and the threshold voltage has increased by approximately 50 mV. The increase in effective C_{ox} accounts for the threshold slope change and the subthreshold slope change is as a result of the formation of a depletion layer at the interface between the aqueous solution and the oxide which is similar to the depletion layer in a

heavily doped poly-silicon gate. The corresponding bending of the energy bands at the surface of the oxide means that a greater gate electrode potential (V_G) is required to reach V_T.

Figure 5.4 shows a 3D potential distribution in the simulation domain for a gate bias of 0.2 V and a drain bias of 0.1 V. The potential distribution is altered by the presence of applied bias inside the aqueous solution, but the general trend remains the same as that in Figure 5.2.

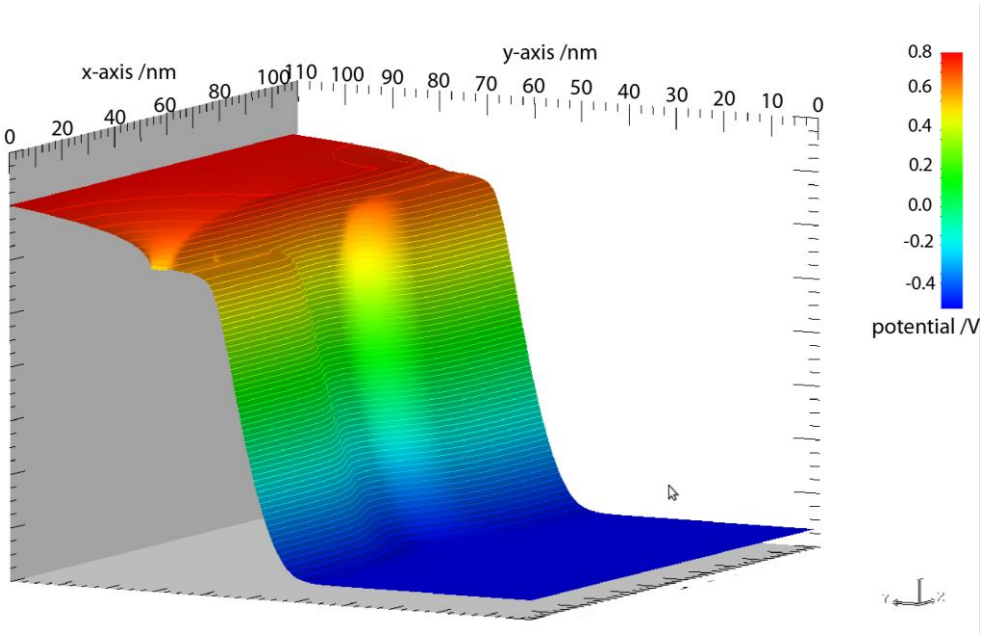

Figure 5.4 – 3D potential plot of a FET device with a pure water section above the oxide. The solution was performed solely with Drift Diffusion. This represents the steady state condition of the WOSFET allowing a calculation of the expected average current in the device.

5.3 Fixed Charge Sensitivity

Having obtained these benchmark results, the next stage is to introduce discrete ionic test charges in the aqueous region. An initial test was performed to analyse the effect of a single ion on FET drain current, and thus the sensitivity of the FET to discrete ions in water. The simulations were performed with a gate voltage of 0.2 V, deep in the sub-threshold regime where the FET current is most sensitive to changes in gate voltage. The charge of the single particle, 1.602×10^{-19} C, is assigned to the mesh using a cloud in cell approach. For this simulation there is only one Dirichlet boundary condition in the aqueous region. No boundaries are present in the area above the source and drain contacts.

The particle is moved along a vertical line in the middle of the gate from 1nm above the oxide to 33 nm above the oxide with 2 nm spacing. The results are shown in Figure 5.5 for both high (0.8 V) and low (0.1 V) drain bias cases illustrating the high sensitivity of the analytical FET to individual discrete charges.

The same single charge was then placed at various points in the water, moved vertically by 1 nm and the change in resulting drain current compared against the solution with no fixed particles in the simulation. Again, the gate voltage was a constant 0.2 V, and high (0.8 V) and low (0.1 V) drain bias values were examined. The simulations were carried out with the particles above the source contact edge, approximately above the source-channel pn junction, in the middle of the channel, approximately above the channel-drain pn junction and at the edge of the drain contact.

Figure 5.5 shows the effect different positions of the fixed single ion on the drain current when it is moved above the middle of the channel. In this position in the *x*-*z* plane there is an exponential dependence on the distance from the gate dielectric due to the Coulomb potential associated with the single ion. As it approaches the gate dielectric, the effect of the resulting charge exclusion region will increase. Figure 5.6 shows the effect in the positions above the source and drain regions. They are shown separately due to the much larger percentage increase caused by the particle when placed above the middle of the channel. When the particle is placed above the source or drain within 5 nm of the oxide,

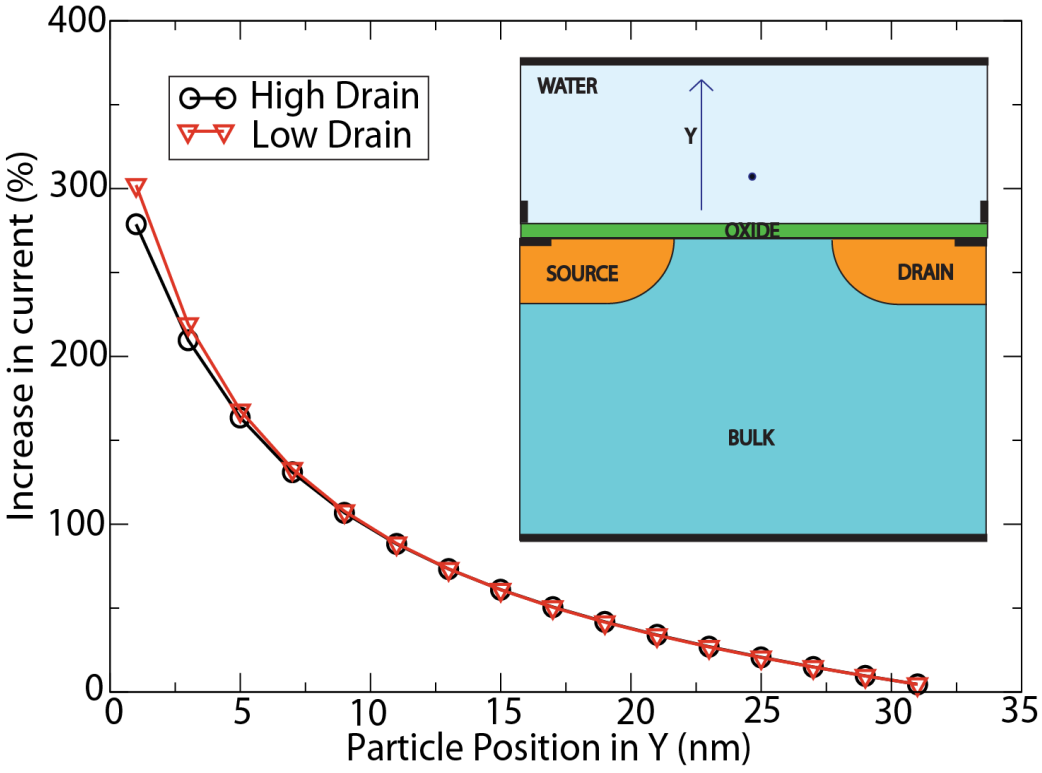

Figure 5.5 – Percentage increase in the device drain current as a function of particle position in Y at the centre of the channel. The increase is in comparison to the situation where no particle is present. The device structure is shown inset with a single particle indicating how the particle position is varied in the Y dimension.

the increase in drain current is reduced. This effect is due to the interaction with the Dirichlet boundaries, which limit the effect of the localised increase in potential caused by the single ion due to screening. These results show that the Dirichlet boundaries must be placed carefully, as far from the area of interest as possible.

As a final test of the sensitivity, simulations were performed with the single positive ion located at 1 nm intervals on the x and y axes. The ion was at the centre of the z dimension (1.5 nm) throughout. As before, the drain current was compared to the value obtained when no ion was present in the solution.

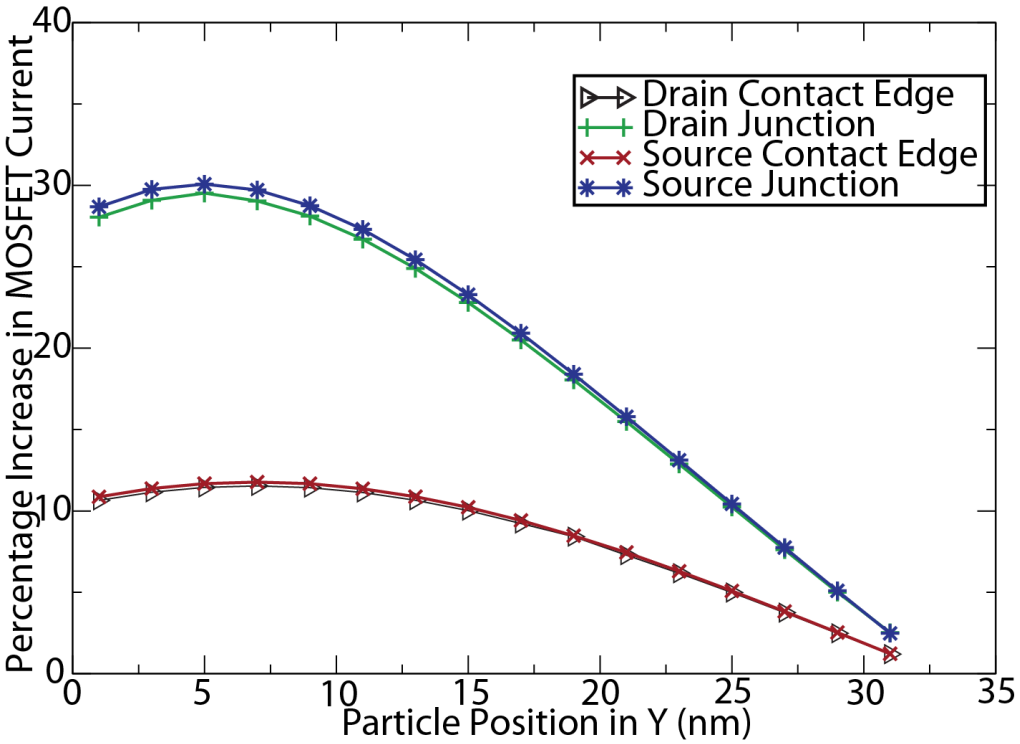

Figure 5.6 – Percentage change in current due to particles at various points above the source and drain. The results shown are for the low drain case. The effect decreases close to the gate dielectric, which is most likely to do with the proximity to the Dirichlet boundary.

The percentage increase in the drain current as a result of an ion in each position is shown in Figure 5.7. This shows that the maximum change occurs when the ion is off centre of the channel - slightly closer to the source than the drain – and close to the gate dielectric. This is because the peak of the potential barrier between the source and the drain shifts towards the source due to the bias applied to the drain contact. The diagram shows up to 350% increase in current due to the ion, but it must be noted that this device was modelled as 3 nm in depth and the effect would diminish in a manufactured device which would have a larger depth. The equipotential lines shown in the diagram are consistent with the effect of the Dirichlet boundaries on the ion-induced drain current increase. The overall result of these simulations shows that the effect of the single ion is significantly greater close to the centre of the channel. This result is essential moving forward to create a model of a nano-bio sensor.

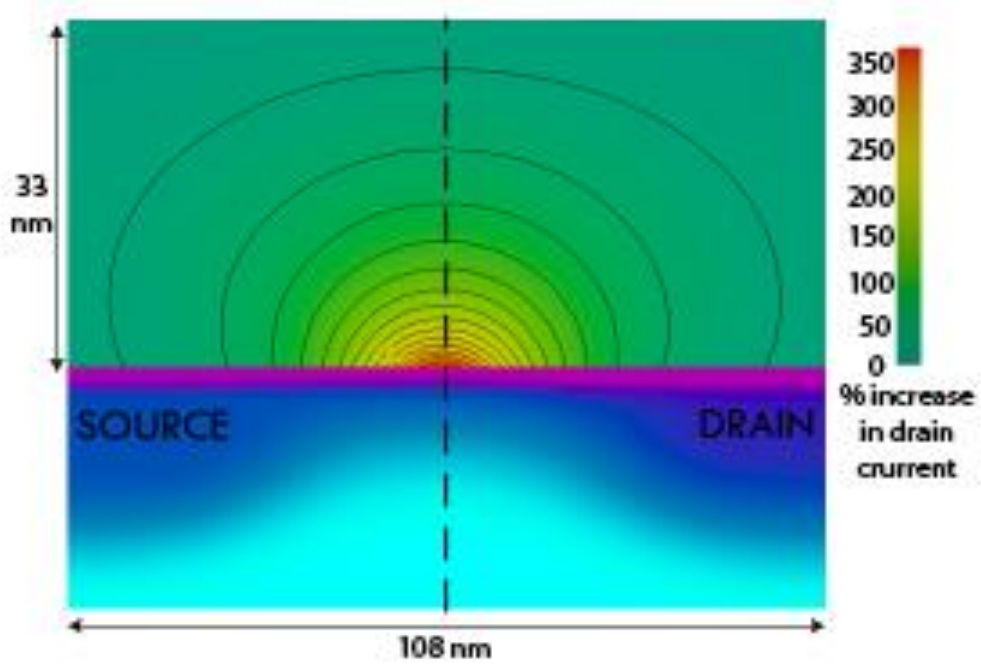

Figure 5.7 – Percentage change in drain current due to a single fixed positive particle. The oxide and source drain regions are shown for reference, as are equipotential lines. The dashed line indicates the centre of the device. The bending of the equipotential lines indicates the effect of the Dirichlet boundaries as noted previously.

5.4 Introducing a Nano-Pore

The introduction of a nano-pore into the simulation domain is essential to properly analyse realistic single ion sensing. These simulations are, once again, without background 'noise' from the Brownian motion of multiple ions. The first simulations investigate the effect of ion position on drain current, in the presence of a nano pore. The second set investigates the effect of the position of the nano-pore itself and compares this with the case where no channel is present at all. Finally the first set of simulations is repeated, varying the ionic concentrations above and below the lipid layer.

The first experiment was a simulation with a positive charge artificially moving through a pore. The simulation domain of the device, shown in Figure 5.8, was defined using the following parameters. The total dimensions were 108 × 110 × 30 nm. The *z* dimension is larger than in previous devices, and is to allow enough space for the nano-pore to be surrounded by the lipid layer and water region, and additionally means that the electric field due to the mirror charge is less than 0.03% of that at 0.5 nm. The grid meshing was non uniform in *x* and *y* directions (maximum 1 nm and minimum 0.5 nm spacing) to allow better resolution in the areas of interest (around the channel and in the aqueous region surrounding the nano-pore) while retaining numerical efficiency. A fine 0.5 nm uniform mesh is used throughout the *z* dimension. The doping in the device was as previously described, and the device dimensions were 108 × 75 × 30 nm, with a 2 nm layer of silicon oxynitride between 75 and 77 nm in the *y* dimension. The remaining material in the *y* dimension is an area of pure water, with a lipid layer between 92 and 95 nm. This has a 0.5 nm 'hole' at the centre (in *x* and *z*) of the layer which is modelled as pure water.

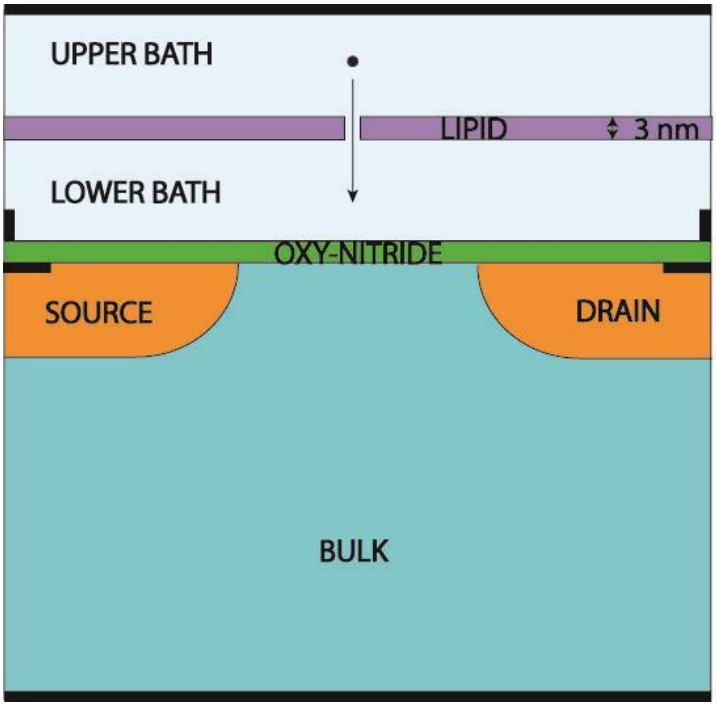

Figure 5.8 – Simulation structure used to investigate the effect of the movement of a single positive ion on the drain current of a FET. The structure is as previously described (see section 5.3 and Figure 5.5) but with the addition of a 3 nm lipid layer placed 15 nm above the oxynitride.

The applied gate bias was set to 0.7 V to ensure that the FET was working in the sub-threshold region, and the drain bias was 0.1 V. 'Source' and 'drain' boundaries in the aqueous area were pinned to the same potential as their equivalent in the FET.

The fixed positive ion was placed at the centre of the *x* and *y* dimensions of the device, just below the gate electrode and moved towards the oxide in 0.25 nm steps until 1 nm above the gate dielectric. Cloud in cell charge assignment was used to represent the charge, and simulation performed using drift diffusion in both the transistor and aqueous solutions domains. At this stage the Brownian

motion of the individual ions, and the corresponding noise, are neglected, treating the ionic solution as a continuous charge medium.

Figure 5.9 shows the FET drain current as a function of the ion position. There is a clear increase in drain current rate of change as the ion transverses the membrane. This is due to the spreading of the effect of the Coulomb potential caused by the small relative dielectric constant of the membrane ($\varepsilon_r = 2$) compared to the very large relative dielectric constant of the solution ($\varepsilon_r = 80$).

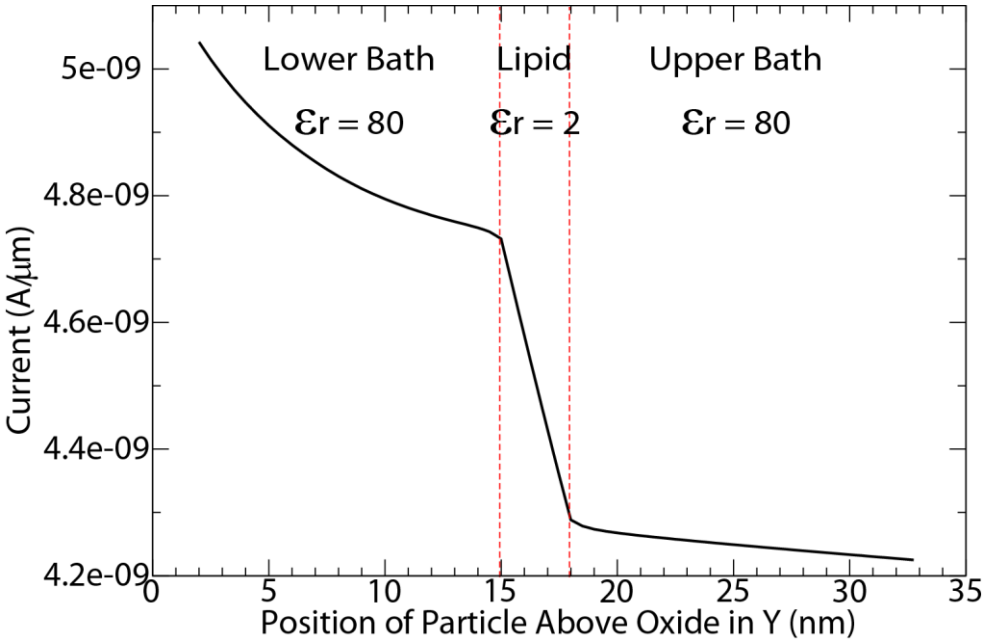

Figure 5.9 – Drain current trace when a particle is moved from the top of the simulation, through a nano-pore, towards the oxide of the FET.

Figure 5.10 shows the potential along a single line passing through the centre of the pore on a normal to the *x-y* plane in the aqueous region. This shows the effect of the Coulomb potential of the ion on the potential distribution which is magnified in the nano-pore – the electric field across the lipid layer is 25 times larger than the electric field in the water layers. Figure 5.11 shows the oxide-water interface potential for selected ion positions, with Figure 5.12 and Figure 5.13 allowing closer views of specific features around the channel and source junctions respectively. When the ion is close to the oxide, there is a distinct increase in potential above the channel and an equivalent reduction of the energy barrier between the source and the drain which leads to the increase in the drain current. The major effect occurs during the occupation and traversal of the nano-pore, since the increase in potential observable at this stage is notable throughout the interface, including the region above the source junction.

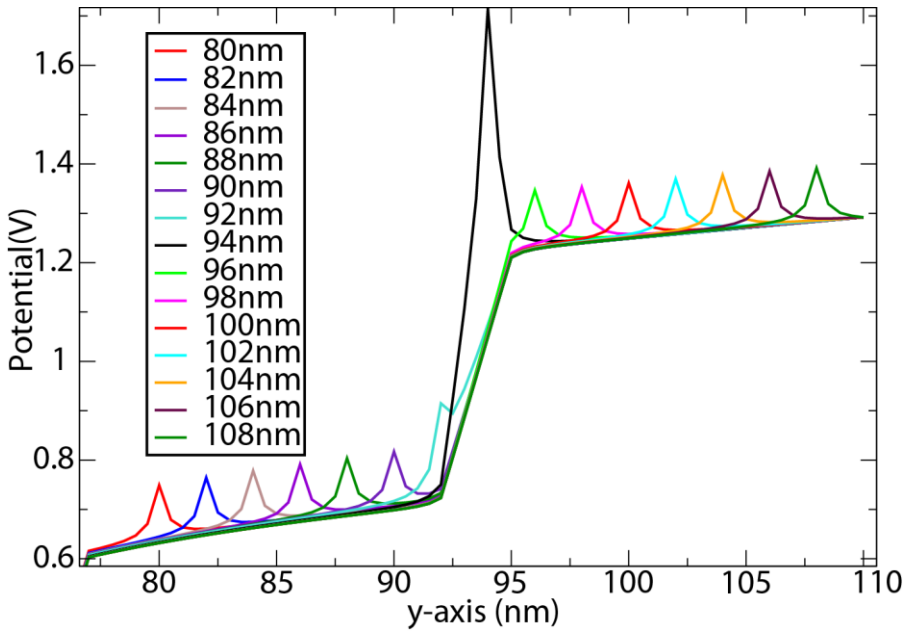

Figure 5.10 – Potential profile in the aqueous area when a single positive ion is placed at various points, including at the centre of the nano pore which is between 92 nm and 95 nm.

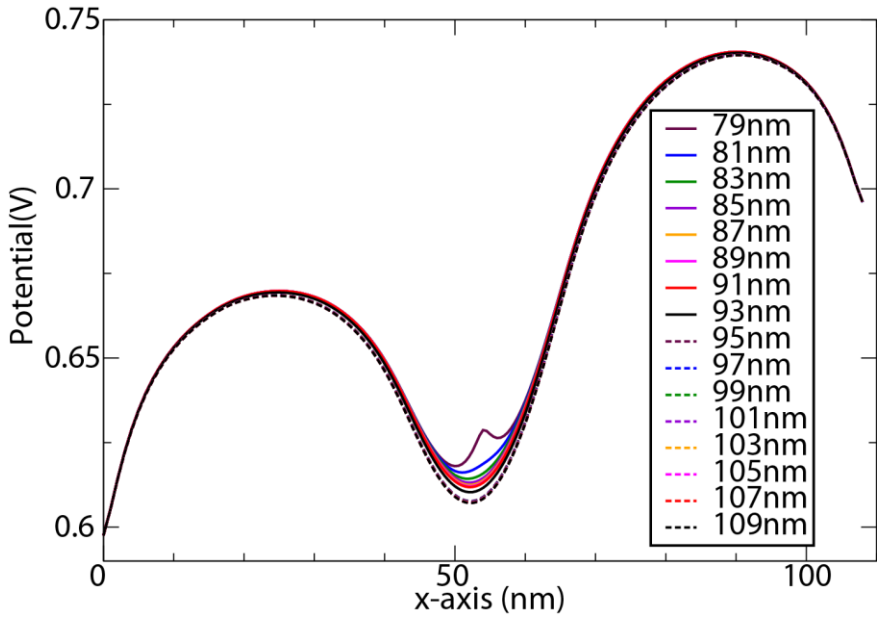

Figure 5.11 – Potential at the water-oxide interface as a result of various positions of positive ion. The dashed black line is when the ion occupies the nano-pore, and all other solid lines are when the ion is 'underneath' the nano-pore.

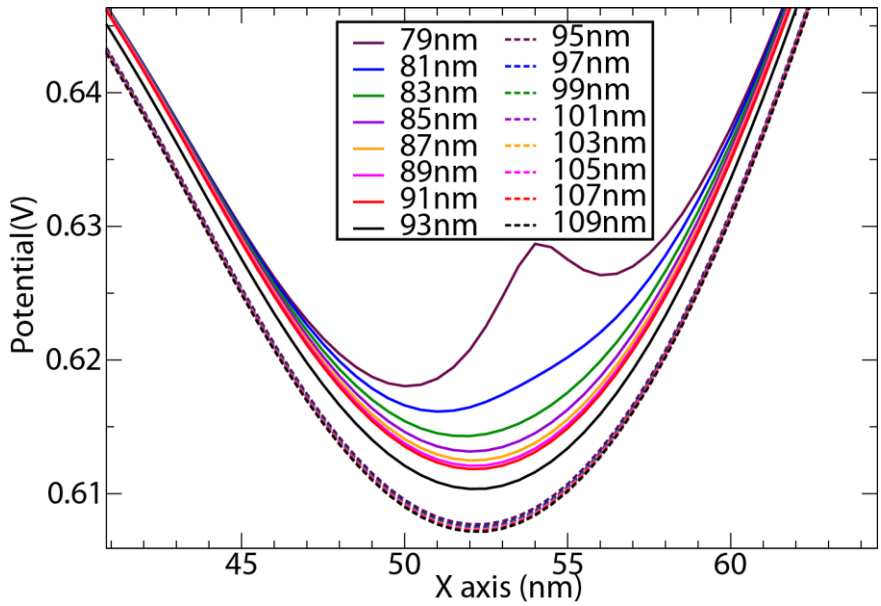

Figure 5.12 – Closer version of Figure 5.11 focussing on the region above the FET channel. This further indicates the rapid change between the dashed lines – denoting when the ion is above the nano-pore, and the solid lines which are either occupying the nano-pore or below it.

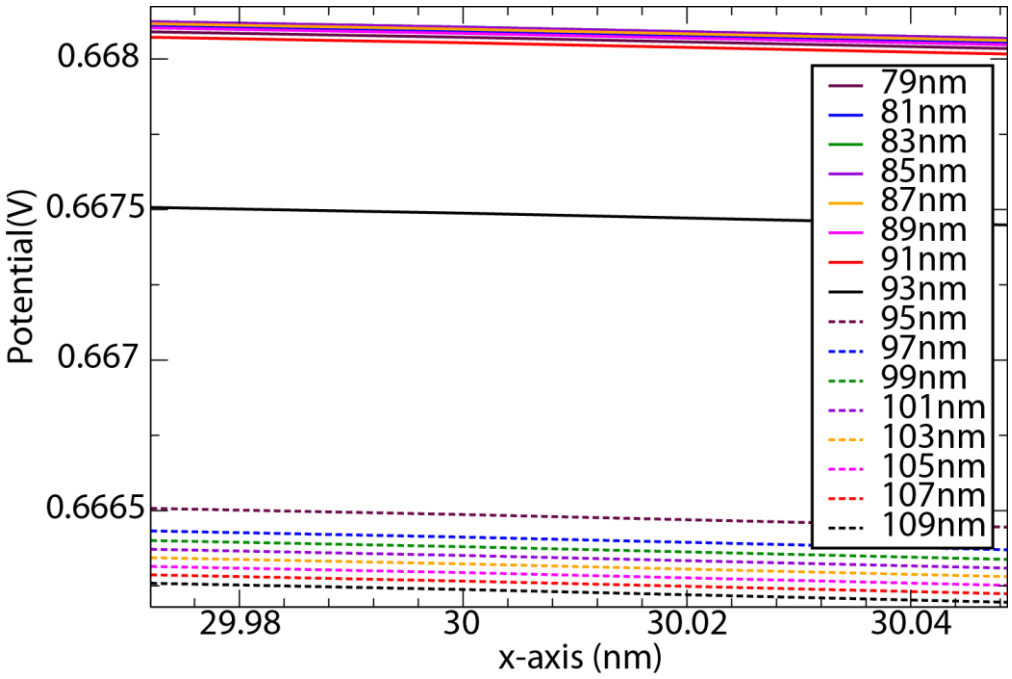

Figure 5.13 – Closer version of Figure 5.11 showing a close view of the region above the FET source junction.

The low dielectric constant of the lipid membrane results in the spreading of the effect of the Coulomb potential of the permeating ion over most of the gate region of the transitory and is illustrated in Figure 5.14. This shows the significant change of the surface potential when the ion resides within the membrane. It is evident that there is a large change in potential above the source and drain regions as the ion goes through the nano-pore in the lipid layer which directly affects the drain current. This is further illustrated in Figure 5.15, which maps the water-oxide interface potential change across the transistor for the three most important ion locations. While the potential change is greatest in the channel as the ion moves from 80 nm to 79 nm (adjacent to the channel itself), this effect is highly localised. Instead, the greatest overall change occurs as the particle traverses the

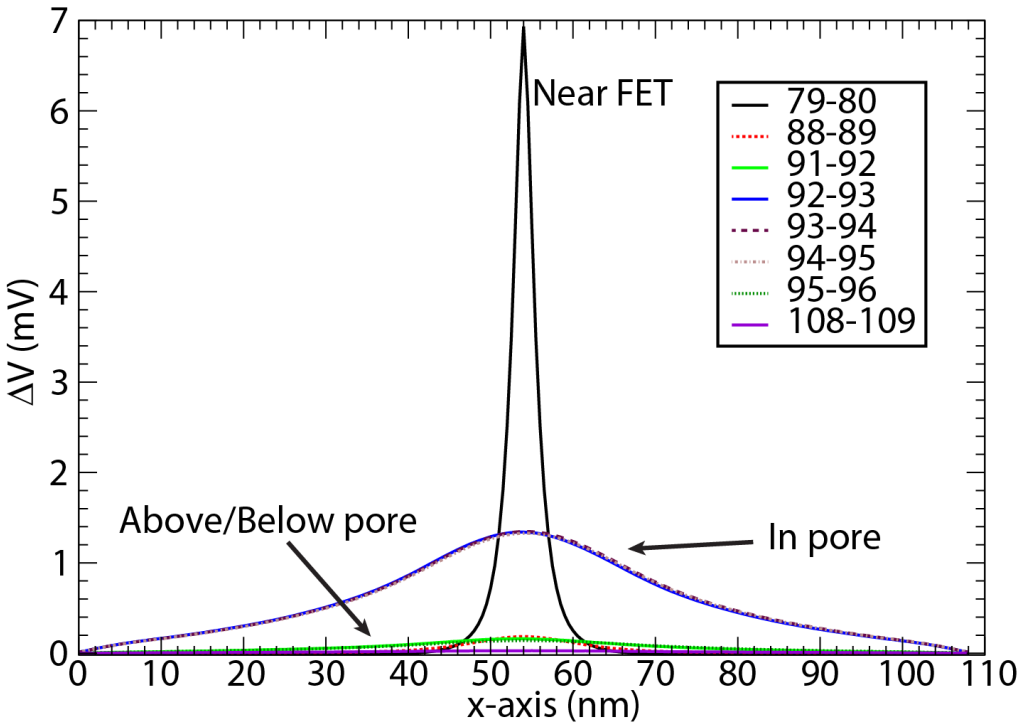

Figure 5.14 – Difference in interface potentials when the particle is moved by 1 nm.

pore. This is due to significant 'defocusing' of the Coulomb potential causing a significant rise in interface potential throughout the channel.

Simulations were then performed with an altered lipid layer/channel distance, again using the drift-diffusion approximation in both the transistor and aqueous solution, thus treating the solution as a continuous medium. Simulations were performed with the lipid layer situated at 5, 10, 15, 20 and 25 nm above the oxynitride surface. The lipid layer thickness, dielectric constant and pore size were unaltered. The FET drain current was measured in response to the motion of a single positive ion, successively repositioned from the top electrode through the nano-pore towards the oxynitride.

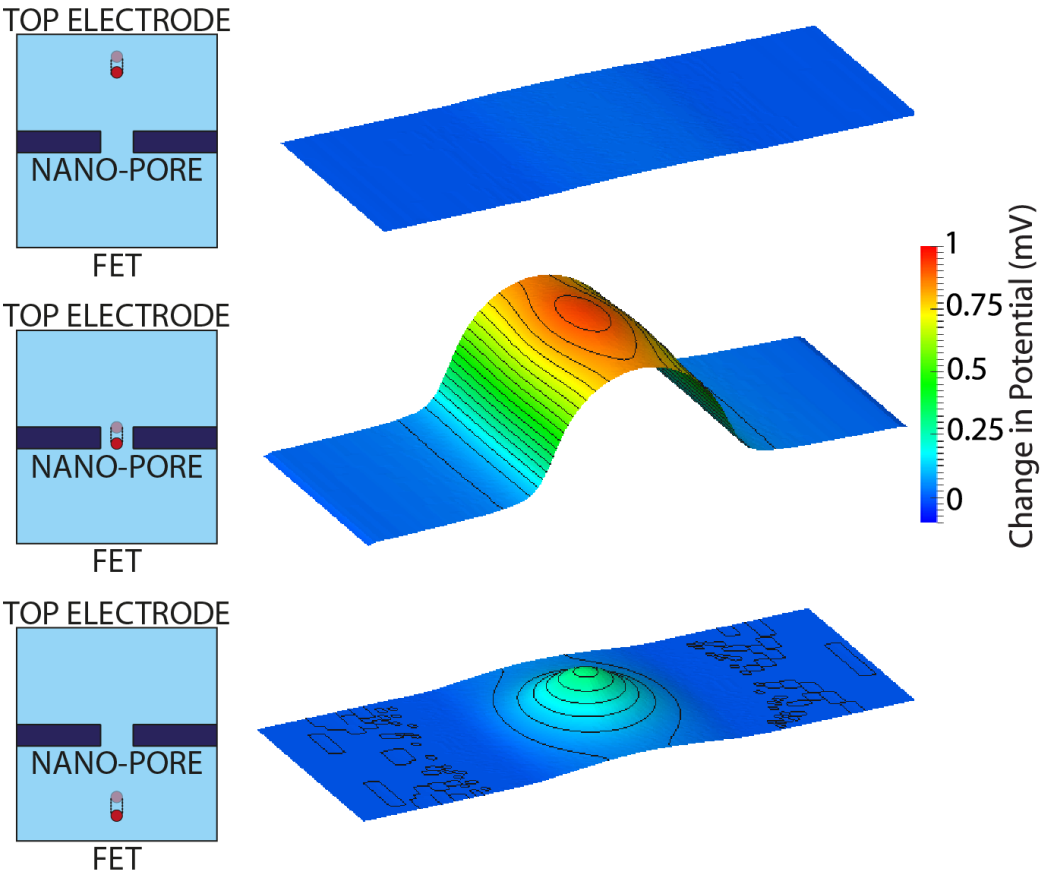

Figure 5.15 – Change in silicon interface potential (mV) as an ion is moved 1 nm towards the oxide of the FET. The top plane shows the change when the ion is in the top bath. The middle plane shows the change as the ion moves through the pore. The lower image shows the change when the ion is close to the oxide.

The currents obtained from the simulations with 5 different positions of the lipid layer above the gate dielectric are compared to the case where no lipid layer is present in Figure 5.16a and 5.16b. shows the same results without the comparison to the simulation with no lipid layer. As in the previous results, there is a clear increase in the sensitivity of the drain current in each case as the ion traverses the membrane. This is due to the delocalisation of the Coulomb potential by the small relative dielectric constant of the membrane ($\varepsilon_r = 2$) compared to the very large relative dielectric constant of the solution ($\varepsilon_r = 80$). This results in the same 'defocussing' of the Coulomb potential of the permeating ion over a larger area of the gate region of the transistor which causes a larger relative change in the drain current, as illustrated in Figure 5.15. There is a significant change of the surface potential (and the current) of the transistor when the ion resides within the membrane which, somewhat counter intuitively, results in less change when the ion is close to the interface.

As expected, the closer the lipid layer to the gate dielectric, the lower the drain current; the lipid layer position determines the overall current level in each case. This is because the potential drop across the membrane is much greater than in water – if this occurs further away from the channel, the effective surface potential will remain higher. The lipid position affects the sensitivity when an ion traverses the pore. Furthermore, in Figure 5.16 it is shown that the rate of change of current through the pore is directly affected by the pore position. This suggests that there is an optimal positioning of the lipid layer to achieve the greatest sensitivity of the drain current to the ion traversing the pore. According to these results, when the pore is between 10 nm and 20 nm above the oxynitride, the strongest sensitivity is achieved as the current increases by more than 0.4 nA/μm. Outside this range, the increase in current is lower. This suggests that the pore should be placed far enough from the oxynitride to avoid

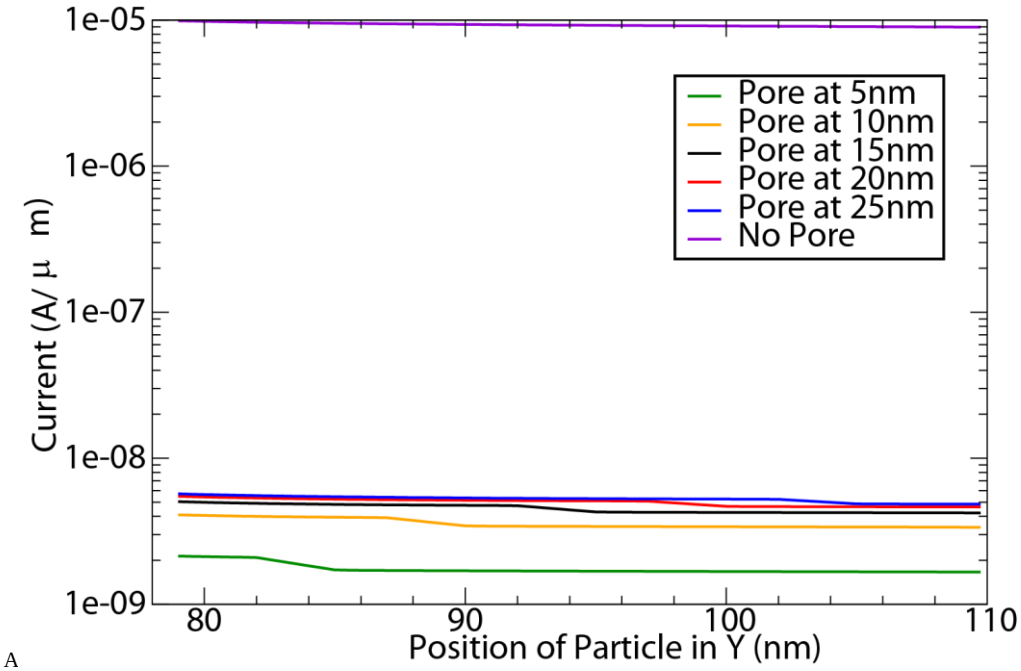

A

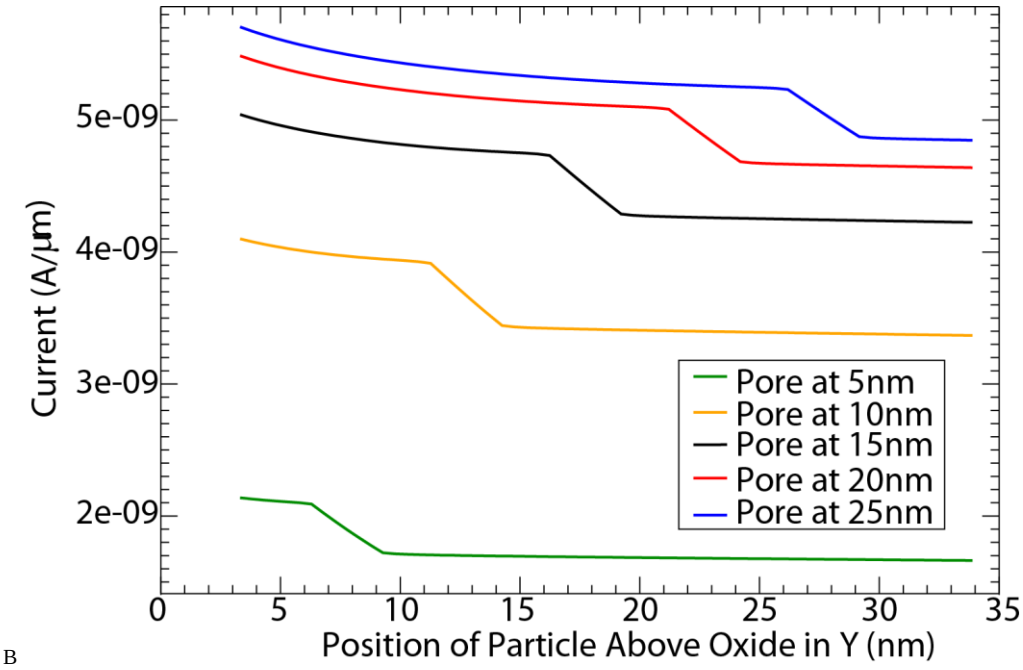

B

Figure 5.16 – Dependence of drain current on pore position. Shown with (A) and without (B) the instance with no pore present. The closer the pore is to the oxide, the lower the current is in the FET.

screening effects of contacts, but close enough that the device remains in the sub-threshold regime.

5.5 Conclusion

This chapter detailed the initial experiments using the newly developed simulation software. Investigations were performed to examine the effect of individual ions on drain current in nominal 35 nm channel length FET. All tests were performed treating the aqueous solution above the FET as a continuous media with a charge density resulting from an artificially placed ion and the simulations were completed using the drift diffusion approximation. It was found that the greatest effect on absolute current occurs when an ion is close to the gate dielectric, and that the effect is greatest slightly closer to the source than the drain, when drain bias is applied.

Additionally, the effect of introducing a nano-pore in a lipid layer suspended in the aqueous solution was investigated. It was found that the greatest change in current during traversal of the nanopore occurs when the lipid layer is placed between 10 and 20 nm above the oxynitride. It was found that the lipid layer causes a ‘defocussing’ effect on the Coulomb potential resulting in an increased surface potential and sensitivity. This means that experimental tests should aim to place the lipid layer at this level to allow the best chance of successful identification pore traversal.

This simulation methodology is a considerable improvement in the state of the art [21] which required the modification of commercial software to analyse a similar system using only drift diffusion.

Chapter 6

Dynamic Simulations

6.1 Introduction

This chapter describes the results of simulations performed using the newly developed simulator integrating Brownian dynamics and drift diffusion domains in the same simulation harness. For the first time the effects of stochastic ionic movement in an electrolyte on FET drain current are investigated. Simulations are performed which allow the evaluation of shot noise induced by a bath of ions in an aqueous solution above the gate of a sensing FET. Finally, the sensing of the

permeation of a single ion through a nanopore, in the presence of background noise, is evaluated.

6.2 Dynamic Simulations – Ion Bath

The first ionic simulations revisited the simulations presented in section 5.2 considering a FET with its gate electrode replaced by an ion bath and remote contact. In section 5.2 the simulations were carried out using the drift-diffusion approximation in both the FET body and ion bath. The simulation domain is shown inset in Figure 5.3. The domain is 108 × 110 × 3 nm, with 75 nm of silicon forming the body of the FET, a 2 nm layer of oxynitride and then 33 nm of electrolyte solution with a gate electrode above. For this simulation, the device has a peak source and drain N^+ doping concentration of $1 \times 10^{20}\,cm^{-3}$ and P type doping of $5 \times 10^{18}\,cm^{-3}$ throughout the substrate. The doping profile is approximated using 2D Gaussian distributions in *x* and *y*. The effective channel length of the transistor (the distance between the metallurgical p-n Junctions at the interface) is approximately 35 nm. A 2 nm layer of silicon oxy-nitride is placed between the FET and a 33 nm layer of electrolyte solution, chosen to allow a large enough region for later experiments where a lipid membrane will be added. The electrolyte solution was modelled as a charge neutral region with a $6.022 \times 10^{26}\,m^{-3}$ concentration of both sodium and chloride ions. An Ohmic contact is applied across the top of the electrolyte to act as an electrode. 0.2 V is applied across the top electrode to bias the FET in the sub-threshold region, the bias on the drain was 0.1 V and there was a 0 V bias on the source.

A full drift-diffusion approximation solution over the whole simulation domain was used as starting conditions, allowing for the initialisation of the Brownian

particles in the ion bath. The Brownian simulation approach was then initiated in the Brownian region using 1 ps time-steps, performing a linear solution of the Poisson equation after each time-step in the whole simulation domain. A full drift-diffusion solution in the transistor was performed every 100 time-steps (0.1 ns) at which time the FET drain current was calculated. This 1:100 ratio of full solutions to Brownian only solutions was chosen through testing on individual cores of 2.53 GHz Intel Xeon Nehalem processors with up to 6 GB of memory per core. An increase in the frequency of the full solution resulted in a significantly increased computational overhead, with the 1:100 taking approximately seven days to complete 1 million time steps. The ratio chosen ensured that a full solution is performed frequently enough during a normal ion-pore traversal time which is in the order of tens of nanoseconds.

The potential distribution for a single full drift diffusion iteration is shown in Figure 6.1. While the device is the same as that in Figure 5.4, the difference in simulation methodology allows the simulation of ions as individual discrete charges and the corresponding noise. Figure 6.2 shows the drain current of the FET over the first 6 ns of the simulation. This shows the transient of the beginning, when settlement of the simulation domain is still progressing. The drift diffusion steady state simulation current for this gate bias is shown for reference. It can be seen that, after the initial relaxation, the current from the combined Brownian and drift diffusion simulation fluctuates around an average which is close to the current obtained in the drift diffusion simulation. The mean of the combined simulation is 5×10^{-7} A/μm compared to 4×10^{-7} A/μm for the drift diffusion only, representing a close match deep in the subthreshold regime.

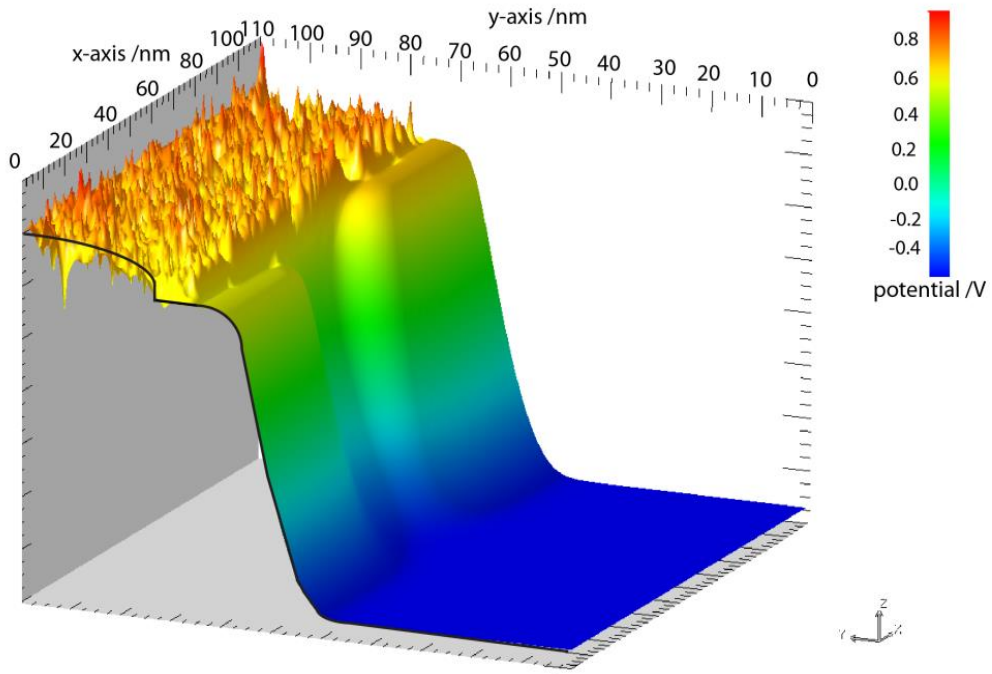

Figure 6.1 – 3D potential plot of a FET with an electrolyte solution above the oxide, and with Brownian particles introduced. This plot is taken at a single time step with no averaging. The black line shown at x = 0 nm indicates the approximate results achieved with a drift diffusion only simulation.

The current when using Brownian dynamics varies around the steady state current simulated using drift diffusion only. Three points are highlighted on the time series trace in Figure 6.2 and the silicon-oxide interface potential is shown for each of these points in Figure 6.3. These show high, moderate and low current points on the series. This result clearly demonstrates that the fluctuations in the distribution of charge in the ionic solution is having a direct effect on the potential in the channel, leading to a corresponding change in the electron concentration at the interface, and a change in the transistor drain current. Taking approximate measurements for the difference peak channel potential at each highlighted time-

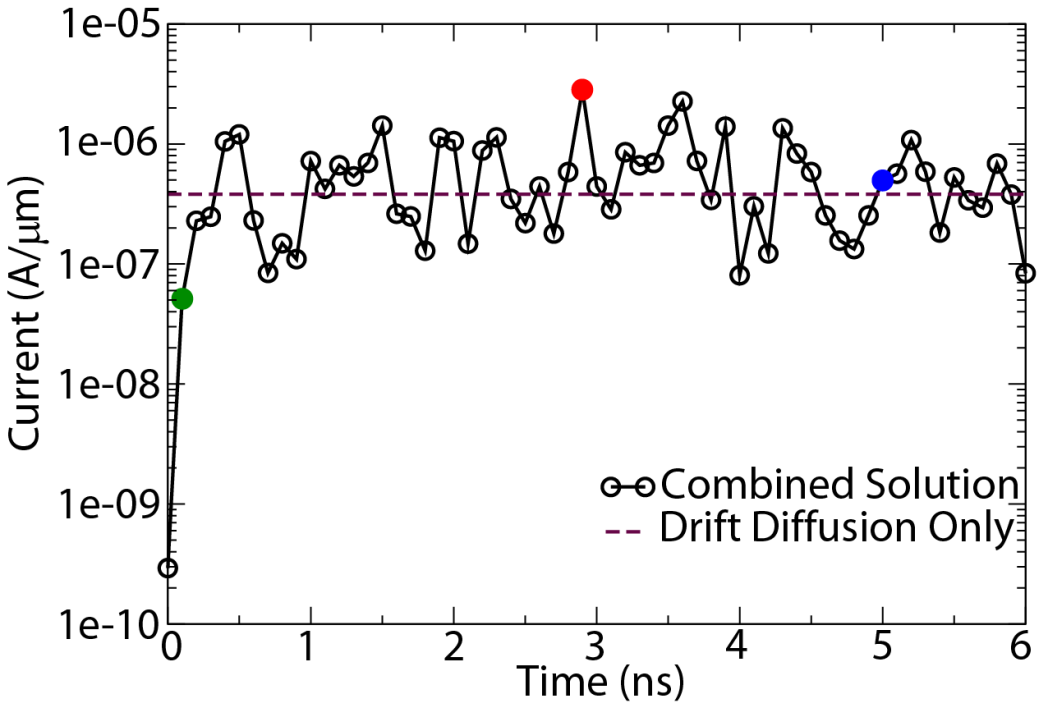

Figure 6.2 – Drain current in the FET with 0.2V gate electrode bias simulated with Drift Diffusion only and with Brownian dynamics combined with Drift Diffusion.

step in in Figure 6.2 suggests a transconductance (the change in current per unit change in potential difference) on the order of 3×10^{-6} A/µm/V, though, as would be expected as the FET is operating in the subthreshold region, the sensitivity increases as the surface potential increases. This simulation shows the high sensitivity of the transistor characteristics to local potential fluctuations directly resulting from the movement of ions in the solution.

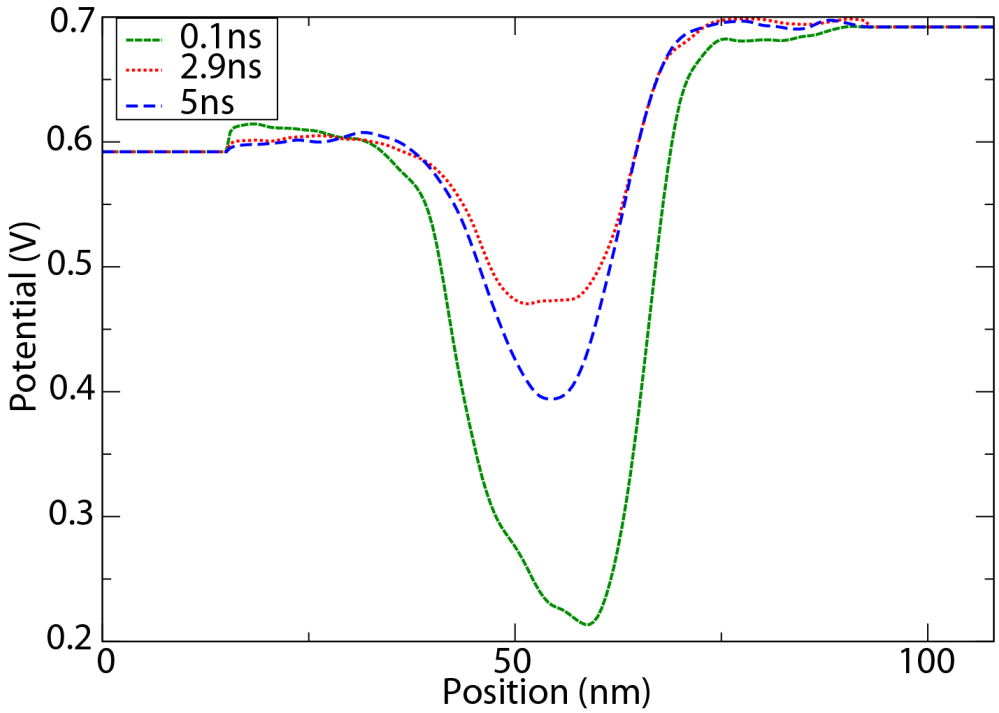

Figure 6.3 – Oxide-Silicon interface potential at three time-steps. These times match to those highlighted in Figure 6.2.

6.3 Noise Analysis

The next stage is to analyse the effects of shot noise associated with individual discrete ions in the electrolyte on the drain current of the n-channel FET. Nanometre thick insulator layers are routinely used in silicon MOSFETs, allowing tight electrostatic control of the flow of carriers through their channels, making modern MOSFET devices highly sensitive to individual discrete charges [115]. Indeed large (more than 100%) 'random telegraph' changes in the current flowing through nano CMOS transistors are routinely observed as a result of single carrier

trapping in gate oxides [118]. This effect has been posited as a method of single carrier sensing [119] in a possible MOSFET based bio-nano-sensor. However, background 'noise' of the Brownian motion of the solution may interfere with the resolution of individual ion permeation, and should be investigated.

The device structure, ion and doping concentrations, and simulation initialisation is identical to the simulations in the previous section. Brownian particles were introduced to the electrolyte as sodium and chloride ions at a concentration of $6.022 \times 10^{26}\ m^{-3}$. The starting point of such simulations is a drift-diffusion solution in both the FET and the electrolyte region. This gives a more realistic potential distribution before the introduction of the Brownian particles. The simulation was then performed with a fully self-consistent solution to the whole domain for each 1 ps time-step, using the Brownian dynamics system to move the ions, and a cloud-in-cell arrangement to assign charge to the mesh. The small time steps of the full solution allow the extraction of the high frequency component of the noise spectrum. The length of the simulation determines the lower frequencies that can be captured in the noise analysis.

The power spectrum of the current in the electrolyte solution is shown in Figure 6.4. The analysis uses data from multiple simulations totalling over 40,000,000 time-steps (40 μs) with data recorded every 100 ps. This power spectrum tends towards 'white noise' as expected as the result for Brownian noise. With a longer simulation time, the power spectrum would be expected to produce an even more uniform distribution at all frequencies.

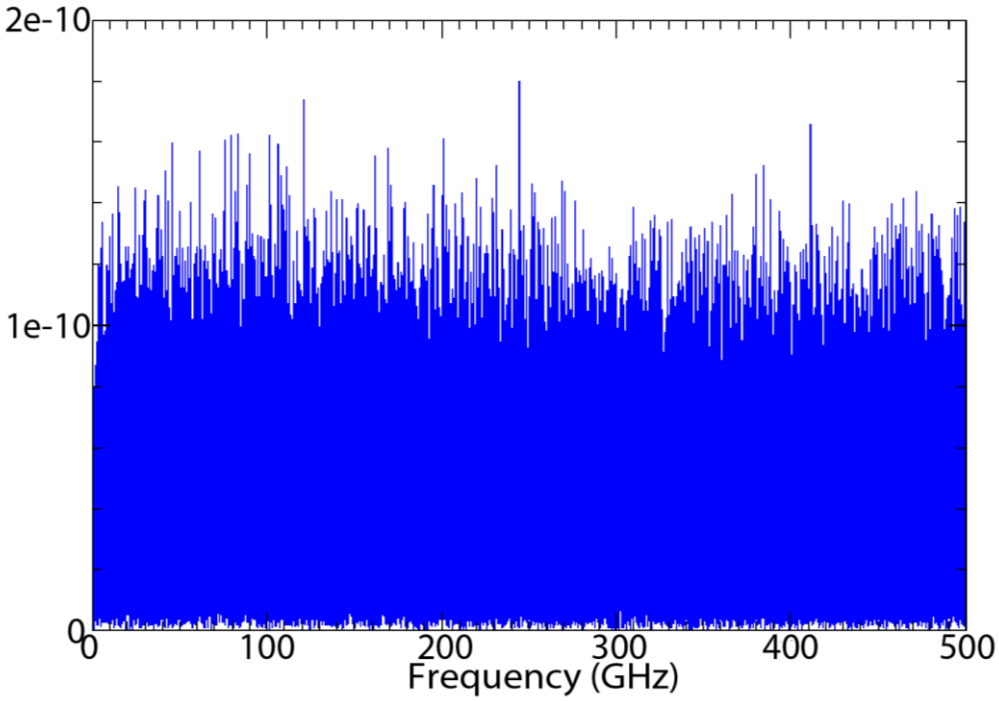

Figure 6.4 – Discrete Fourier transform of the current in the aqueous solution at 1ps time-steps.

Figure 6.5 shows the power spectrum of the FET drain current in the presence of Brownian noise from the electrolyte solution. It can be seen that the sensitivity of the MOSFET drops sharply at around 3 GHz, below 3 GHz the FET responds to fluctuations in the electrolyte solution. The response in the simulations is dependent on transport models which are less accurate than the electrostatics. Since the duration of an ion permeation event in an ion channel occurs on the order of 10s of nanoseconds this is an order of magnitude below the cut-off frequency of the MOSFET sensitivity.

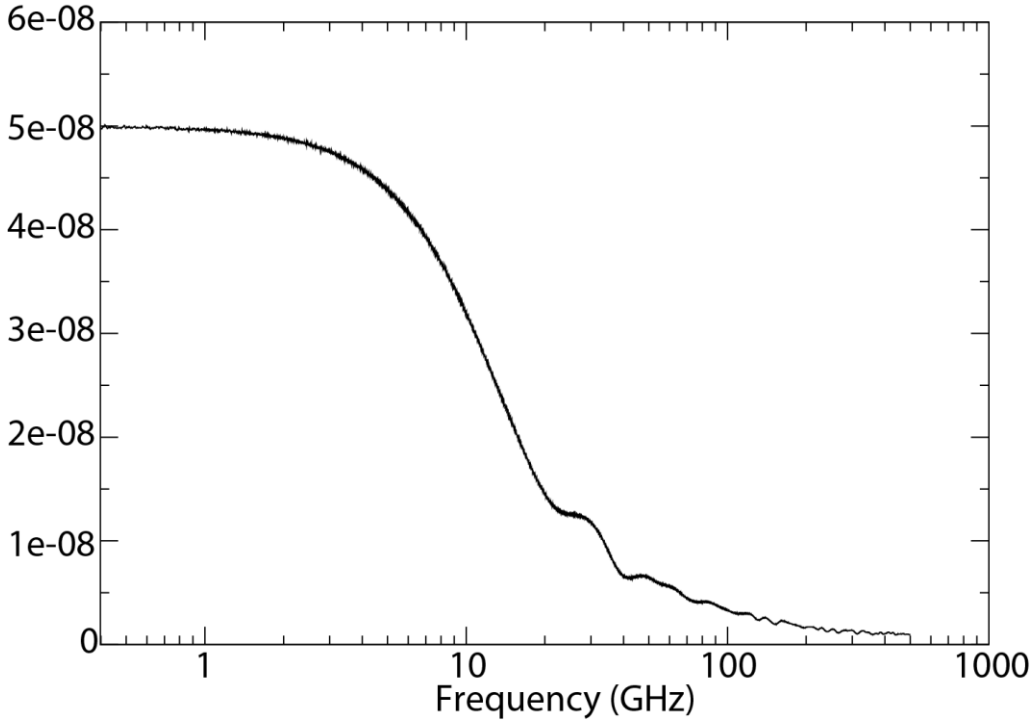

Figure 6.5 – Power distribution in the FET drain current. The response begins to drop at approximately 3GHz. Below this the current is reacting almost instantaneously to fluctuations in the electrolyte solution.

6.4 Forced Ion Traversal Simulations

Next, simulations were conducted with the addition of a 3 nm lipid membrane layer 15 nm above the oxide. The simulations are carried out with biologically significant concentrations of background ions in the solution simulated as Brownian particles which move stochastically. A 0.5 nm nano-pore modelled as a hole in the membrane filled with pure water was placed at the centre of the lipid layer. A single positive ion was then positioned at the top of the pore and moved from the gate electrode towards the oxide, through the nano-pore. Chloride and Sodium ions were introduced into the simulations in equal concentrations to

provide an average charge of zero, and are moved thermally to introduce noise in the transistor current. The electrolyte solutions above and below the lipid layer were set at 0, 1 mM and 1 M respectively, chosen to demonstrate a range of biologically significant concentrations [120], of each species to create the combinations listed in Table 6.1. In extracellular fluid, for example, the concentration of sodium, potassium and chloride is between 10 and 400 mM.

Each simulation was performed with a 1 ps time step and 500 time steps were completed to allow the system to equilibrate before the test ion was allowed to move through the pore. It was found that 500 time steps allowed the charge density in the simulation to equilibrate, for any of the experimental molar concentrations. In order to capture the detail of the simulation at the same rate of the simulations in section 5.4, a full drift diffusion solution as performed after every time step.

Simulation Number	**Upper Bath (Lipid to Top Electrode)**	**Lower Bath (Oxide to Lipid)**
1	1 M	1 M
2	1 M	1 mM
3	1 M	0
4	1 mM	1 M
5	1 mM	1 mM
6	1 mM	0
7	0	1 M
8	0	1 mM
9	0	0

Table 6.1 - Electrolyte concentrations in the 9 simulations performed where a single positive ion was forced through a nano pore.

The single ion which is moved though the nano-pore was held static at the top of the domain throughout the equilibration period as it was judged that introducing it after this period could cause some transient changes as a particle appears in the centre of the simulation from nowhere, defeating the purpose of the equilibration time. The current in the FET was calculated at each time step.

In order to achieve semi-realistic ion movement, the average magnitude of particle movements from the simulations in section 6.3 was taken resulting in 0.35 nm movements every 1 ps time-step from the top electrode through the pore to the oxide layer. Cloud in cell was used to represent the charge, and drift diffusion was then solved.

The results varied depending on the concentrations in the electrolyte baths above and below the lipid membrane. It was observed that, when the lower bath concentration is 1 M, no observable difference in drain current was registered during the permeation, clearly due to the dynamic screening from the ions below the membrane which occurs at distances in the range of 10 nm. Figure 6.6 shows the output of simulations 1, 4 and 7 where the lower bath concentration was 1 M. The ion enters the nano pore at approximately 0.54 ns, but the trace does not allow identification of that stage. Since simulations in the previous chapter showed that the rate of the change during traversal is higher than those at other times in the simulation, the rate of change of current is shown in Figure 6.7, but again, no observable difference is shown.

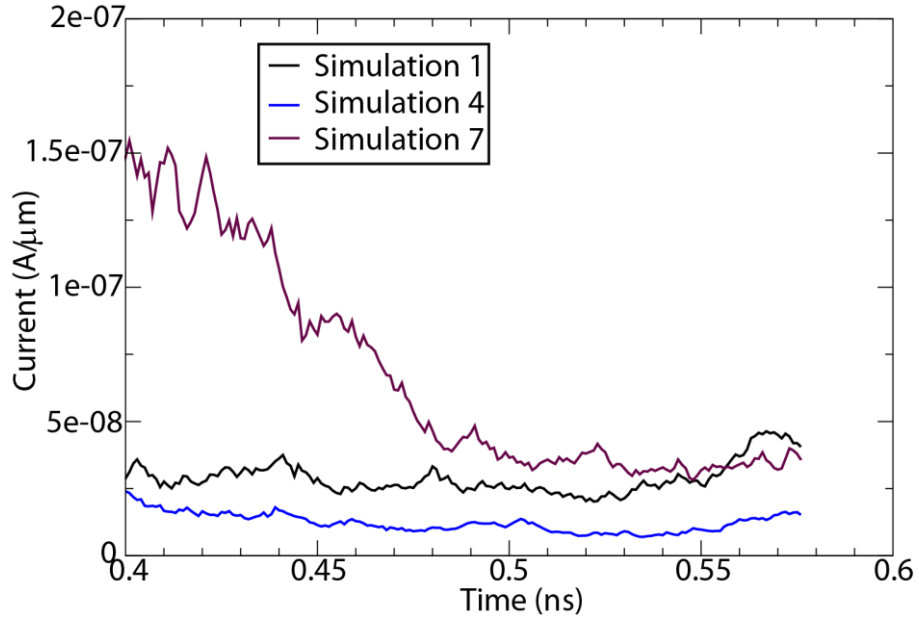

Figure 6.6 – Current trace when a single positive ion is moved through the electrolyte bath, through the nano pore and towards the oxide layer. The lower bath concentration is 1M in each simulation, the upper bath concentration is 1 M, 1 mM and 0 in simulation 1, 4 and 7 respectively. The pore traversal begins at approximately 0.54 nanoseconds.

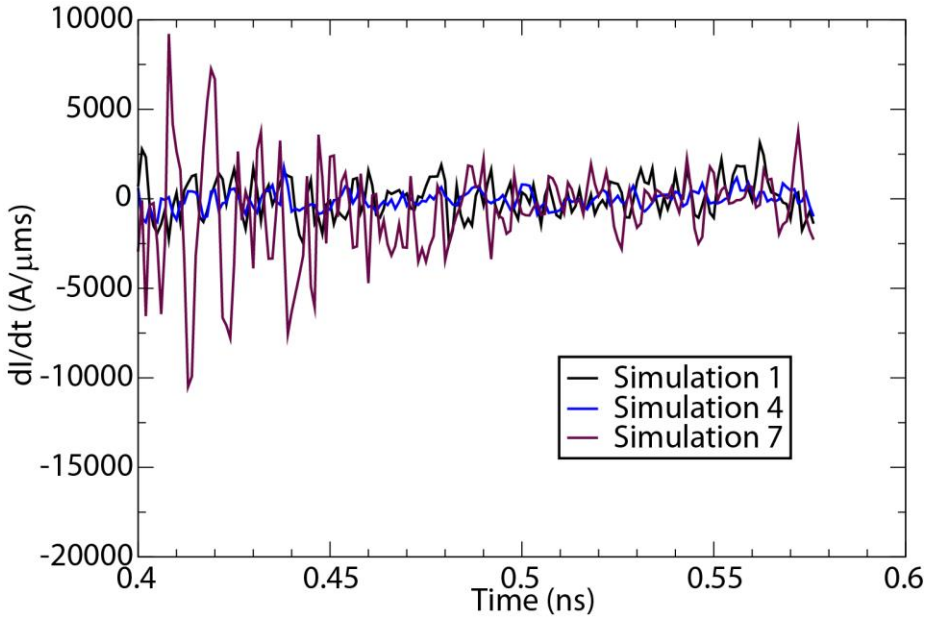

Figure 6.7 – Rate of change of current for simulations where there is a 1 M concentration below the lipid.

In the cases where the lower concentration was 1 mM of each species of ion, the traversal event results in current increase through the transistor. Figure 6.8 shows all three of these simulations. The point at which the particle traverses the pore can be seen as the ramp at approximately 0.54 ns. The level of noise was greater in the case where 1 M of each species was present above the lipid, but the screening effects were not sufficient to mask the permeation of the single positive ion.

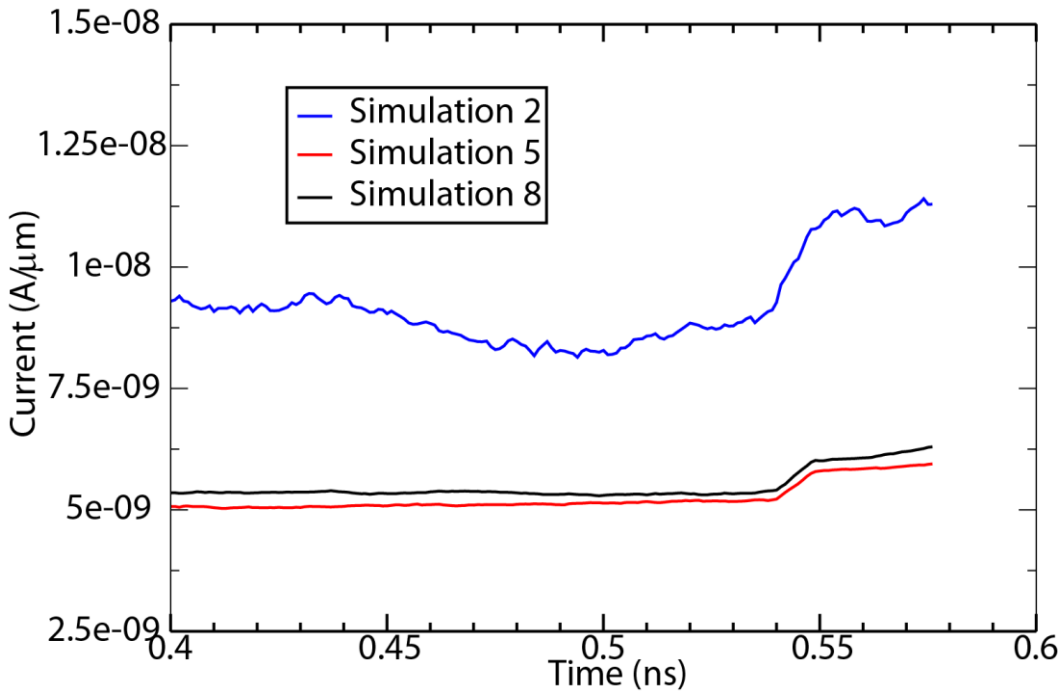

Figure 6.8 – Current traces for three of the simulation runs, in each case the lower concentration of each species of ion was 1 mM. The pore traversal can be seen at approximately 0.54 ns. Simulations 2, 5 and 8 had an upper concentration of 1 M, 1 mM and 0 M respectively.

While there is an evident change in current, when the traversal occurs it is difficult to separate this from the noise signals, since the level of the current does not drop after permeation. For this reason, the rate of change of current is used as the identifying feature.

Figure 6.9 shows the rate of change of drain current for a time period which includes the permeation. The rate of change of current during the traversal event is approximately two and a half times greater than during the rest of the simulation. Furthermore, a low pass filter averaging of the current time series produces a clearer signature of the permeation. Figure 6.10 shows a running average taken over 10 time-steps (10 ps). This time represents an approximation of the traversal event allowing smoothing of the noise surrounding the signal while preserving the signal itself. The data have been normalised to one, to provide a clearer comparison between the traces. The rate of change is never more than 30% of the peak traversal rate of change during the rest of the simulation, allowing clear discrimination between the traversal event and the rest of the simulation. Sensing circuitry could be allied with this to observe the rate of change of current and, as the signal is much larger during traversal, it would be possible to use a scheme of digital sampling to ensure that the traversal is sensed without the noise signal.

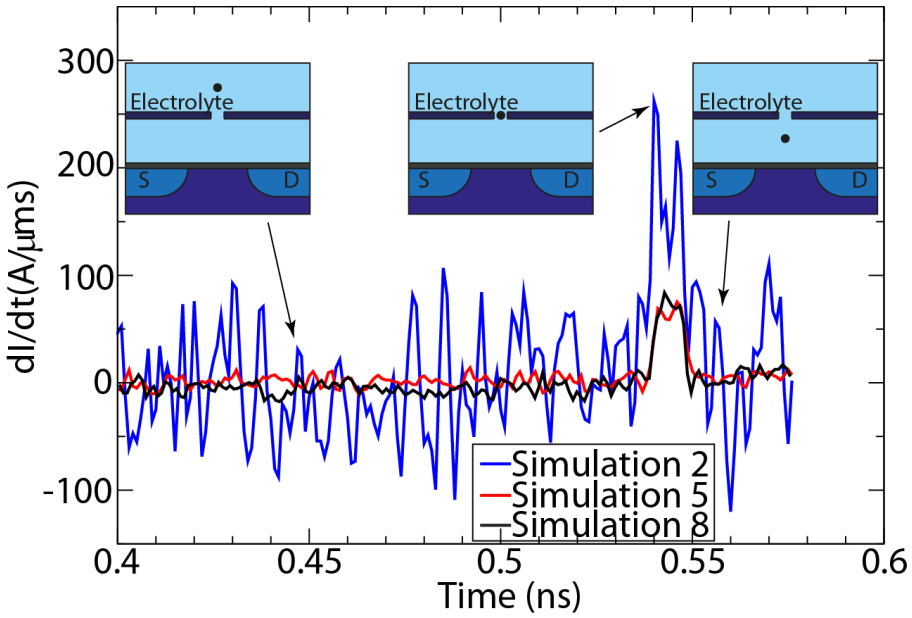

Figure 6.9 – Rate of change of drain current over time. The legend details the concentrations of ions above and below the lipid layer, referring to Table 6.1.

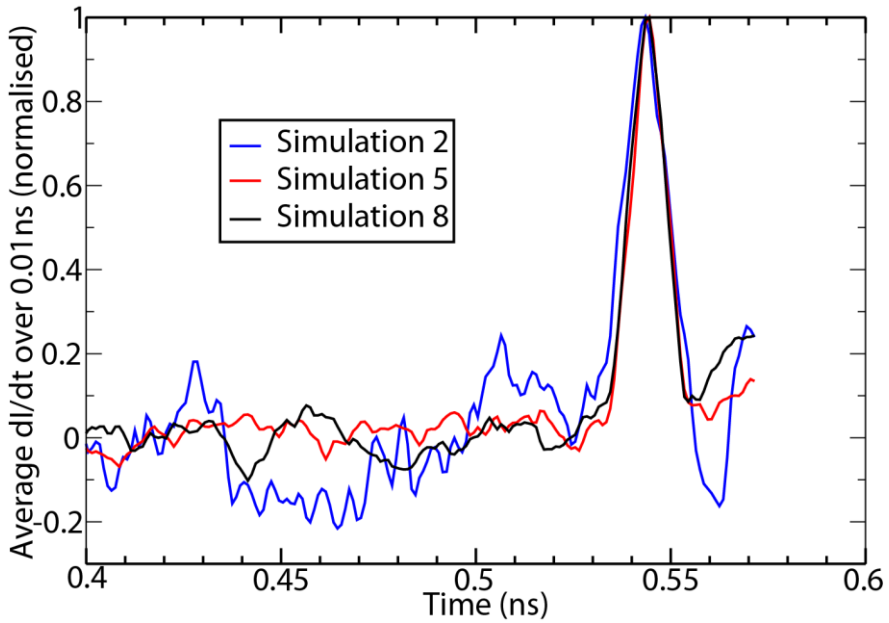

Figure 6.10 – Running average over 10 time steps of the same runs as shown in Figure 6.9. The plot is normalised.

The simulation traces for 0 lower bath concentration are shown in Figure 6.11. Some noise is visible in these traces, but there is little degradation as a result of the increased upper bath concentrations. The current rate of change plot which shows the clear distinction at the point of traversal is shown in Figure 6.12. In this case, when the upper bath concentration is 1 M, the rate of change is approximately double the maximum elsewhere, though if the trace were to be averaged the discrimination would be clearer. In the 1 mM case the rate of change is 40 times greater during the traversal than at other periods. However, although these simulations give a best case scenario, they are less realistic than those with non-zero background concentrations, since it is unrealistic to have a bath free of all ions. Note that simulation 9, and this case was discussed in the previous chapter.

Ion screening is the prime reason that the pore traversal signal is not detectable in simulations where there is 1 M of ions in the lower bath. As shown above, the upper bath concentration does have an effect on the pore traversal signal to noise ratio, but does not critically affect the ability to detect the pore traversal in these experimentally realistic conditions.

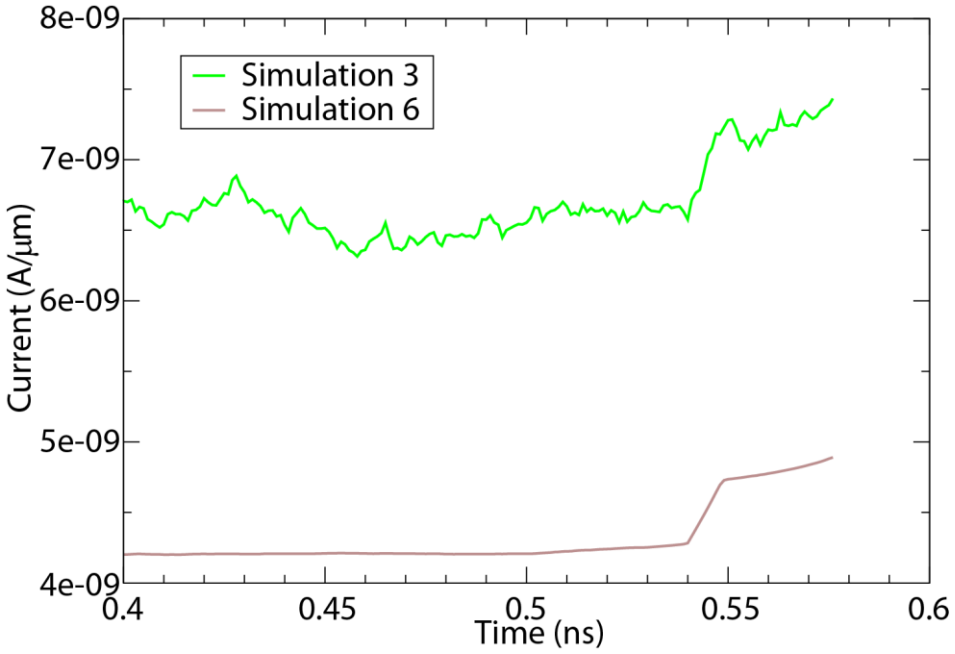

Figure 6.11 – Current in simulations where the lower bath is 0. Simulation three has an upper concentration of 1 M and simulation six has an upper concentration of 1 mM.

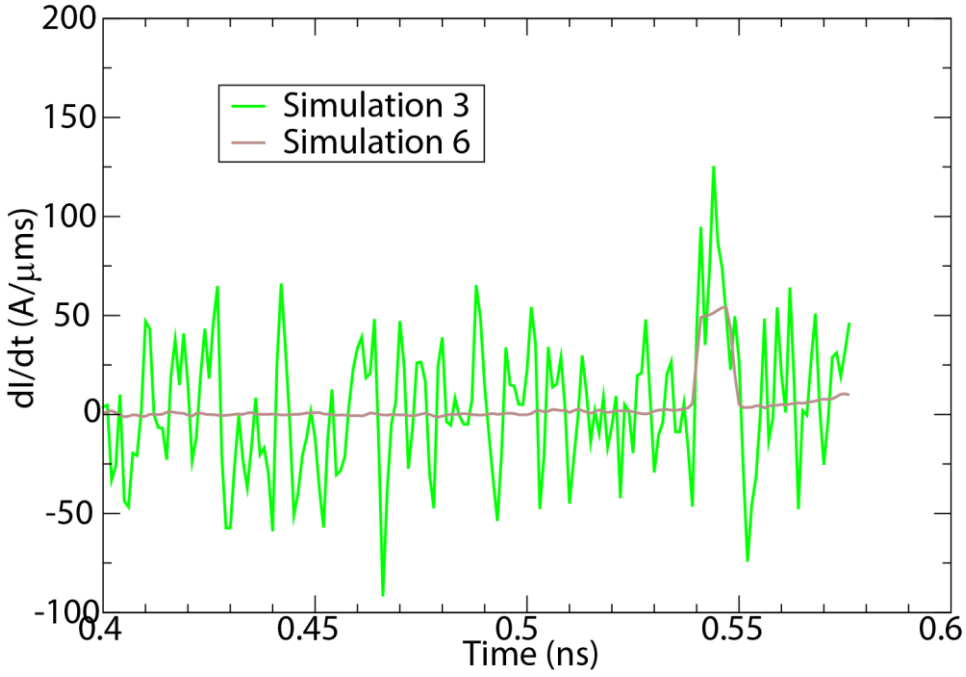

Figure 6.12 – Rate of change of Figure 6.11.

The Debye screening length, given by the expression below, is central to the analysis of charge screening.

$$\lambda_D = \sqrt{\frac{\varepsilon_0 \varepsilon_r k_B T}{2q^2 N_A n}} \tag{6.1}$$

Where N_A is Avogadro's number and n is the molar ion concentration present in the simulation. Using this equation, a Debye length of 0.3 nm for 1 M and 9.74 nm for 1 mM is obtained. This means that the effect of any traversal event 15 nm distance from the FET is strongly screened in the case of a 1 M concentration. Screening is also important in the 1 mM case, but the distance is close enough to the Debye length to ensure that some of the signal remains. According to this analysis, 1mM is approaching the maximum concentration which can be sensed with a 15 nm separation between oxide and pore. A more accurate calculation is further complicated by the presence of the upper bath which has a diminished effect due to the high dielectric constant of the lipid layer.

Figure 6.13 shows the change in the electrostatic potential at the MOSFET surface for 1.05 nm (3 time-steps) changes in ion position, above, below and during traversal of the pore in the lipid membrane. The figure shows the data gathered from a simulation with 1 mM concentration in both the upper and lower baths. These results further illustrate the Coulomb 'defocusing' effect described in section 5.4 now in the presence of potential fluctuations from the rest of the ions in the solution. It is clear that, while, some variation in potential change can be observed in various positions due to local ions, the overall trend is the same with the 'defocusing' of the Coulomb potential is clearly evident as the ion traverses

the pore. On average, the defocussing is not affected by the 1 mM solutions, but the individual changes, especially with higher concentrations, show that the surrounding solution must be taken into consideration.

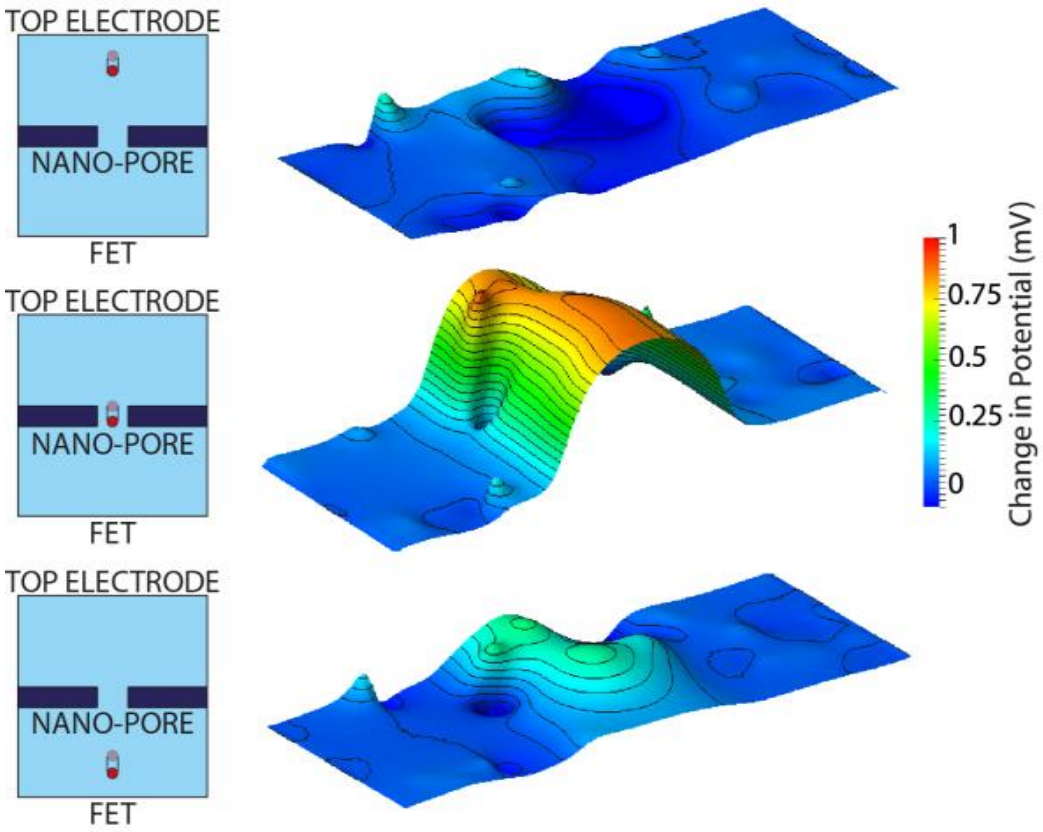

Figure 6.13 – Change in silicon interface potential (mV) as an ion is moved 1.05 nm (three time steps) towards the oxide of the FET. In this case there are 1 mM concentrations of sodium and chloride ions above and below the lipid layer. The planes are in similar positions to Figure 5.15.

6.5 Brownian Traversal Simulations

The final phase of these simulations is to allow the pore traversal to happen 'naturally,' as in the simulations discussed so far, ions have been 'forced' to traverse the pore over a predetermined time period in the order of ps. This is, of course, not what would happen in reality, and it is therefore necessary to create a more realistic simulation within the constraints of computational efficiency. Such simulations, for example, can allow the estimation of the ion traversal time through the pore.

The simulations were carried out using the device structure which is described in section 5.4. As in section 6.4, upper and lower ion baths of 1 mM chloride and sodium were created, recognising that these concentrations will provide a detectable traversal signal, whilst retaining realistic levels of Brownian noise and interaction of the traversing ion with other ions in the baths. The potential gradient between the top electrode and the oxide above the channel was approximately 0.7 V, with 0.5 of this dropping across the lipid layer. This potential gradient makes a traversal event more likely.

As before, in order to avoid unphysical transients caused by the sudden introduction of a particle in the middle of the domain, a single positive ion was initialised at the beginning of the simulation in addition to the background concentrations. This ion was held in position for 500 time-steps, while the background concentration of ions moved towards a realistic distribution. After this period, instead of moving the ion, it was instead 'released' and the simulator treated it in the same way as all of the other ions. To improve the likelihood of a traversal event, the ion was placed 0.25 nm above the entrance to the nano-pore.

For direct comparison with previous results, a full drift diffusion simulation was completed after every time-step.

Multiple simulations were required to observe a single traversal event, since in many cases the Brownian motion of the ion, or local electric fields would move the ion away from the entrance to the ion channel. The success rate was approximately 1 in 10, and was largely dependent on the random distribution of ions prior to the release of the transit ion. This correlates well with a basic analysis of the problem as, neglecting the effect of the electric field, the ion will have approximately a 1 in 7 chance of entering the pore from the starting position. This is based on treating the probability of possible movements of the ion as equal in all directions in the surrounding sphere. The section of the sphere which includes the entrance to the pore is approximately one seventh of that area. The average electric field from the top electrode to the gate dielectric should increase the chance as the particle will be drawn towards the lower potential, but local potential fluctuations due to other individual ions will also have an effect on the direction of movement. A more accurate success rate estimate would require significantly more individual simulations, as each simulation requires in excess of a week to perform. Overall, the ion will only be trapped in the channel when the potential drop in the pore is greater than the local potential fluctuations in the region surrounding the ion.

When the ion did permeate the pore and traverse to the lower bath it exhibited Brownian motion, moving both up and down, in small steps. The mean movement per ps in x while traversing was 3.2×10^{-11} m with a range of 2.5×10^{-13} m to 1.3×10^{-10} m resulting a traversal period in the range of 0.25 ns compared to the forced traversal which took place over 0.01 ns. The scattering from the walls of the pore were also taken into account in the simulation.

Figure 6.14 shows the trace of one successful traversal simulation. The left axis denotes the particle position, where the 77 nm position marks the bottom of the lower bath. The right axis denotes the drain current per micron of the biased FET, showing that there is a clear increase in drain current as the traversal occurs. The dashed lines indicate the position of the nano-pore for reference.

As with previous traversal simulations, it is clear that there is an increase in the drain current. Compared to the equivalent simulation (simulation 5) in section 6.4 the current increase is halved and occurs over 25 times great period. That this

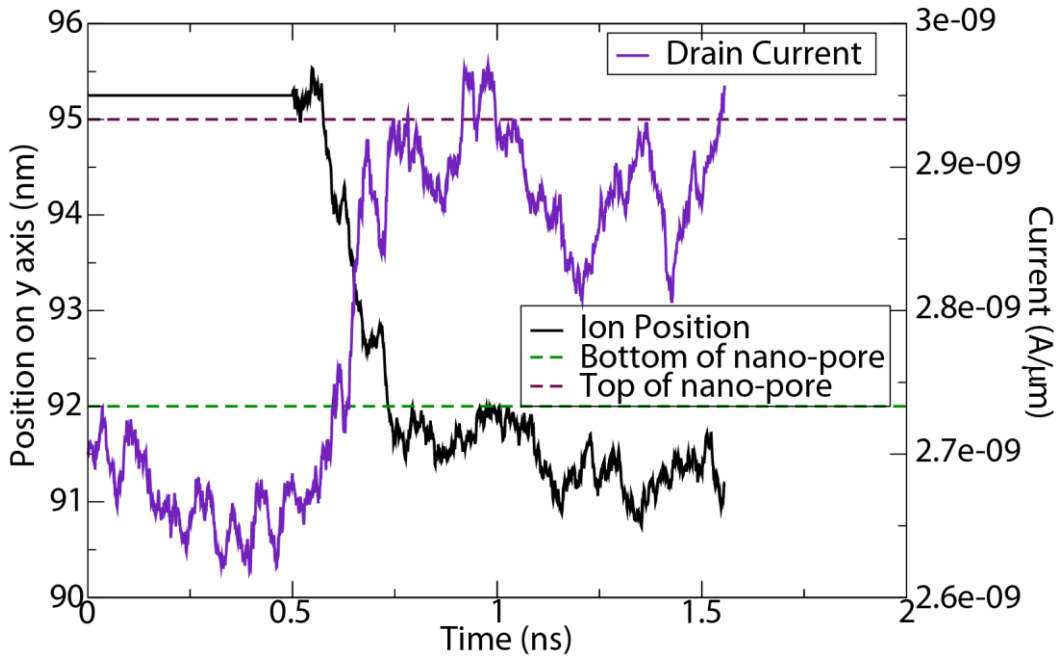

Figure 6.14 – Position of ion plotted alongside the drain current of the FET for an ion of single electron charge traversing a 3 nm long 0.5 nm diameter pore in a lipid membrane placed 15 nm above the oxynitride gate insulator of a 35 nm nominal channel length FET and surround with a 1 mM ionic solution.. The nano-pore is indicated by the dashed lines.

alone is not sufficient to indicate that the channel is occupied. Since the current fluctuations between 1 ns and 1.5 ns move to levels similar to those during the traversal event, Brownian fluctuations can be on the order of 1.5 A/µm which is close to the overall change in the region of 4 A/µm caused by the traversal. As a result it is unsafe to assume that a simple measure of current at any time can confirm that the channel has been traversed, and is even less safe to use the absolute current level to calculate when traversal occurred.

To confirm the traversal event two additional methods of data analysis have been used. The first is the integration of the current, shown in Figure 6.15. The integral of the current clearly changes at the point where the ion is approximately half way through the pore. The change from negative gradient to positive gradient in the

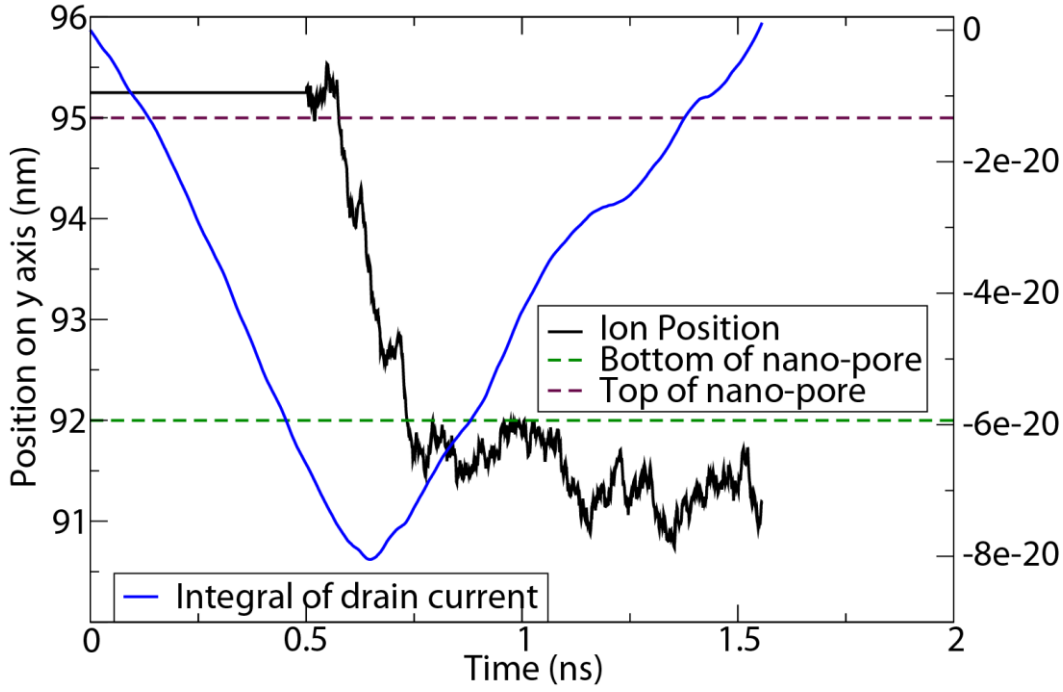

Figure 6.15 – Integral of the drain current plotted alongside ion position for an ion of single electron charge traversing a 3 nm long 0.5 nm diameter pore in a lipid membrane placed 15 nm above the oxynitride gate insulator of a 35 nm nominal channel length FET and surround with a 1 mM ionic solution.

drain current integral is a much clearer indicator of pore ion occupation.

To further analyse the traversal, the rate of change was calculated as in the previous section. This was then averaged over an 0.1 ns window, to reduce the high frequency changes caused by the rapid small movements of the ion which hide the general trend of the movement. The corresponding trace is shown in Figure 6.16, where the rate of change of current is more than double the maximum elsewhere in the trace. The peak value during traversal is 2.23 A/µms whereas in the rest of the trace the maximum is 1.04 A/µms. Removing the signal and the settlement period, the standard deviation of the trace is 0.55 A/µms meaning that the traversal signal is more than 4 σ giving stronger, conclusive, indication of the traversal. There is a problem during traversal, though, where there is a double peak in the trace, this is caused by a stochastic upwards movement of the ion

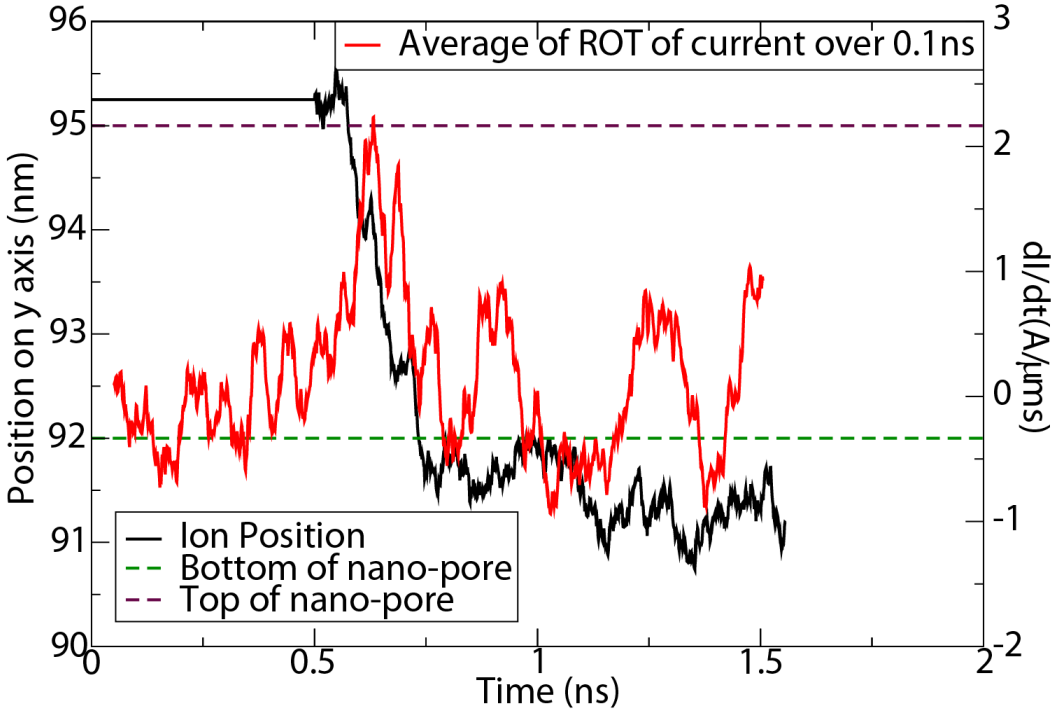

Figure 6.16 – Average (over 0.1 ns) of the drain current for an ion of single electron charge traversing a 3 nm long 0.5 nm diameter pore in a lipid membrane placed 15 nm above the oxynitride gate insulator of a 35 nm nominal channel length FET and surround with a 1 mM ionic solution.. Two peaks are evident as the ion moves through the pore.

during the traversal, which when averaged in this way significantly effects the output.

Figure 6.17 shows a similar trace averaged over 0.09 ns. This shows the effect of changing the smoothing factor. The dip between two peaks has been vastly reduced, and the peak of the signal made stronger in comparison to the rest of the trace, however the automating the process of choosing the smoothing factor, and of traversal detection by this method is still non-trivial.

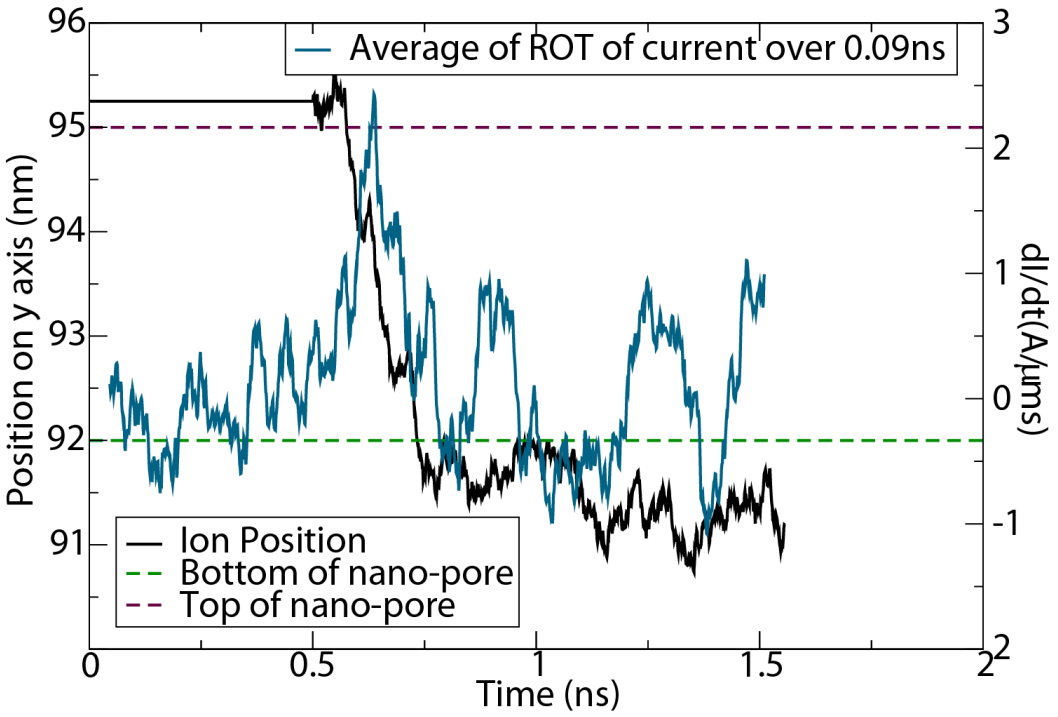

Figure 6.17 – Average (over 0.09 ns) of the rate of change of drain current. There is an identifiable peak during the permeation.

For the above reason a further detection method was developed. The magnitude, as opposed to the value, of the rate of current change was averaged over 0.1 ns, since this should reduce errors due to the smaller movements within the channel, especially those in the direction opposite to the traversal direction. This is because the movement of the ion inside the pore causes a rapid change in current in either direction while it occupies the pore. As shown in Figure 6.18, the average of the magnitude of the rate of change remains much higher than the rest of the trace throughout the traversal, and the effect of the dip described in the previous paragraph is reduced. The trace also remains at a higher level for more of the permeation time, giving a greater indication of the position of the ion.

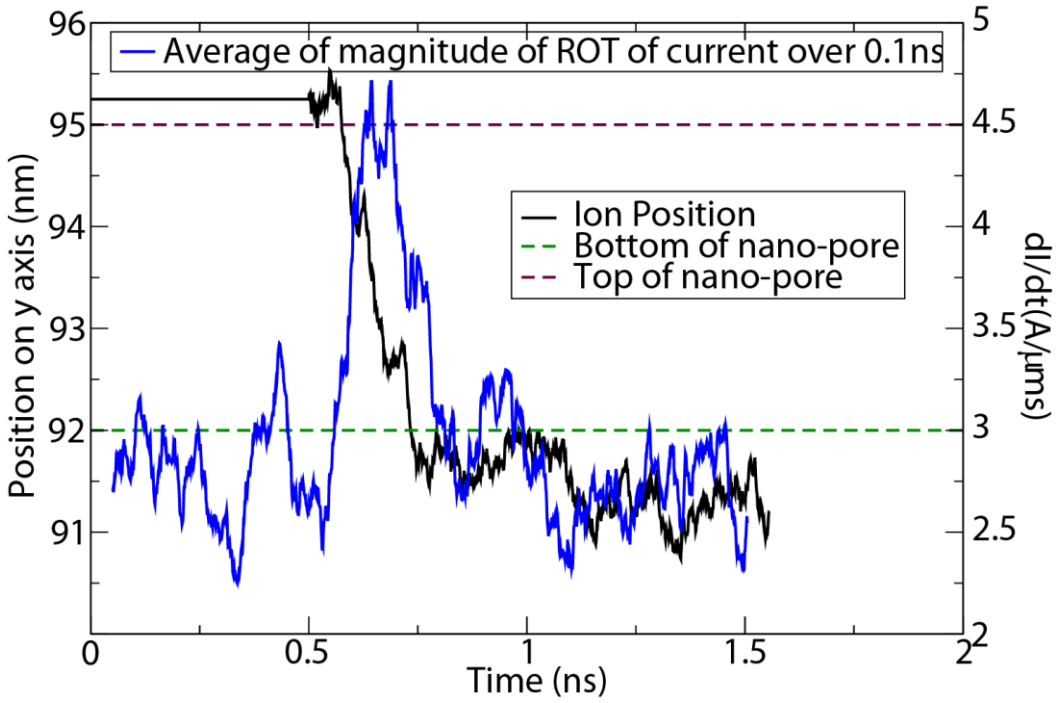

Figure 6.18 – Average of the magnitude of the rate of change.

The clearer indication of pore occupation does, however, come at some cost. Without knowledge of the position of the ion, which is the purpose of the sensor, it is impossible to identify the direction of travel from this trace. The computational part of a sensor using this system would require calculations based on the traces in both *x* and *y* to identify the direction of travel, and the point of traversal. However, such an analysis should not pose any significant computational overheads over those required for this system to be successful.

These final results clearly indicate that the occupation, and direction of travel of an ion through a pore, can be identified from the drain current of a sensing nano scale FET. The rate of change of the current trace is the clearest indicator of the presence of the ion, and gives an automatically identifiable signal, which is not possible from the current trace alone.

6.6 Conclusion

Initial experiments showed that the movement of ions in an aqueous solution above the insulating layer of a modern FET have a direct and measurable impact on the drain current of the FET. It was demonstrated that the fluctuations in ionic movement are at a rate below the maximum response of the FET.

The experiments in this chapter demonstrate that the presence of background concentrations have a significant impact on the viability of using the drain current of a FET as a means of analysing ion traversal through a nano-pore. If the aqueous solution below the lipid membrane has a concentration of 1 M, the traversal of the pore cannot be measured. At lower concentrations, however, the transit of the ion can be directly observed, though there are some inherent difficulties. As the

background concentrations cause noise in the current trace, it is possible that the absolute value of the current will be higher at times other than the transit. Instead, the rate of change of current can be used to demonstrate when the ion is situated in the nano-pore as this is significantly higher (up to double) when an ion occupies the pore than at any other stage. Further investigation would yield optimal time-scales for the averaging system.

The ion transit has been observed monitoring the rate of change of current in situations where the ion is moved artificially through the pore, but more importantly, when allowed to move freely through the pore following Brownian motion. This simulation methodology is a considerable improvement in the state of the art [21] which required the modification of commercial software to analyse a similar system using only drift diffusion simulators. The system in this research is capable of introducing the discrete nature of ions while maintaining the computationally efficient drift diffusion technique in the FET region.

Chapter 7

Conclusions and Further Work

7.1 Conclusions

This thesis details the development and testing of a combined drift diffusion and Brownian dynamics simulator. A simulation framework including drift diffusion and Brownian simulation domains coupled through the solution of Poisson's equation has been developed. This is the first time these techniques have been combined in this way and allows the advantages of two separate simulation methodologies to be combined to create an efficient bio-nano-sensor simulator which is capable of resolving the effect of individual ions. This task was non-trivial and formed a large part of the development of the research presented in this work. The alignment of these two techniques in a single 3D simulation domain is one of the most significant achievements of the research.

A strict testing regime was employed to ensure accuracy throughout the different development stages. Comparisons and validation was carried out using both analytical results and previous simulation standards. This testing included interfacing an analytically doped gateless MOSFET to an aqueous ionic solution

in order to test the functionality of the simulator and showed successful integration of the simulation methodologies.

The developed software was used to investigate the capabilities of the FET as a sensing mechanism using individual ionic charges in a solution suspended above the FET. This is the first time that a simulator has been used to investigate the influence of individual ions on the drain current of a FET. The greatest effect on absolute current occurs when an ion is close to the gate dielectric, closer to the source than the drain. The response of the drain current of a FET to the position of a single ion through a nano-pore has been shown. When a lipid layer with a nano pore is suspended 15 nm above the oxide layer, the position of ions has a detectable effect on the drain current of a FET – from the top of the lipid layer to the bottom of the lipid layer there is a 5 nA/μm increase in drain current. The effect of the position of the lipid layer was also investigated showing that the absolute current is directly affected by the position of the layer, and that the lipid layer is the source of the defocusing effect on the Coulomb potential.

The dual simulator was used to investigate the stochastic movement of ions and its effect on FET drain current. A preliminary analysis of the Brownian noise in the drain current due to the motion of ions was performed to determine whether it is possible to sense single ion transport events in the presence of significant background noise.

The results show, for the first time, that it is possible to detect the permeation of single ion through a pore using a nano-scale transistor, and that the sensing ability remains despite the Brownian noise introduced by other ions in solution. With a lipid layer suspended 15 nm above the oxide layer, it was possible to determine the traversal of an ion through the rate of change of drain current with background

concentrations up to 1 mM. The detection was to 4 σ. The simulations show the high sensitivity of the transistor characteristics to individual ions in the solution. This is due to the low dielectric constant of the membrane 'defocusing' the Coulomb potential of the permeating ion which results in strong proximity impact on the potential and therefore on the current in the sensing transistor. Still, careful choice of the concentrations in the electrolyte solutions above and below the membrane is required in order to avoid the screening of the coulomb potential from the permeating ion by the other mobile charges in the solution and to obtain a strong signal to noise ratio. These results indicate a significant advance on the previous state of the art as, for the first time, a single simulator can be used to investigate the operation of a FET as the surface potential is altered by the stochastic movement of individual ions.

7.2 Further Work

It is important to investigate the possible range of sensitivity of the sensor simulated in this work, and the maximum concentrations with which it will continue to function. Additionally, investigation of impact of the lipid position, substrate, drain and gate electrode biasing, and time step could be performed. This work forms the first steps in the investigation of the direct coupling of nanoscale semiconductor and biological components and opens new possibilities for sensory applications.

While there are many positive results from this work, extensive research can continue on many fronts. Initially, an investigation of the optimum position of the

lipid layer and nano pore may yield further improvements in sensitivity. There is a possibility that such analysis will hone alterations in the sensor design and could allow single ion sensing in the presence of greater background concentrations. Similarly, the biases applied to the transistor could be altered to improve sensitivity.

One important aspect which has not yet been investigated is the effect of movement and placement of the nanopore. Should the pore move or stretch towards the source side of the channel, this would most likely increase the sensitivity of the device, though movement towards the drain would likely cause the inverse. The position of the nanopore in a manufactured device could drift in all dimensions during use since the lipid layer is fluid, and the simulator is well placed to investigate the effects of this movement on sensitivity. The software could be altered to allow movement of the nanopore throughout the duration of the simulation.

The introduction of more complex biological structures could also be simulated. DNA sensing, as mentioned in the second chapter is an ideal application of such a methodology. The inherent charges on a single strand of DNA could be observed as the strand is ‘pulled’ through a nano-pore interfacing with a nano-scale transistor. This could be performed far more efficiently compared to the current optical methods. Success in such simulation could contribute to the development of rapid diagnostic technology with a broad range of applications.

Artificial or biological ion channel structures could replace the current simple nano-pore, with little additional development work. These could be engineered to utilise inherent selectivity, allowing for targeted sensors.

On the software front, the development can continue in two directions. Initially, improvements can be made to the drift diffusion solver to allow the simulation of more realistic device structures. The addition of density gradient or quantum corrections and various sources of statistical variability, all of which have significant effects on such small devices, would allow for better alignment to experimental studies. Finally, the combination of methodologies could be take further to allow greater efficiency for example, only modelling the nano-pore region with Brownian Dynamics while modelling other areas as a continuum.

Simulation of semiconductor devices is a key method in the development stages of device design. The simulation software in this research has been developed to allow its use as a design tool. By simulating novel devices without the great expense of manufacturing, some analysis can be performed.

The prospects for research combining biological and electronic elements are enormous. Simulation combined with experimental work may yield the development of important biomedical and industrial diagnostics based on a significant requirement for portable, inexpensive and most importantly rapid sensing tools.

References

[1] B. Lübbers et al., "A novel GaN-based multiparameter sensor system for biochemical analysis," *Physica Status Solidi (c)*, vol. 5, no. 6, pp. 2361-2363, 2008.

[2] C. Millar, S. Roy, O. Beckstein, M.S.P. Sansom, and A. Asenov, "Continuum vs. particle simulations of model nano-pores," *Journal of Computational Electronics*, vol. 6, no. 1, pp. 367-371, 2007.

[3] Campbell Millar, "3D Simulation Techniques for Biological Ion Channels," PhD Thesis, University of Glasgow, 2003.

[4] G.D. Roy, "Simulation of Intrinsic Paramter Fluctuations in Nano-CMOS Devices," PhD Thesis, University of Glasgow, 2005.

[5] S. Chung, T.. Allen, and S. Kuyucak, "Modeling Diverse Range of Potassium Channels with Brownian Dynamics," *Journal of Biophysics*, vol. 83, no. 1, pp. 263-277, 2002.

[6] G. Roy, A. Brown, F. Adamu-Lema, S. Roy, and A. Asenov, "Simulation study of individual and combined sources of intrinsic parameter fluctuations in conventional nano-MOSFETs," *IEEE Transactions on Electron Devices*,

vol. 53, no. 12, pp. 3063-3069, 2006.

[7] D. Sharma, D. Fine, and A. Dodabalapur, "A new four-terminal hybrid silicon/organic field-effect sensor device," *Device Research Conference Digest, 2005. DRC '05. 63rd* , vol.1, no., pp.109,110, 22-22 June 2005.

[8] D.-S. Kim et al., "An FET-type charge sensor for highly sensitive detection of DNA sequence," *Biosensors and Bioelectronics*, vol. 20, no. 1, pp. 69-74, 2004.

[9] B. Hille, *Ion Channels of Excitable Membranes*, 3rd ed.: Sinauer Associates, 2001.

[10] T.A. Van Der-Straaten, J.M. Tang, U. Ravaioli, R.S. Eisenberg, and N.R. Aluru, "Simulating Ion Permeation Through the ompF Porin Ion Channel Using Three-Dimensional Drift-Diffusion Theory," *Journal of Computational Electronics*, vol. 2, no. 1, pp. 29-47, 2003.

[11] S. Pandey, A. Bortei-Doku, and M.H. White, "Simulation of biological ion channels with technology computer-aided design," *Computer Methods and Programs in Biomedicine*, vol. 85, no. 1, pp. 1-7, 2007.

[12] Z. Sands, A. Grottesi, and M.S.P. Sansom, "Voltage-gated ion channels," *Current Biology*, vol. 15, no. 2, pp. R44-R47, 2005.

[13] S. Aboud, M. Saraniti, and R. Eisenberg, "Computational Issues in Modeling Ion Transport in Biological Channels: Self-Consistent Particle-Based Simulations," *Journal of Computational Electronics*, vol. 2, no. 2, pp. 239-243, 2003.

[14] C. Millar, A. Asenov, S. Roy, and A.R. Brown, "Simulating the bio-nano-CMOS interface," *Nanotechnology, 2005. 5th IEEE Conference on* , vol.,

no., pp.171,174 vol. 1, 11-15 July 2005.

[15] S. Chung and S. Kuyucak, "Recent advances in ion channel research," *Biochimica et Biophysica Acta (BBA) - Biomembranes, Membrane Protein Structure*, vol. 1565, no. 2, pp. 267-286, 2002.

[16] H. Miedema et al., "A Biological Porin Engineered into a Molecular, Nanofluidic Diode," *Nano Letters*, vol. 7, no. 9, pp. 2886-2891, 2007.

[17] B. Eisenberg, "Ion Channels as Devices," *Journal of Computational Electronics*, vol. 2, no. 2, pp. 245-249, 2003.

[18] C. Millar et al., "Brownian Simulation of Charge Transport in Alpha-Haemolysin," *Journal of Computational Electronics*, vol. 7, pp. 28-33, 2008.

[19] L. Wallman et al., "Perforated silicon nerve chips with doped registration electrodes: In vitro performance and in vivo operation," *IEEE Transactions on Biomedical Engineering*, vol. 46, no. 9, pp. 1065-1073, 1999.

[20] ITRS 2005, International Roadmap for semiconductors, 2005.

[21] C. Millar, S. Roy, A.R. Brown, and A. Asenov, "Simulating the Bio-nanoelectronic Interface," *Journal of Physics Condensed Matter*, vol. 19, no. 21, pp. 1-12, 2007.

[22] P. Fromherz, "Semiconductor chips with ion channels, nerve cells and brain," *Physica E: Low-dimensional Systems and Nanostructures, Proceedings of the Twelfth International Winterschool on New Developments in Solids State Physics, @'Low- Dimensional Systems: From 2D to Molecules@4'*, vol. 16, no. 1, pp. 24-34, 2003.

[23] S. Middelhoek, "Celebration of the tenth transducers conference: The past, present and future of transducer research and development," *Sensors and Actuators A: Physical*, vol. 82, no. 1-3, pp. 2-23, 2000.

[24] D.R. Thevenot,. Toth, R.A. Durst, and G.S. Wilson, "Electrochemical biosensors: recommended definitions and classification," *Biosensors and Bioelectronics*, vol. 16, pp. 121-131, 2001.

[25] M.J. Schöning and A. Poghossian, "Recent advances in biologically sensitive field-effect transistors (BioFETs)," *Analyst*, vol. 127, pp. 1137-1151, 2002.

[26] J.J. Gooding, "Nanoscale Biosensors: Significant Advantages over Larger Devices?," *Small*, vol. 2, no. 3, pp. 313-315, 2006.

[27] G. Zheng, F. Patolsky, Y. Cui, W.U. Wang, and C.M. Lieber, "Multiplexed electrical detection of cancer markers with nanowire sensor arrays," *Nature Biotechnology*, vol. 23, pp. 1294-1301, 2005.

[28] D.-S Kim et al., "An FET-type charge sensor for highly sensitive detection of DNA sequence," *Biosensors and Bioelectronics*, vol. 20, no. 1, pp. 69-74, 2004.

[29] J.-K. Shin, D.-S. Kim, H.-J. Park, and G. Lim, "Detection of DNA and Protein Molecules Using an FET-Type Biosensor with Gold as a Gate Metal," *Electroanalysis*, vol. 16, no. 22, pp. 1912-1918, 2004.

[30] Y. Chen, X Wang, S. Erramilli, P. Mohanty, and A. Kalinowski, "Silicon-based nanoelectronic field-effect pH sensor with local gate control," *Applied Physics Letters*, vol. 89, no. 22, p. 223512, 2006.

[31] M. Kamahori, Y. Ishige, and M. Shimoda, "DNA Detection by an Extended-Gate FET Sensor with a High-Frequency Voltage Superimposed onto a Reference Electrode," *Analytical Sciences*, vol. 23, pp. 75-79, 2007.

[32] B.A. Cornell et al., "A biosensor that uses ion-channel switches," *Nature*, vol. 387, pp. 580-583, 1997.

[33] E. Stern et al., "Label-free immunodetection with CMOS-compatible semiconducting nanowires," *Nature*, vol. 445, pp. 519-522, 2007.

[34] M.M.-C. Cheng et al., "Nanotechnologies for biomolecular detection and medical diagnostics," *Current Opinion in Chemical Biology*, vol. 10, pp. 11-19, 2006.

[35] C. Berggren, P. Stålhandske, J. Brundell, and G. Johansson, "A Feasibility Study of a Capacitive Biosensor for Direct Detection of DNA Hybridization," *Electroanalysis*, vol. 11, no. 3, pp. 156-160, 1999.

[36] M. Ferrari, "Cancer nanotechnology: opportunities and challenges," *Nature Reviews Cancer*, vol. 5, pp. 161-171, 2005.

[37] D.V. Lim, J.M. Simpson, E.A. Kearns, and M.F. Kramer, "Current and Developing Technologies for Monitoring Agents of Bioterrorism and Biowarfare," *Clinical Microbiology Reviews*, vol. 18, no. 4, pp. 583-607, 2005.

[38] Y. Cui, Q. Wei, H. Park, and C. M. Lieber, "Nanowire Nanosensors for Highly Sensitive and Selective Detection of Biological and Chemical Species," *Science*, vol. 293, no. 5533, pp. 1289-1292, 2001.

[39] V. Krishnamurthy, S.M. Monfared, and B. Cornell, "Ion-Channel Biosensors—Part I: Construction, Operation, and Clinical Studies," *IEEE Transactions on Nanotechnology*, vol. 9, no. 3, pp. 303-312, 2010.

[40] O.S. Smart, J.M. Goodfellow, and B.A. Wallace, "The pore dimensions of gramicidin A ," *Biophysical Journal* , vol. 65, no. 6, pp. 2455-2460, 1993.

[41] X.T. Vu et al., "Top-down processed silicon nanowire transistor arrays for biosensing," *Physica Status Solidi (a)*, vol. 206, no. 3, pp. 424-434, 2009.

[42] Be. Straub, E. Meyer, and P. Fromherz, "Recombinant maxi-K channels on transistor, a prototype of iono-electronic interfacing," *Nature Biotechnology*, vol. 19, pp. 121-124, 2001.

[43] K. Arshak, E. Moore, G.M. Lyons, J. Harris, and S. Clifford, "A review of gas sensors emplyed in electronic nose applications," *Sensor Review*, vol. 24, no. 2, pp. 181-198, 2004.

[44] K.-Y. Park et al., "Development of FET-type albumin sensor for diagnosing nephritis," *Biosensors and Bioelectronics*, vol. 23, no. 12, pp. 1904-1907, 2008.

[45] T.G. Drummond, M. G. Hill, and J.K. Barton, "Electrochemical DNA Sensors," *Nature Biotechnology*, vol. 21, pp. 1192-1199, 2003.

[46] Y. Han, A. Offenhäusser, and S. Ingebrandt, "Detection of DNA hybridization by a field-effect transistor with covalently attached catcher molecules," *Surface and Interface Analysis*, vol. 38, pp. 176-181, 2006.

[47] A. Star, J.-C.P. Gabriel, K. Bradley, and G. Grüner, "Electronic Detection of Specific Protein Binding Using Nanotube FET Devices," *Nano Letters*, vol.

3, no. 4, pp. 459-463, 2003.

[48] P.M. Levine, P. Gong, R. Levicky, and K. L. Shepard, "Real-time multiplexed electrochemical DNA detection using an active complementary metal-oxide-semiconductor biosensor array with integrated sensor electronics," *Biosensors and Bioelectronics*, vol. 24, no. 7, pp. 1995-2001, 2009.

[49] T. Matsuo and K. D. Wise, "An Integrated Field-Effect Electrode for Biopotential Recording," *IEEE Transactions on Biomedical Engineering*, vol. 6, pp. 485-487, 1974.

[50] I. Lundstrom, S. Shivaraman, C. Svensson, and L. Lundkvist, "A hydrogen-sensitive MOS field-effect transistor," *Applied Physics Letters*, vol. 26, pp. 55-57, 1975.

[51] X.P.A. Gao, G. Zheng, and C.M. Lieber, "Subthreshold Regime has the Optimal Sensitivity for Nanowire FET Biosensors," *Nano Letters*, vol. 10, no. 2, pp. 547-522, 2010.

[52] A. Offenhäusser and W. Knoll, "Cell-transistor hybrid systems and their potential applications," *Trends in Biotechnology*, vol. 19, pp. 62-66, 2001.

[53] H.G. Craighead, "Nanostructure science and technology: Impact and prospects for biology," *Journal of Vacuum Science \& Technology A*, vol. 21, pp. S216-S221, 2003.

[54] A.J. Storm, J.H. Chen, X.S. Ling, H.W. Zandbergen, and C. Dekker, "Fabrication of solid-state nanopores with single-nanometre precision," *Nature Materials*, vol. 2, pp. 537-540, 2003.

[55] M.J. Schöning and H. Lüth, "Novel Concepts for Silicon-Based Biosensors," *Physica Status Solidi (a)*, vol. 185, no. 1, pp. 65-77, 2001.

[56] M. Curreli et al., "Real-Time, Label-Free Detection of Biological Entities Using Nanowire-Based FETs," *IEEE Transactions on Nanotechnology*, vol. 7, no. 6, pp. 651-667, 2008.

[57] J. Bausells, J. Carrabina, A. Errachid, and A. Merlos, "Ion-sensitive field-effect transistors fabricated in a commercial CMOS technology," *Sensors and Actuators B: Chemical*, vol. 57, no. 1-3, pp. 56-62, 1999.

[58] S. Zhaoxia and Z. Dazhong, "Modeling and discussion of threshold voltage for a multi-floating gate FET pH sensor," *Journal of Semiconductors*, vol. 30, no. 11, p. 114011, 2009.

[59] A. Errachid, N. Zine, J. Samitier, and J. Bausells, "FET-Based Chemical Sensor Systems Fabricated with Standard Technologies," *Electroanalysis*, vol. 16, no. 22, pp. 1843-1851, 2004.

[60] M.J. Deen, M.W. Shinwari, J.C. Ranuárez, and D. Landheer, "Noise considerations in field-effect biosensors," *Journal of Applied Physics*, vol. 100, no. 7, p. 074703, 2006.

[61] K.-W. Lee et al., "An underlap field-effect transistor for electrical detection of influenza," *Applied Physics Letters*, vol. 96, p. 033703, 2010.

[62] P.R. Nair and M.A. Alam, "Screening-Limited Response of NanoBiosensors," *Nano Letters*, vol. 8, no. 5, pp. 1281-1285, 2008.

[63] S.N. Kim, J.F. Rusling, and F. Papadimitrakopoulos, "Carbon Nanotubes for Electronic and Electrochemical Detection of Biomolecules," *Advanced*

Materials, vol. 19, pp. 3214-3228, 2007.

[64] P. Bergveld, "Thirty years of ISFETOLOGY: What happened in the past 30 years and what may happen in the next 30 years," *Sensors and Actuators B: Chemical*, vol. 88, no. 1, pp. 1-20, 2003.

[65] A.A. Shul'ga et al., "Operation of an ISFET with non-insulated substrate directly exposed to the solution," *Sensors and Actuators B: Chemical*, vol. 30, no. 2, pp. 101-105, 1996.

[66] P. Bergveld, "Development of an Ion-Sensitive Solid-State Device for Neurophysiological Measurements," *IEEE Transactions on Biomedical Engineering*, vol. 17, no. 1, pp. 70-71, 1970.

[67] P. Bergveld, "Development, Operation, and Application of the Ion-Sensitive Field-Effect Transistor as a Tool for Electrophysiology," *IEEE Transactions on Biomedical Engineering*, vol. 19, no. 5, pp. 342-351, 1972.

[68] H.-J. Park et al., "An ISFET biosensor for the monitoring of maltose-induced conformational changes in MBP," *FEBS Letters*, vol. 583, no. 1, pp. 157-162, 2009.

[69] S. Caras and J. Janata, "Field effect transistor sensitive to penicillin," *Analytical Chemistry*, vol. 52, no. 12, pp. 1935-1937, 1980.

[70] A.B. Kharitonov, M. Zayats, L. Alfonta, E. Katz, and I Willner, "A novel ISFET-based NAD+-dependent enzyme sensor for lactate," *Sensors and Actuators B: Chemical*, vol. 76, no. 1-3, pp. 203-210, 2001.

[71] P. Bergveld, "A critical evaluation of direct electrical protein detection methods," *Biosensors and Bioelectronics*, vol. 6, no. 1, pp. 55-72, 1991.

[72] X.-L. Luo, J.-J. Xu, W.Z., and H.-Y. Chen, "Glucose biosensor based on ENFET doped with SiO2 nanoparticles," *Sensors and Actuators B: Chemical*, vol. 97, no. 2-3, pp. 249-255, 2004.

[73] E. Stern et al., "Importance of the Debye Screening Length on Nanowire Field Effect Transistor Sensors," *Nano Letters*, vol. 7, no. 11, pp. 3405-3409, 2007.

[74] E.I. Rainina, E.N. Efremenco, S.D. Varfolomeyev, A.L. Simonian, and J.R. Wild, "The development of a new biosensor based on recombinant E. coli for the direct detection of organophosphorus neurotoxins," *Biosensors and Bioelectronics*, vol. 11, pp. 991-1000, 1996.

[75] J. Fritz, E.B. Cooper, S. Gaudet, P.K. Sorger, and S.R. Manalis, "Electronic detection of DNA by its intrinsic molecular charge," *Proceedings of the National Academy of Sciences of the United States of America*, vol. 99, no. 22, pp. 14142-14146, 2002.

[76] C. Dekker, "Solid-state nanopores," *Nature Nanotechnology*, vol. 2, pp. 209-215, 2007.

[77] D.W. Deamer and M. Akeson, "Nanopores and nucleic acids: prospects for ultrarapid sequencing," *Trends in Biotechnology*, vol. 18, no. 4, pp. 147-151, 2000.

[78] J.J. Kasianowicz, E. Brandin, D. Branton, and D.W. Deamer, "Characterization of individual polynucleotide molecules using a membrane channel," *Proceedings of the National Academy of Sciences of the United States of America*, vol. 23, no. 24, pp. 13770-13773, 1996.

[79] C. Staii, A.T. Johnson Jr., M. Chen, and A. Gelperin, "DNA-Decorated Carbon Nanotubes for Chemical Sensing," *Nano Letters*, vol. 5, no. 9, pp.

1774-1778, 2005.

[80] Z. Li et al., "Sequence-Specific Label-Free DNA Sensors Based on Silicon Nanowires," *Nano Letters*, vol. 4, no. 2, pp. 245-247, 2004.

[81] J.W. Shim and L. Q. Gu, "Stochastic Sensing on a Modular Chip Containing a Single-Ion Channel," *Analytical Chemistry*, vol. 79, pp. 2207-2213, 2007.

[82] D.-S. Kim et al., "An extended gate FET-based biosensor integrated with a Si microfluidic channel for detection of protein complexes," *Sensors and Actuators B: Chemical*, vol. 117, pp. 488-494, 2006.

[83] B. Roux, "Theoretical and computational models of ion channels," *Current Opinion in Structural Biology*, vol. 12, no. 2, pp. 182-189, 2002.

[84] G.R. Smith and M.S.P. Sansom, "Effective diffusion coefficients of K+ and Cl- ions in ion channel models," *Biophysical Chemistry*, vol. 79, no. 2, pp. 129-151, 1999.

[85] D. Marreiro, M. Saraniti, and S. Aboud, "Brownian dynamics simulation of charge transport in ion channels," *Journal of Physics: Condensed Matter*, vol. 19, no. 21, p. 215203, 2007.

[86] A. Einstein, *Investigations on the Theory of Brownian Movement*.: Dover, 1956.

[87] R. Brown, "A brief account of microscopical observations made in the months of June, July and August 1827 on the particles contained in the pollen of plants; and on the general existence of actrive molecules in organic and inorganic bodies.," *Philosophical Magazine Series 2*, 4, 161-

173, 1828.

[88] Z. Yang, T. A. Van, U. Ravaioli, and Y. Liu, "A Coupled 3-D PNP/ECP Model for Ion Transport in Biological Ion Channels," *Journal of Computational Electronics*, vol. 4, no. 1, pp. 167-170, 2005.

[89] A. Grottesi, C. Domene, S. Haider, and M.S.P Sansom, "Molecular dynamics Simulation approaches to K channels: conformational flexibility and physiological function," *IEEE Transactions on NanoBioscience*, vol. 4, no. 1, pp. 112-120, 2005.

[90] M.S P. Sansom et al., "Potassium channels: structures, models, simulations," *Biochimica et Biophysica Acta (BBA) - Biomembranes*, vol. 1565, no. 2 Membrane Protein Structure, pp. 294-307, 2002.

[91] T. W. Allen and S. H. Chung, "Brownian dynamics study of an open-state KcsA potassium channel," *Biochimica et Biophysica Acta (BBA) - Biomembranes*, vol. 1515, no. 2, pp. 83-91, 2001.

[92] R. Toghraee, R. J. Mashl, K.I. Lee, E. Jakobsson, and U. Ravaioli, "Simulation of charge transport in ion channels and nanopores with anisotropic permittivity," *Journal of Computational Electronics*, vol. 8, no. 2, pp. 98-109, 2009.

[93] A. Burykin, C. N. Schutz, J. Villá, and A. Warshel, "Simulations of ion current in realistic models of ion channels: The KcsA potassium channel," *Proteins: Structure, Function, and Genetics*, vol. 47, no. 3, pp. 265-280, 2002.

[94] C. Millar, A. Asenov, S. Roy, and J.M. Cooper, "Generic Particle-Mesh Framework for the Simulation of Ionic Channels," *Journal of Computational Electronics*, vol. 1, no. 3, pp. 405-409, 2002.

[95] S. Chung, M. Hoyles, T. Allen, and S. Kuyucak, "Study of Ionic Currents across a Model Membrane Channel Using Brownian Dynamics," *Journal of Biophysics*, vol. 75, no. 2, pp. 793-809, 1998.

[96] S. R. Vaccaro, "Position-dependent stochastic diffusion model of ion channel gating," *Phys. Rev. E*, vol. 78, p. 4, 2008.

[97] B.J. Cheng, S. Roy, G. Roy, and A. Asenov, "Integrating 'atomistic', intrinsic parameter fluctuations into compact model circuit analysis," *European Solid-State Device Research, 2003. ESSDERC '03. 33rd Conference on* , vol., no., pp.437,440, 16-18 Sept. 2003.

[98] L. Delle-Site, R.M. Lyndeb-Bell, and A. Alavi, "What can classical simulators learn from ab initio simulations?," *Journal of Molecular Liquids, Molecular Structure and Dynamics in Liquids*, vol. 98-99, pp. 79-86, 2002.

[99] B. Corry, S.Kuyucak, and S. Chung, "Tests of Continuum Theories as Models of Ion Channels. II. Poisson-Nernst-Planck Theory versus Brownian Dynamics," *Journal of Biophysics*, vol. 78, no. 5, pp. 2364-2381, 2000.

[100] P. Graf, M.Kurnikova, R. Coalson, and A. Nitzan, "Comparison of Dynamic Lattice Monte Carlo Simulations and the Dielectric Self-Energy Poisson-Nernst-Planck Continuum Theory for Model Ion Channels," *Journal of Physical Chemistry B*, vol. 108, no. 6, pp. 2006-2015, 2004.

[101] S. Furini, F. Zerbetto, and S. Cavalcanti, "Application of the Poisson-Nernst-Planck Theory with Space-Dependent Diffusion Coefficients to KcsA," *Journal of Biophysics*, vol. 91, no. 9, pp. 3162-3169, 2006.

[102] K. Cooper, E. Jakobsson, and P. Wolynes, "The theory of ion transport through membrane channels," *Progress in Biophysics and Molecular*

Biology, vol. 46, no. 1, pp. 51-96, 1985.

[103] H. Kosina and S. Selberherr, "A Hybrid Device Simulator that Combines Monte Carlo and Drift-Diffusion Analysis," *IEEE Transactions on Computer-Aided Design of Integrated Circuits and Systems*, vol. 13, no. 2, pp. 201-210, 1994.

[104] T. Vora, B. Corry, and S. Chung, "A model of sodium channels," *Biochimica et Biophysica Acta (BBA) - Biomembranes*, vol. 1668, no. 1, pp. 106-116, 2005.

[105] D.Y. Cheng, K. Wu, C.G. Hwang, and R.W. Dutton, "Drain contact boundary specification in windowed Monte-Carlo Device Analysis," *IEEE Electron Device Letters*, vol. 9, no. 10, pp. 503-505, 1988.

[106] C.R. Arokianathan, "Methods for the Atomistic Simluation of Ultrasmall Semiconductor Devices," *PhD Thesis*, University of Glasgow, 1998.

[107] W. H. Press, S. A. Teukolsky, W. T. Vetterling, and B. P. Flannery, *Numerical Recipes: The Art of Scientific Computing*, 3rd ed.: Cambridge University Press, 2007.

[108] G.E.P. Box and M.E. Muller, "A Note on the Generation of Random Normal Deviates," *Annals of Mathematical Statistics*, vol. 29, no. 2, pp. 610-611, 1958.

[109] R. W. Hockney and J. W. Eastwood, *Computer Simulation Using Particles*.: Taylor \& Francis, 1988.

[110] H. K. Gummel, "A Self-Consistent Iterative Scheme for One-Dimensional Steady State Transistor Calculations," *IEEE Transactions on Electron*

Devices, vol. 11, no. 6, pp. 455-465, 1964.

[111] D.L. Scharfetter and H.K. Gummel, "Large-signal analysis of a silicon Read diode oscillator," *Electron Devices, IEEE Transactions on*, vol. 16, no. 1, pp. 64-77, 1969.

[112] A. Brown, Personal Correspondance, 2013.

[113] R. Barrett et al., *Templates for the Solution of Linear Systems: Building Blocks for Iterative Methods, 2nd Edition*.: SIAM, 1994.

[114] H. A. van Der Vorst, "BI-CGSTAB: a fast and smoothly converging variant of BI-CG for the solution of nonsymmetric linear systems," *SIAM J. Sci. Stat. Comput.*, vol. 13, no. 2, pp. 631-644, 1992.

[115] A. Asenov, "Random dopant induced threshold voltage lowering and fluctuations in sub-0.1 μm MOSFET's: A 3-D "atomistic" simulation study," *IEEE Transactions on Electron Devices*, vol. 45, no. 12, pp. 2505-2513, 1998.

[116] Yuan Taur and Tak H. Ning, *Fundamentals of Modern VLSI Devices*.: Cambridge University Press, 1998.

[117] S. Inaba et al., "High performance 35 nm gate length CMOS with NO oxynitride gate dielectric and Ni salicide," *Electron Devices, IEEE Transactions on*, vol. 49, no. 12, pp. 2263-2270, 2002.

[118] A. Asenov, R. Balasubramaniam, A.R. Brown, and J.H. Davies, "RTS amplitudes in decananometer MOSFETs: 3-D simulation study," *Electron Devices, IEEE Transactions on*, vol. 50, no. 3, pp. 839-845, 2003.

[119] I. Moore, C. Millar, S. Roy, and A. Asenov, "Integrating Drift-Diffusion and Brownian Simulations for Sensory Applications," *Ultimate Intigration on Silicon 2010 Proc.*, pp. 85-88, 2010.

[120] W. Im and B. Roux, "Ion Permeation and Selectivity of OmpF Porin: A Theoretical Study Based on Molecular Dynamics, Brownian Dynamics, and Continuum Electrodiffusion Theory," *Journal of Molecular Biology*, vol. 322, no. 4, pp. 851-869, 2002.